The Hong Kong Polytechnic University

Department of Electronic and Information Engineering

The Studies of Improved Quantification Techniques for Positron Emission Tomography

Xiujuan Zheng

A thesis submitted in partial fulfillment of the requirements for the degree of Doctor of Philosophy

September 2010

Certificate of Originality

I hereby declare that this thesis is my own work and that, to the best of my knowledge and belief, it reproduces no material previously published or written, nor material that has been accepted for the award of any other degree or diploma, except where due acknowledgement has been made in the text.

(Signed)

Xiujuan Zheng （鄭秀娟） (Name of Student)

Abstract

Positron emission tomography (PET) technology provides a sensitive, informative and quantitative approach for non-invasively visualization of biological processes with specific molecular probes. Although PET has been widely used in clinical and preclinical studies, there are still some challenges for quantification techniques to provide more reliable information about the underlying biological processes from PET imaging. This thesis is thus devoted to advance appropriate quantification techniques in order to improve the reliability of quantification and to facilitate image analysis, emphasizing on the PET imaging with [^{18}F]Fluoro-2-deoxy-2-D-glucose (FDG-PET) in small-animal studies and dual-time scans for human.

The investigations of this thesis began with the improvements in the reliability of quantification for PET imaging. An automatic image-based method with improved standard uptake values (SUVs) was developed to reduce the influences of the error measurements and the excreted tracer by renal function. The improved SUVs, an image-derived SUV (iSUV) and a modified SUV (mSUV), were proposed and then demonstrated in a set of static mouse FDG-PET studies. For the selected targets, the iSUV and mSUV were compared against their corresponding SUVs. The results indicated that the automatic image-based method could derive the iSUV to replace SUV when the actual measurements were missing or unreliable. Meanwhile, the estimated mSUV can reduce the inter-subject variability and enhance the tumor-to-background separation.

In addition to the improvements in the calculation of SUV, a simulation framework was designed to derive generalized optimal quantitative index (QI) and its associated flexible dual-time imaging protocol for accurately differentiating the malignancy from benign lesions in FDG-PET for lung cancer diagnosis. In computer simulations, the generalized optimal QI can provide the higher accuracy in differentiating malignancy from benign lesions under each noise level than traditional RI for lung cancer diagnosis. The corresponding optimal dual-time imaging protocol was suggested to be flexible, which could be valuable for the high-throughput clinical applications.

Furthermore, the frequent invasive arterial blood sampling to obtain input function poses many challenges and inconvenience for tracer kinetic modeling with dynamic PET imaging. Non-invasive approaches were proposed to address this issue. A simple non-invasive quantification method based on Patlak graphic analysis (PGA) that uses a reference region to obtain the relative influx rate without an input function has recently been proposed. This non-invasive Patlak (nPGA) method was extended to whole-body FDG-PET studies and systematically investigated using a set of mouse studies and computer simulations. In the mouse studies, a high linearity of relative influx rates was observed between the nPGA and PGA for most pairs of reference and target regions, when an appropriate underlying kinetic model was used. The simulation results demonstrated that the accuracy of the nPGA method was similar to that of the PGA method, with a higher reliability for most pairs of reference and target regions. The results proved that the nPGA method could provide a non-invasive and indirect way of quantifying the FDG kinetics in the tissues where the k_4 and vascular effect were negligible.

The automatic non-invasive approach can further facilitate the analysis of dynamic PET imaging. A novel hybrid clustering method (HCM) was proposed to objectively delineate the regions of interest (ROIs) in dynamic PET images for the automatic estimation of image-derived input function (IDIF) and was demonstrated the application to the mouse FDG-PET studies. The results showed that the HCM achieved accurate ROIs delineation in both computer simulations and experimental mouse studies. In the mouse studies the predicted IDIF had a high correlation with the gold standard, the PTAC derived from invasive blood sampling. The results indicate that the proposed HCM has a great potential in ROI delineation for automatic estimation of IDIF in dynamic FDG-PET studies.

In summary, this thesis has significantly contributed to the improvement of several critical quantification approaches for preclinical small-animal studies and clinical patient examinations.

List of Publications

Journal Papers

1. **X. Zheng**, G. Tian, S.-C. Huang, D. Feng, "A Hybrid Clustering Method for ROI Delineation in Small Animal Dynamic PET Images: Application to the Automatic Estimation of FDG Input Function", *IEEE Transactions on Information Technology in Biomedicine* (in press).
2. **X. Zheng**, C.-L. Yu, W. Sha, C. Radu, S.-C. Huang, D. Feng, "Study of an image-derived SUV and a modified SUV in mouse FDG PET", *Nuclear Medicine and Biology* (in press).

Journal Papers (communication papers/abstracts)

1. **X. Zheng**, G. Tian, S.-C. Huang, D. Feng, **"**Semi-automatic Estimation of Image-derived Input Function in Mouse FDG-PET Studies Using One Blood Sample", *The Journal of Nuclear Medicine*, 51(suppl. 2): 514, 2010.
2. G. Tian, **X. Zheng**, S. Song, G. Huang, D. Feng, "Automated Tumor Detection and Treatment Response Assessment with FDG-PET Dynamic Studies", *The Journal of Nuclear Medicine*, 51(suppl. 2): 25, 2010.
3. **X. Zheng**, C.-L. Yu, W. Sha, X. Zhang, A. S. Yu, C. Radu, D. Feng, S.-C. Huang, "Study of a modified SUV to reduce variability and to increase tumor-to-background separation in mouse FDG PET", *The Journal of Nuclear Medicine*, 50 (suppl. 2): 234, 2009.

Conference Papers

1. **X. Zheng**, L. Wen, S.-J. Yu, D. Feng, S.-C. Huang, "A study of non-invasive Patlak quantification for experimental whole-body dynamic FDG-PET studies of mice", *7th IFAC Symposium on Modelling and Control in Biomedical Systems (including Biological Systems)*, 12th-14th August, Aalborg, Denmark.
2. **X. Zheng**, G. Tian, L. Wen, D. D. Feng, "Generalized Optimal Quantitative Index of Dual-Time FDG-PET imaging in Lung Cancer Diagnosis", *2010 IEEE International Symposium on Biomedical Imaging (ISBI)*, 14th-17th April, Rotterdam, Netherlands.

Submitted Papers

1. **X. Zheng**, L. Wen, S.-J. Yu, D. Feng, S.-C. Huang, "A Study of Non-invasive Patlak Quantification for Whole-body FDG-PET Studies in Mouse", 2nd revision resubmitted to *Biomedical Signal Processing and Control*.
2. **X. Zheng**, G. Tian, S. Song, G. Huang, D. Feng, "Automatic Lesion Detection for Measuring Response with Dynamic FDG-PET", submitted to *IFAC world congress 2011 - Special sessions on Image based biomedical system modeling*.

Acknowledgements

I would like to express the deepest gratitude to my chief supervisor, Professor David Dagan Feng, for his excellent guidance and generous support throughout my PhD study. I would also like to thank Professor Henry Sung-Cheng Huang in the Department of Molecular & Medical Pharmacology, David Geffen School of Medicine at UCLA, for his academic guidance and the wisdom imparted to me during the period I studied in his lab as a visiting research student. In addition, I am very grateful to my co-supervisor, Dr. Zheru Chi, for his help and encouragement. Without their supervision, I would not have finished my study smoothly.

I also appreciate the advice, suggestion, support and friendship from my friends and colleagues, in particular, Dr. Lingfeng Wen, Dr. Guangjian Tian, Dr. Koon-pong Wong, Ms. Amy Shu-Jung Yu, Ms. Wei Sha, Dr. James Chin-Lung Yu, and Dr. Hong Fu.

Last but not least, I would like to express my gratitude and love to my family for their continuous support and deep love.

Contents

ABSTRACT I

LIST OF PUBLICATIONS V

ACKNOWLEDGEMENTS VII

CONTENTS IX

LIST OF FIGURES XIII

LIST OF TABLES XIX

ABBREVIATIONS XXI

CHAPTER 1 INTRODUCTION 1

1.1 Overview of Positron Emission Tomography 1

1.2 Motivation 4

1.3 Literature Review 5

1.4 Organization of the Thesis 9

CHAPTER 2 POSITRON EMISSION TOMOGRAPHY AND QUANTIFICATION TECHNIQUES 13

2.1 Principles of PET 13

2.2 Kinetic Modeling 16

2.2.1 Compartmental Model 17

2.2.2 Parameter Estimation 19

2.3 Kinetic Analysis Methods 21

2.3.1 Nonlinear Least Squares Method 21

2.3.2 Linear Least Squares Method 23

2.3.3 Graphic Analysis 24
2.4 Semi-Quantitative Parameters 28
2.5 Noninvasive Methods 30
2.5.1 Image-Derived Input Function 30
2.5.2 Reference Tissue Model 32
2.6 Summary 35

CHAPTER 3 AUTOMATIC IMAGE-BASED METHOD WITH IMPROVED SUVS FOR STATIC SMALL-ANIMAL PET IMAGING 37

3.1 Introduction 37
3.2 Theory of Automatic Image-Based Method with Improved SUVs 38
3.2.1 Automatic Image-Based Method 38
3.2.2 Image-Derived SUV and Modified SUV 42
3.3 Experiments 43
3.3.1 Small-Animal Studies 43
3.3.2 Estimation of iSUV and mSUV 45
3.3.3 Statistical Analysis 45
3.4 Results 47
3.4.1 iSUV vs. SUV 47
3.4.2 mSUV vs. SUV 51
3.5 Discussion 55
3.6 Summary 59

CHAPTER 4 GENERALIZED OPTIMAL QUANTITATIVE INDEX FOR DUAL-TIME PET IMAGING 61

4.1 Introduction 61
4.2 Methods 63
4.2.1 Optimization of Quantitative Index 63

4.2.2 Computer Simulations 65
4.2.3 Performance Evaluation 66
4.3 Results 67
4.3.1 Generalized Optimal Quantitative Index 67
4.3.2 Threshold and Accuracy 68
4.3.3 Effect of Noise 69
4.4 Discussion 70
4.5 Summary 71

CHAPTER 5 NON-INVASIVE PATLAK QUANTIFICATION METHOD FOR DYNAMIC SMALL-ANIMAL PET IMAGING 73

5.1 Introduction 73
5.2 Theory of Non-Invasive Patlak Graphic Analysis 74
5.3 Experiments 76
5.3.1 Small-Animal Studies 76
5.3.2 Computer Simulations 77
5.3.3 Performance Evaluation 78
5.4 Results 81
5.4.1 Estimated Parameters and Simulated TTACs 81
5.4.2 Effect of Relative Influx Rate in Small-Animal Studies 82
5.4.3 Effect of Noise Levels 85
5.4.4 Effect of Kinetic Model in Parameter Estimation 89
5.5 Discussion 90
5.6 Summary 94

CHAPTER 6 AUTOMATIC ESTIMATION OF INPUT FUNCTION FOR DYNAMIC SMALL-ANIMAL PET IMAGING 96

6.1 Introduction 96

6.2 Theory of Hybrid Clustering Method 97
6.2.1 Background Removal 98
6.2.2 Curve Clustering with PRMMs 99
6.2.3 Classes Merging 101
6.2.4 Parameters of the HCM 103
6.3 Estimation of Imaged-Derived Input Function 104
6.4 Computer Simulations 105
6.4.1 Digimouse Phantom Simulations 105
6.4.2 Evaluation of the ROI Delineation 107
6.4.3 Results 109
6.5 Small-Animal Studies 112
6.5.1 Dynamic Mouse FDG-PET Studies 112
6.5.2 Evaluation of the ROI Delineation and IDIF Estimation 114
6.5.3 Results 115
6.6 Discussion 119
6.7 Summary 122
CHAPTER 7 CONCLUSIONS AND FUTURE WORK 124
7.1 Conclusions 124
7.2 Future Work 128
APPENDIX A 132
APPENDIX B 134
APPENDIX C 136
BIBLIOGRAPHY 138

List of Figures

Figure 1-1 Two commercial scanners and their corresponding static images in clinical and preclinical environments. (a) Siemens Biograph™ TruePoint™ PET/CT (reproduced from http://www.medical.siemens.com/); (b) coronal PET/CT fusion image of colon cancer patient acquired using FDG (reproduced from http://www.medical.siemens.com/, data courtesy of cancer imaging and tracer development program, University of Tennessee, Dr. David Townsend); (c) Siemens microPET Focus 220 (reproduced from http://www.medical.siemens.com/); (d) coronal micoPET image of a tumor-planted mouse acquired using FDG in Crump institute for molecular imaging, UCLA. 4

Figure 2-1 Principles of PET: starting with the annihilation process through registering the photons at the scanner ring until the final image reconstruction (reproduced from Dr. Jens Langner's thesis, http://en.wikipedia.org/wiki/File:PET-schema.png). 14

Figure 2-2 Illustration of the four main types of coincidence event. The black dot indicates the source of positron annihilation. (a) a true coincidence; (b) a scattered event where one or both of the photons undergo a Compton interaction (indicated by the open arrow); (c) a random or accidental coincidence arising from two positrons in which one of the photons from each positron annihilation is counted; (d) a multiple coincidence arising from two positron annihilations in which three events are counted. In the case of (b) and (c), the mis-assigned line of response is indicated by the dashed line (reproduced from [68]). 15

Figure 2-3 A tracer time-activity curve obtained from the dynamic PET images..... 16

Figure 2-4 The three-compartment four-parameter FDG model. The first compartment is for the FDG in plasma; the second one is for the FDG in tissue; the third one is for the phosphorylated FDG-6-PO_4 in tissue. 17

Figure 2-5 The data flow to construct the parametric image of *CMRGLc* (reproduced from [26]). 20

Figure 2-6 The iterative process for fitting model outputs to measurements (reproduced from [26]).....21

Figure 2-7 The process of Patlak graphic analysis (from Turku PET Center, http://www.turkupetcentre.net/modelling/guide/patlak_plot.html). In the largest figure, the y-axis contains apparent distribution volumes, i.e. the ratio of tracer concentrations in tissue and in plasma. On x-axis is normalized plasma integral, i.e. the ratio of the integral of plasma concentration and the plasma concentration. 26

Figure 2-8 The three-compartment model for the target tissue and two-compartment model for the reference tissue in neuroreceptor study (reproduced from [26]). .33

Figure 3-1 The flow chart of automatic image-based method for the estimation of iSUV and mSUV. 39

Figure 3-2 Box-and whisker diagrams of estimated error percentage of body weight (BW), injected dose (ID) and 1/iSUVfactor. Box height shows inter-quartile range. The line in the box is for the median. Whiskers indicate the largest observation (minimum to maximum). 48

Figure 3-3 The linear regression performed for all 31 pairs of SUV factor and iSUV factor. The open circle symbols note the scatter plot of the 31 pairs of iSUV factor and SUV factor. The red solid line is the regression line. 48

Figure 3-4 The comparisons between two sets of SUV and iSUV, SUV_{mean} vs. $iSUV_{mean}$ and SUV_{max} vs. $iSUV_{max}$, for (a) brain, (b) heart, (c) lung, (d) liver, (e) kidney, (f) muscle, and (g) tumor shown by box-and-whisker diagram. In each sub-figure, box height shows inter-quartile range. The line in the box is for the median. Whiskers indicate the largest observation (minimum to maximum). ...50

Figure 3-5 The linear regression plots between SUV and iSUV. (a) Linear regression is performed for 217 (7×31, 7 major organs for 31 mice studies) pairs of $iSUV_{mean}$ and SUV_{mean}. (b) Linear regression is performed for 217 (7×31, 7 major organs for 31 mice studies) pairs of $iSUV_{max}$ and SUV_{max}. The black dot symbols note the scatter plot of pairs of iSUV and SUV. The red solid line is the regression line. 51

Figure 3-6 The validation of bladder volume. The estimated bladder volume obtained by the automatic image-based method is compared to the value obtained by manual method with visual support from microCT image. The open circle symbols denote the scatter plot of the pairs of automatic and manual results. The red solid line denotes the linear regression line. 52

Figure 3-7 Plot of tumor and background (lung, liver and muscle) SUVs, iSUVs and mSUVs. The values for tumor (square), lung (circle), liver (triangle) and muscle (cross) are grouped for SUV, iSUV and mSUV to compare the tumor-to-background separations (quantitative measurements of the separation are listed in Table 3-3). (a) This figure shows that the tumor-to-background separation is increased using $mSUV_{mean}$ compared with using SUV_{mean} and $iSUV_{mean}$. A threshold of 1 (gray dash line) is given as an example to separate tumor from background in this figure. (b) This figure shows that the tumor-to-background separation is increased using $mSUV_{max}$ compared with using SUV_{max} and $iSUV_{max}$. A threshold of 1 (gray dash line) is given as an example to separate tumor from background in this figure. 54

Figure 3-8 The microCT and microPET images and the missing body parts in the images. (a) the microCT image has a field of view of 51.2mm×51.2mm×99.2mm. The microCT image voxel size is 0.2mm×0.2mm×0.2mm in a 256×256×496 matrix. (b) The microPET image has a field of view of 51.2mm×51.2mm×75.6mm. The microPET image voxel size is 0.4mm×0.4mm×0.796mm in a 128×128×95 matrix. (c) The fused mircoPET/CT image. In this figure, the contour of the whole body, included the missing parts of the mouse body, is sketched out by red solid line. 56

Figure 4-1 (a) the obtained cost map and (b) the optimal n map.....67

Figure 4-2 The distributions of quantitative measures of three different approaches: (a) RI_flexible, (b) RI_fixed, and (c) QI_flexible. In each subfigure, the red circle denotes the malignant class and blue star denotes the benign class.....68

Figure 4-3 Plots of classification accuracies for three approaches. (a) RI_flexible; (b) RI_fixed; (c) QI_flexible. The best threshold with greatest accuracy for each

approach is illuminated by red circle. The values of the optimum thresholds and greatest accuracies are given in the legends.....69

Figure 5-1 Measured and simulated PTAC and TTACs. (a) Measured PTAC of one sample mouse study; (b) Measured TTACs of one sample mouse study; (c) Simulated noise-free PTAC obtained using (5-6) ; (d) Simulated noise-free TTACs using the rates constants in Table 5-1. 82

Figure 5-2 Plot of percentage bias of relative influx rates estimated by PGA and nPGA methods at different noise levels. In all the sub-figures, the vertical axis denotes the bias in percentage, and the horizontal axis notes the noise level c, which could be set to 0, 0.1, 0.5, 1, 2 and 4. The blue open circle markers indicate the bias values of $K_{\mathrm{tr,PGA}}$ under different noise levels, while the magenta open triangle markers are for those of $K_{\mathrm{tr,nPGA}}$. The solid lines reflect the change tendencies of bias with the rise of noise level. 87

Figure 5-3 Plot of CVs of relative influx rate estimated by PGA and nPGA methods at different noise levels. In all the sub-figures, the vertical axis denotes the CV in percentage, and the horizontal axis denotes the noise level c, which could be set to 0, 0.1, 0.5, 1, 2 and 4. The blue open circle markers indicate the CV values of $K_{\mathrm{tr,PGA}}$ under different noise levels, while the magenta open triangle markers are for those of $K_{\mathrm{tr,nPGA}}$. The solid lines reflect the change tendencies of CVs with the increase of the noise level. 88

Figure 6-1 Flowchart of the proposed HCM for ROI delineation 98

Figure 6-2 The typical FDG TACs for the major thoracic tissues (myocardium, blood cavity, lungs and surrounding muscles) and blood TAC in 60 min.....106

Figure 6-3 A transverse slice of the Digimouse phantom. An extra blood cavity was added inside the heart position, while the rest part of the heart was considered to be the myocardium. 106

Figure 6-4 Five frames of the simulated dynamic FDG-PET image under noise level of 1. (a) 3s post tracer injection. (b) 6s post tracer injection. (c) 36s post tracer injection. (d) 561s post tracer injection. (e) 3306s post tracer injection. 109

Figure 6-5 The delineations of the automatic ROI_{myo} and ROI_{blc} obtained by (a) HCM_1, (b) HCM_60, and (c) KCM. The contours of the automatic ROI_{myo} and ROI_{blc} are sketched by red and blue solid line, while the ground truths are respectively highlighted by green and magenta on the Digimouse phantom. ..111

Figure 6-6 Illustrations of the best and worst cased of ROI delineation among the 12 mice studies. The top row shows the best case (m17332) of ROI delineation using HCM_1 and the results from KCM for comparison. The bottom row depicts the worst case (m19019) using HCM_1 and the results from KCM for comparison. (a) and (d) show the original PET image frames at about 6s, 60s and ~3600s post injection. (b) and (e) exhibit the ROIs derived automatically from HCM_1 compared with the manual ROIs. (c) and (f) display the results from KCM. In (f), KCM failed to get ROImyo. In (b), (c), (e) and (f), the left sub-figure shows the results of automatic ROI delineation compared with the ground truth for myocardium, while the right sub-figure shows the same for the blood cavity. The contours of the automatically derived ROIs are sketched using a red solid line, while the manually defined ROIs are colored in green. 117

Figure 6-7 The plot of the predicted IDIF for one mouse (m17332) comparing with gold standard obtained from invasive blood sampling. 117

Figure 6-8 Comparison of (a) the AUC of the predicted IDIF and the gold standard (GS), (b) the Patlak K_i of the brain, (c) the Patlak K_i of the myocardium, and (d) the Patlak K_i of the muscles.The results of linear regression are shown in the legends. 119

List of Tables

Table 1-1 Characteristics of some molecular image techniques 3

Table 3-1 The comparison of SUV_{mean}, $iSUV_{mean}$ and $mSUV_{mean}$ by average, standard deviation and coefficient of variance. 49

Table 3-2 The comparison of SUV_{max}, $iSUV_{max}$ and $mSUV_{max}$ by average, standard deviation and coefficient of variance. 49

Table 3-3 Comparison of Mahalanobis distance to evaluate SUV, iSUV and mSUV for tumor-to-background separation. 53

Table 4-1 Rate constants of malignant and benign lesions in lung 65

Table 4-2 Accuracy of classification at different noise levels.....70

Table 5-1 The rate constants derived by WNLS in mouse FDG-PET studies 81

Table 5-2 Relative influx rates for the studied pair of target and reference 83

Table 5-3 A summary of linear regression for the same reference groups.....84

Table 5-4 A summary of linear regression for the same target groups. 84

Table 5-5 Estimates of the relative influx rates (K_{tr}) under different noise levels. ..86

Table 5-6 Percent bias of K_{12} and K_{52} of PGA and nPGA compared with true values for different model at noise level c=0. 89

Table 6-1 The Mean Values of The Evaluation Metrics* 110

Table 6-2 The Mean and Standard Deviance (SD) of The Evaluation Metrics For The ROIs Derived By HCM_1 and KCM* 116

Abbreviations

Abbreviation	Expanded Term
CT	Computed Tomography
%ID/g	Percent Injected-Dose per Gram of Tissue
CAD	Computer Aided Detection/Diagnosis
CMRGlc	Cerebral Metabolic Rate of Glucose
CV	Coefficient of Variation
DSC	Dice Similarity Coefficient
EM	Expectation-Maximization
FDG	[^{18}F]Fluoro-2-deoxy-2-D-glucose
FOV	Field of View
FUR	Fraction Uptake Rate
GLLS	Generalized Linear Least Squares
HCM	Hybrid Clustering Method
IDIF	Image-Derived Input Function
iSUV	Image-derived SUV
KCM	K-means Clustering Method
KIS	Kinetic Imaging System
LGA	Logan Graphic Analysis
LLS	Linear Least Squares
LMA	Local Means Analysis
MRGlc	Metabolic Rate of Glucose
MRI	Magnetic Resonance Imaging
mSUV	Modified SUV

Abbreviation	Expanded Term
NLS	Nonlinear Least Squares
nPGA	Non-invasive Patlak Graphic Anaylsis
PCA	Principle Component Analysis
PDF	Probability Density Function
PET	Positron Emission Tomography
PGA	Patlak Graphic Analysis
PRMMs	Polynomial Regression Mixture Models
PTAC	Plasma Time-Activity Curve
QI	Quantitative Index
RI	Retention Index
RMS	Root Mean Square
ROI	Region of Interest
SD	Standard Deviation
SIMO	Single-Input-Multi-Output
SNR	Signal to Noise Ratio
SPECT	Single Photon Emission Computed Tomography
SUV	Standard Uptake Value
TAC	Time-Activity Curve
TBR	Tumor-to-Background Ratio
TTAC	Tissue Time-Activity Curve
WNLS	Weighted Nonlinear Least Squares

Chapter 1

Introduction

1.1 Overview of Positron Emission Tomography

The past few decades have witnessed rapid developments of molecular imaging to non-invasively visualize, characterize and measure the biological processes within living systems by the molecular probes or interactions with molecules [1, 2]. Molecular imaging techniques, such as magnetic resonance imaging (MRI) and functional nuclear medicine imaging, have not only improved the diagnosis and treatment of diseases at a molecular level, but also provided a unique way to understand the fundamental biological and pathological processes inside organisms [2-5]. Table 1-1 lists the abstracted general characteristics of some currently available molecular imaging techniques in [6]. The original table in [6] with more details are also given in Appendix A.

In the field of molecular imaging, PET is a nuclear imaging technique which use radioisotope labeled compounds as molecular probes to image and measure biochemical processes of mammalian biology *in vivo* [1]. The molecular probes are usually called tracer in the field of nuclear medicine, which can be administered to a

subject and ‘trace’ specific biological process. The temporal and spatial information of tracer is detected and stored then as functional images by the PET system. The radioisotope of fluorine (^{18}F) is frequently used in labeling tracers, while there are others radioisotopes used in tracer developments such as oxygen (^{15}O), nitrogen (^{13}N), and carbon (^{11}C). The most attractive advantage of PET is the availability of a large number of tracers specific for different biological processes. Up to now, “Over 500 molecular imaging probes have been developed and consist of various labeled enzyme and transporter substrates, ligands for receptor systems, hormones, antibodies, peptides, drugs (medical and illicit), and oligonucleotides” [1]. The limitations of PET imaging are relatively low spatial resolution and low signal-to-noise ratio (SNR) due to imaging nature of nuclear medicine. To address the issues of lacking accurate anatomical information and prolonged transmission-based attenuation correction in traditional PET imaging, multimodality hybrid imaging systems have been developed such as the integrated scanner of PET/CT [7] or PET/MRI [8, 9]. Several commercial healthcare manufactories have provided the dedicated PET systems with optimal strategies, such as Siemens Biograph^{TM} TruePoint^{TM} PET/CT used in clinical routines and Siemens microPET Focus 220 for preclinical studies. Figure 1-1 shows these two commercial PET scanners and their corresponding static images.

With the dedicated high-performance system and the multi-disciplinary cooperation, PET imaging has been applied in amount of areas because of its high sensitivity to the biological processes. It is reported that PET imaging can provide the early diagnosis of neurological disorders and evaluate the treatment effects [10]. One example is that early Alzheimer’s detections and relevant cause classifications could benefit from the new methods adopted PET imaging [11-13]. Furthermore,

PET imaging can serve the purpose for measuring metabolic viability of cardiac tissue. As a result, PET imaging has been used to detect the coronary artery disease and guide the cardiovascular therapy [14, 15]. Metabolic information from PET images also shows the advantages in cancer studies even in cancer drug developments [5, 16, 17]. The most frequently used PET tracer especially for oncologic imaging (>90% of all cancer-related scans) is [^{18}F]Fluoro-2-deoxy-2-D-glucose (FDG). PET with FDG (FDG-PET) has been widely used for detecting and staging of colorectal cancer, esophageal cancer, head and neck cancer, non-small cell lung cancers, melanoma, and lymphoma [16, 18-20]. With the other more tracers, the versatility of PET in oncologic imaging can help the cancer biologists to measure and understand cancer [21]. PET imaging is also valuable for predicting the tumor response to the therapy and patient survival [22, 23]. In addition, PET can visualize gene expressions *in vivo* [24, 25]. In a word, both in clinical and preclinical environments, PET imaging is a powerful molecular imaging technique in neurology, cardiology, oncology, and genetics *etc*.

Table 1-1 Characteristics of some molecular image techniques

Imaging Technique	Role	Spatial Resolution	Sensitivity	Quantitative degree
MRI	anatomy, function	25 - 100 um	low/medium	++
CT	anatomy	50 - 200 um	not well characterized	not applicable
PET	function, biology	1 - 2 mm	very high	+++
SPECT	function, biology	1 - 2 mm	high	++
Optical	function, biology	2 - 5mm	very high	+ to ++
Ultrasound	anatomy	50-500 um	not well characterized	+

MRI: magnetic resonance imaging; CT: computed tomography; PET: positron emission tomography; SPECT: single photon emission computed tomography.

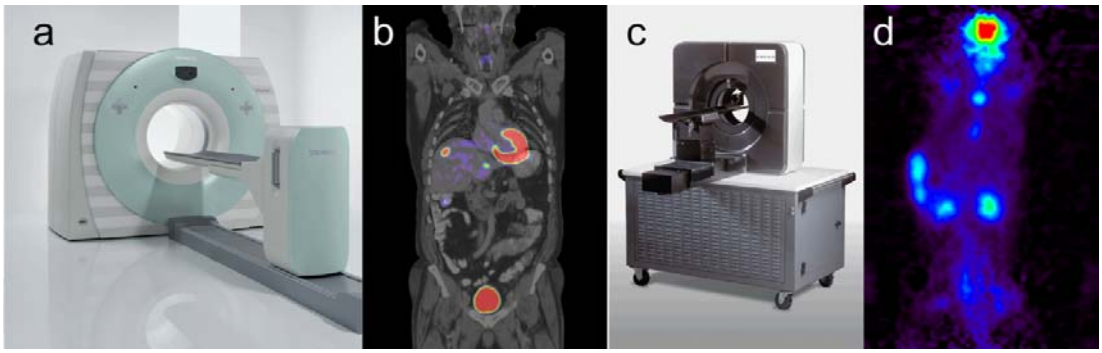

Figure 1-1 Two commercial scanners and their corresponding static images in clinical and preclinical environments. (a) Siemens Biograph^{TM} TruePoint^{TM} PET/CT (reproduced from http://www.medical.siemens.com/); (b) coronal PET/CT fusion image of colon cancer patient acquired using FDG (reproduced from http://www.medical.siemens.com/, data courtesy of cancer imaging and tracer development program, University of Tennessee, Dr. David Townsend); (c) Siemens microPET Focus 220 (reproduced from http://www.medical.siemens.com/); (d) coronal micoPET image of a tumor-planted mouse acquired using FDG in Crump institute for molecular imaging, UCLA.

1.2 Motivation

Facing with these diverse applications with PET, how to efficiently and objectively derive the biological information from PET images becomes a significant issue for designing an appropriate PET assay. Many quantification techniques have been developed to serve this purpose of estimating the biological parameters [26], including the semi-quantitative approaches and tracer kinetic modeling methods. The semi-quantitative approaches are usually simple by neglecting many factors and avoiding prolonged dynamic scans. Invasive blood sampling which is frequently required by the approaches based on tracer kinetic modeling is inconvenient and can induce the harmful effects to subjects and operators. Moreover, the invasive approach is often considered as a challenge in

preclinical studies. On the other hand, the quantification techniques are often conducted based on the operators' experience. These subjective, labor-intensive and time-consuming processes cannot meet the demands of high-throughput PET centers and inter-institute investigations.

In recent years, the development of information technology has inspired more innovative strategies to address the issues in quantitative PET imaging. For example, some approaches based on theory of signal processing have been proposed to explore non-invasive methods and automate the analysis processes based on objective criteria. Nevertheless, more and more preclinical studies related with PET imaging are innovated and applied to explore diverse disorders with new tracers. The utility of the small-animal models enable the preclinical studies to perform *in vivo* testing and revealing the biological processes. The small-animal PET imaging is thriving with the booming developments of biological technologies. The requirements of methodologies to address the specific issues then are increasing along with such the new trend. This motivates my research interest in advancing quantification techniques for achieving better performance of PET imaging especially for small-animal studies, which includes two aims: to improve the reliability of quantification and to facilitate image analysis. Investigations in this topic will enhance the PET image analysis and deliver more benefits to preclinical and clinical studies by using FDG-PET.

1.3 Literature Review

The semi-quantitative approach is applied to quantify the biological processes in a simple way. Standard uptake value (SUV), as the most frequently used semi-

quantitative parameter, is widely applied to measure the tracer uptake in static PET images [27]. It is simple in calculation without the requirement of the invasive blood sampling and suitable for high-throughput imaging centers. However, its variability can be influenced by many factors including the length of uptake period, plasma glucose level, recovery coefficient, partial volume effects [28, 29] and the subject's preparations [30]. In addition, considering the lower concentration in body fat for some tracers, the body weight may not be the best normalization factor in SUV calculation, and the lean body weight or surface area has been proposed as a substitute [31, 32]. SUV can be calculated with the correction of partial volume effects by using the recovery coefficients of the system [33] or a model-based method [34]. In addition to these modifications in SUV calculation, the changes of SUV with imaging time are also studied for improving the quality of quantification in PET studies [35-37]. For applications in the cancer diagnosis, the sole measurement of SUV may not allow optimal differentiation of malignancy from benign lesions [38]. To reduce false positive of benign lesions, dual-time imaging protocol with one early and one delayed static scan has been proposed to classify malignancy from benign lesions using the change of SUVs as the criterion [39]. The dual-time imaging protocol can provide more information than static protocol and higher subject throughput than dynamic protocol. It has already been adopted in clinical cancer diagnosis [40-43]. The optimizations of the imaging protocol and diagnosis criterion are also coming into the focus of researches to improve the diagnostic performance of dual-time PET imaging [44, 45].

Being different from static approaches, tracer kinetic modeling is proposed to analyze the dynamic PET images which visualize spatial and temporal information of the tracer distribution inside the living systems. By assuming an underlying

kinetic model for the tracer, this method uses a tracer plasma time-activity curve (PTAC) as a input function to fit the output function, the target tissue time-activity curve (TTAC), through adjusting kinetic parameters which may be related to physiological/biochemical processes [26]. Although frequent invasive arterial blood sampling is the gold standard for obtaining PTACs in the kinetic quantification, it is harmful to subjects and may expose operators to extra radiation. The invasive blood sampling is also a challenge in preclinical studies with small-animal because of the subject's small size of blood vessels and limited volume of blood. A non-invasive method that eliminates blood sampling has been proposed for simultaneously estimating the input function and physiological parameters from multiple ROIs with distinct TTACs [46, 47]. Without using ROIs, the method based on factor analysis has been developed to extract the input function from the dynamic PET studies for several different tracers [48, 49]. Population-based method [50, 51] and image-derived input function (IDIF) [52, 53] have also been introduced to avoid the invasive approach in clinical environments. The IDIF methods, which rely on a sufficiently large vascular structure in the imaging field of view (FOV), are more direct and convenient to be applied than population-based methods without extra information. Moreover, the reference tissue model has also provided a non-invasive approach to address the problem of invasive blood sampling in neuroreceptor study for the graphical analysis methods [54, 55].

In most quantitative analysis, the tracer time-activity of static images and the time-activity curve (TAC) of dynamic images are usually derived from a predefined ROI placed in the target organ/tissue/lesion. The quality of the ROI delineation depends upon the experience of the operator. The manual approach is subjective, labor-intensive, and time-consuming, and as such semi- or fully-automatic ROI

delineation methods that utilize some objective criterion are necessary in order to overcome these disadvantages and to benefit the development of automatic high-throughput analysis. One approach is to register PET image with the high spatial resolution anatomical image, such as CT or MRI, then to delineate the ROI or segment PET images based on the spatial information from the aligned images [56]. Furthermore, a template-based method has been developed to automatically delineate the ROIs in PET images using the anatomical image and supplementary predefined template [57]. Because these methods are relying on image registration algorithms, they usually perform well in rigid structures that have the stable and similar shape among subjects, such as the brain. Another approach is to directly delineate ROIs in PET images using the techniques of image segmentation. In dynamic PET images, every pixel has a corresponding TAC which reflects the temporal information of tracer distribution. Many pixel-clustering methods have successfully used the temporal information for image segmentation by assuming that the TACs of pixels in the same tissue or organ have similar shapes and magnitudes. By assuming the TACs as the feature vectors of pixels, the K-means clustering method has been proposed in the segmentation of major organs from dynamic PET images [58]. This method was later extended to 3D segmentation of white and gray matters in the brain by integrating the kinetic features [59]. K-means clustering has also been used to segment PET images of the brain with principle component analysis (PCA) [60]. An unsupervised method, called local means analysis (LMA), has been introduced for tissue segmentation in dynamic rodent whole-body PET images, without guidance from anatomical image [61]. Clustering methods have also been used to obtain non-invasive arterial input functions from human brain studies [62, 63] and small-animal cardiac images [64]. In addition to these clustering

methods for the segmentations of reconstructed images, a clustering method with iterative coordinate descent has been adopted to directly segment dynamic PET images in the projection domain [65, 66].

Despite the significant efforts that have gone into attempting to develop and improve quantification techniques, there are still many issues that need to be addressed in order to achieve better performance of PET imaging with the high quantification quality and convenient processes.

1.4 Organization of the Thesis

This thesis is composed of seven chapters, which are organized as follows.

Chapter 1 introduces the role of PET in molecular imaging, especially for its versatility in quantitative analysis. A comprehensive literature review of quantification techniques in PET is then provided to emphasize the motivation of this thesis. This thesis focuses on the studies of improved quantification techniques for achieving better performance of PET imaging. Finally, the organization of this thesis is represented.

After reviewing the principles of PET imaging, Chapter 2 introduces the basics of quantification techniques for analysis PET images, including the tracer kinetic modeling for dynamic imaging, the semi-quantitative parameters for static imaging as well as the non-invasive methods. These fundamental methods are going to be used and discussed in the further investigations of this thesis.

Chapter 3 explores an automatic image-based method to derive SUV and a modified SUV for oncologic FDG-PET studies with small-animal. The image-

derived SUV can replace SUV when actual measurements are missing or unreliable. This is valuable for multidisciplinary and inter-institution large-scale database in education and scientific research. The modified SUV can reduce the inter-subject variability and enhance the tumor-to-background separation, which has the potential to increase the accuracy of cancer detection.

Chapter 4 explores a framework for simultaneously optimizing quantitative indexes and dual-time imaging protocol for FDG-PET imaging and demonstrates its potential in clinical lung cancer diagnosis. A generalized optimal quantitative index with its corresponding dual-time imaging protocol is derived by computer simulations and achieves the highest accuracy of the differentiation of malignancy and benign lesions.

Chapter 5 introduces a non-invasive Patlak graphic analysis method to measure the glucose metabolism using relative influx rates and then extends this method to whole-body small-animal studies. The systematic investigations using computer simulations and experimental FDG-PET studies both demonstrate that high linearity of relative influx rates are achieved between non-invasive Patlak graphic analysis method and common Patlak graphic analysis method for most target and reference regions when using the appropriate kinetic model.

Chapter 6 proposes a novel hybrid clustering method that objectively delineates ROIs in dynamic PET images for the automatic estimation of image-derived input functions for small-animal studies. This method can achieve accurate ROI delineations in both computer simulations and experimental mouse FDG-PET studies. In the mouse studies, the predicted image-derived input function has a high correlation with the referenced method. The results indicate that this proposed

method has a great potential in ROI delineation for automatic estimation of image-derived input functions for dynamic PET studies.

Chapter 7 concludes the investigations described in the previous chapters. After summarizing the major work and contributions of this thesis, some suggestions of the future work are given out.

Chapter 2

Positron Emission Tomography and Quantification Techniques

2.1 Principles of PET

PET imaging relies on detecting photons originated from injected tracer to visualize biochemical processes in living systems. A radioisotope (such as ^{18}F) labeled tracer is injected into the subject (usually into the blood circulation). The instable radioisotope in the injected tracer undergoes radioactive decay by transforming atom to more stable state with positron emitted. The positron travels a very short distance and then collides with an electron in surrounding tissues, which leads to an annihilation with two 511-keV photons travelling 180º apart. These two photons are detected as a coincident event when they simultaneously strike two small detectors in opposite directions. The source of these photons (the location of annihilation) can be localized along the line connecting these two detectors, which is called the line of response (LOR). In general, there are about 6-70 million detector pair combinations for recording coincident events from many different angles around the subject. All the recorded coincident events are transformed into sinogram

or listmode data and then reconstructed to tomographic images. Figure 2-1 shows the principles of PET. Under ideal circumstances, only true coincident events, where two detected annihilation photons originate from the same radioactive decay and have not changed direction or lost any energy before detecting, are recorded in PET system. However, due to the limitations of the detectors, a number of undesirable events are "accidentally" recorded in actual condition. The measurements of coincident evens are contaminated with these undesirable events, which includes random, scattered and multiple coincidences [67, 68]. Figure 2-2 shows the four main coincident event types for a full-ring PET system diagrammatically.

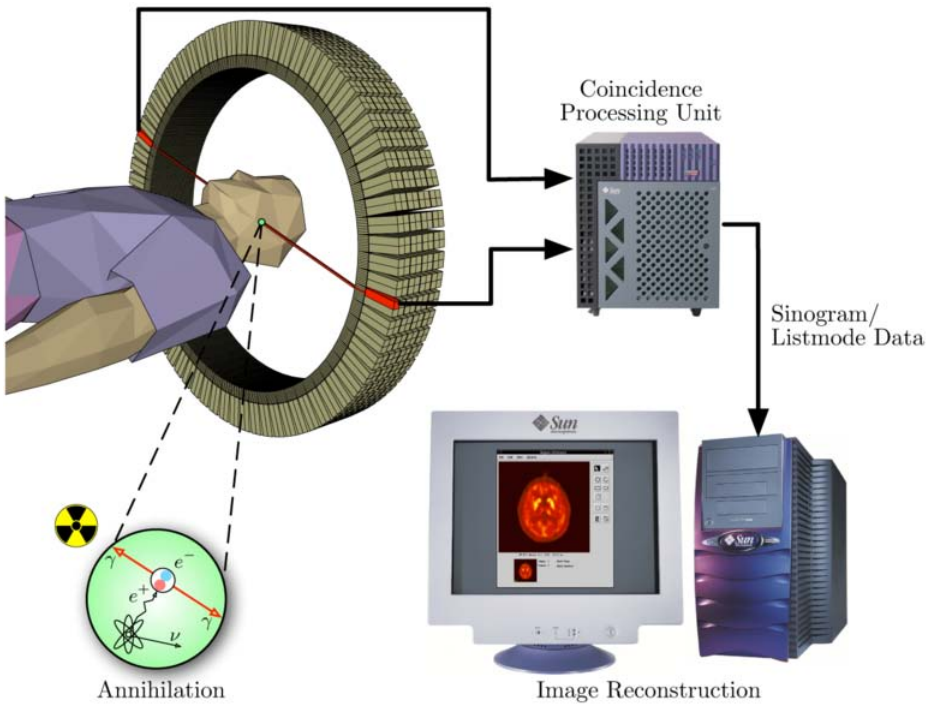

Figure 2-1 Principles of PET: starting with the annihilation process through registering the photons at the scanner ring until the final image reconstruction (reproduced from Dr. Jens Langner's thesis, http://en.wikipedia.org/wiki/File:PET-schema.png).

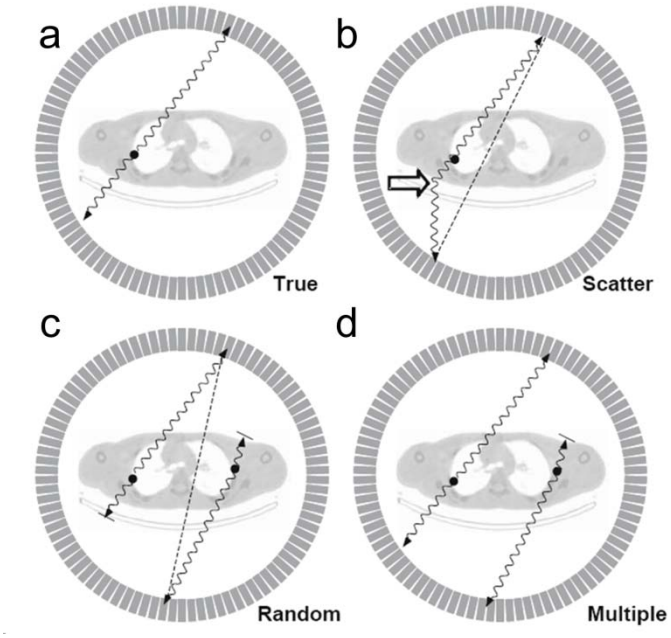

Figure 2-2 Illustration of the four main types of coincidence event. The black dot indicates the source of positron annihilation. (a) a true coincidence; (b) a scattered event where one or both of the photons undergo a Compton interaction (indicated by the open arrow); (c) a random or accidental coincidence arising from two positrons in which one of the photons from each positron annihilation is counted; (d) a multiple coincidence arising from two positron annihilations in which three events are counted. In the case of (b) and (c), the mis-assigned line of response is indicated by the dashed line (reproduced from [68]).

For an actual PET scan, true coincidences and the undesirable events (about total 10^6 to 10^9 events) are all detected. This has a degrading effect on the measurement, so these undesirable events are corrected for a number of factors in order to represent as closely as possible the true condition of positron emission. The final output of the PET imaging is a three-dimensional image, where the signal intensity in any particular image voxel is proportional to the amount of the tracer in that voxel. The voxel value would be converted to true amount of the tracer in the voxel through cross calibration. Hence, PET images allow feasible visualization of three-dimensional spatial quantitative distribution of the tracer in a living subject. If the PET scan is conducted with a dynamic imaging protocol, a time sequence of

image frames can extract the tissue concentration of tracer as a function of time. The time-activity curve (TAC) can be derived from a region of interest (ROI) that can be as small as a voxel, which is demonstrated in Figure 2-3. The open circle denotes the measured tracer time-activity from each frame of the dynamic PET image. The frame reference time is often set to the midpoint of the actual frame duration. In this case, the acquisition time point for each time-activity sample of TAC notes as mid-scan time.

After obtaining the TACs from the dynamic PET images, the use of methods based on kinetic modeling can further derive simple kinetic parameters abstractly describing complicated biological processes *in vivo*.

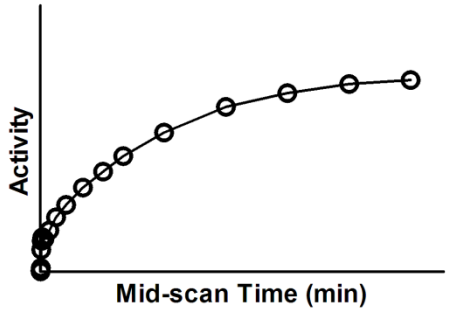

Figure 2-3 A tracer time-activity curve obtained from the dynamic PET images.

2.2 Kinetic Modeling

Kinetic modeling, which originates from pharmacokinetics and uses modeling technique to describe complicated kinetic process, is a highly versatile tool for estimating biological parameters for an underlying model in functional imaging. The kinetic model is established according to physiological and biochemical processes for a dedicated tracer in an abstracted matter. The derived simple kinetic parameters can be directly used in the objective evaluation of physiological processes.

According to mathematical characteristics, the tracer kinetic models can be classified into non-compartmental model [69], compartmental model [70], and distributive model [71]. The models can also be categorized into linear and nonlinear models. Among these models, the linear compartment model is more popular in practice, because of its attractive mathematical properties in deriving parameter estimations. The major principle of compartment models is using a series of interconnected homogeneous pools to describe the kinetics of a specific tracer. In the following contents, all the models are linear compartmental models.

[^{18}F]Fluoro-2-deoxy-2-D-glucose (FDG), a radioactive analog of glucose, is one widely used PET tracer. FDG-PET has been widely used in clinical diagnosis according to the changes of glucose metabolism in main areas, such as cancer, cardiovascular diseases, neurodegenerative disorders and other central nervous system disorders, and infectious, autoimmune, and inflammatory diseases [72-75]. Due to its popularity, FDG-PET is chosen to as an example to introduce kinetic modeling techniques in PET imaging in this thesis.

2.2.1 Compartmental Model

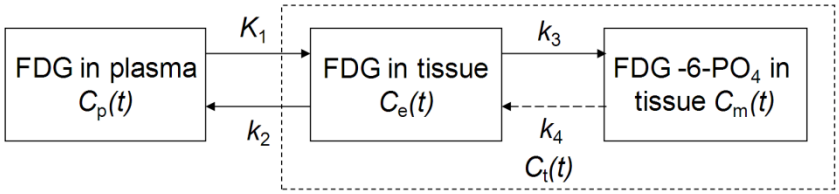

Figure 2-4 The three-compartment four-parameter FDG model. The first compartment is for the FDG in plasma; the second one is for the FDG in tissue; the third one is for the phosphorylated FDG-6-PO_4 in tissue.

The FDG distribution in the living system is frequently analyzed by the three-compartment and four-parameter model, which is originally proposed by Sokoloff *et*

al [76], then further extended by other researchers [77, 78]. The three-compartment four-parameter FDG model is shown in Figure 2-4.

This general FDG model can be described by the differential equations as in (2-1).

$$\begin{cases} \dfrac{dC_{\mathrm{e}}(t)}{dt} = K_1 C_{\mathrm{p}}(t) - (k_2 + k_3) C_{\mathrm{e}}(t) + k_4 C_{\mathrm{m}}(t) \\ \dfrac{dC_{\mathrm{m}}(t)}{dt} = k_3 C_{\mathrm{e}}(t) - k_4 C_{\mathrm{m}}(t) \end{cases} \tag{2-1}$$

where $C_{\mathrm{e}}(t)$ and $C_{\mathrm{m}}(t)$ are the TACs respectively for FDG and FDG-6-PO_4 in tissue; $C_{\mathrm{p}}(t)$ denotes the PTAC of FDG, which is used as a input function in tracer kinetic modeling. K_1, k_2, k_3, and k_4 are the rate constants of the compartment model, which describe the exchanges of tracer between compartments. The units of K_1 is usually set to as ml/min/g, while the units of k_2, k_3, and k_4 is 1/min. The total TTAC of FDG, $C_{\mathrm{t}}(t)$, can be simply described as the sum of $C_{\mathrm{e}}(t)$ and $C_m(t)$, i.e. $C_{\mathrm{t}}(t) = C_{\mathrm{e}}(t) + C_{\mathrm{m}}(t)$.

By solving the differential equations in (2-1), the relationships between the TAC of each compartment and input function can be expressed by (2-2).

$$\begin{cases} C_{\mathrm{e}}(t) = \dfrac{K_1}{\alpha_2 - \alpha_1}\left[(k_4 - \alpha_1)e^{-\alpha_1 t} + (\alpha_2 - k_4)e^{-\alpha_2 t}\right] \otimes C_{\mathrm{p}}(t) \\ C_{\mathrm{m}}(t) = \dfrac{K_1 k_3}{\alpha_2 - \alpha_1}(e^{-\alpha_1 t} - e^{-\alpha_2 t}) \otimes C_{\mathrm{p}}(t) \end{cases} \tag{2-2}$$

where α_1 and α_2 are macro parameters derived from the combination of the rate constants k_1, k_2, k_3, and k_4, as shown in (2-3).

$$\alpha_1, \alpha_2 = \left(k_2 + k_3 + k_4 \mp \sqrt{(k_2 + k_3 + k_4)^2 - 4k_2 k_4}\right)/2 \tag{2-3}$$

A fifth parameter, V_{p}, fractional plasma volume in vascular space, is often included to address vascular effects from surrounding vascular systems [79, 80]. In

this case, the total TTAC, $C_{\mathrm{t}}(t)$, can be modified as the sum of $C_e(t)$ and $C_m(t)$ plus a fraction of the PTAC, $C_{\mathrm{p}}(t)$, which is given by (2-4).

$$\begin{aligned} C_{\mathrm{t}}(t) &= \big(C_{\mathrm{e}}(t) + C_{\mathrm{m}}(t)\big) + V_{\mathrm{p}}C_{\mathrm{p}}(t) \\ &= \frac{K_1}{\alpha_2 - \alpha_1}[(k_3 + k_4 - \alpha_1)e^{-\alpha_1 t} \\ &\quad + (\alpha_2 - k_3 - k_4)e^{-\alpha_2 t}] \otimes C_{\mathrm{p}}(t) + V_{\mathrm{p}}C_{\mathrm{p}}(t) \end{aligned} \tag{2-4}$$

Once the rate constants of the FDG model are estimated, the metabolic rate of glucose (*MRGlc*) of the tissue, which is an important macro biological parameter in analysing glucose metabolism, can be estimated using (2-5).

$$MRGlc = \frac{C_{\mathrm{glc}}}{LC}\frac{K_1 k_2}{k_2 + k_3} \tag{2-5}$$

where, C_{glc} is the plasma glucose concentration in blood; LC is the lumped constant accounting for the differences in the transport and phosphorylation between FDG and glucose; $\frac{K_1 k_2}{k_2 + k_3}$ is usually referred to the influx rate, K_{i}.

2.2.2 Parameter Estimation

With the measurements from PET images and blood samples, the appropriate tracer kinetic model allows for estimating the specific biological parameter, e.g. *MRGlc* given by (2-5). The parametric image can be generated by the predicted biological parameters covering the three-dimensional image volume. Figure 2-5 illuminates the data flow to construct parametric image, taking an example of the estimation cerebral metabolic rate of glucose (*CMRGlc*) in FDG-PET studies. Firstly, the kinetic of FDG uptake in the brain is recorded in a series of frames of dynamic PET images. During the dynamic PET imaging, the arterial blood samples are collected from the blood vessels. The PTAC is then derived from the blood samples

and used as an input function in tracer kinetic modeling. A ROI of a certain tissue is placed in PET images to obtain a TTAC that usually is the average of the TACs of the voxles within the ROI. Based on the general FDG model, the micro-parameters, K_1, k_2, k_3, and k_4, are estimated by fitting the model outputs to the measured TTAC. Finally, *CMRGlc* can be estimated using the rate constants, the endogenous glucose concentration and the lump constant. If the ROI is as small as voxel in the PET images, *CMRGlc* can be calculated voxel by voxel to generate the corresponding three-dimensional parametric image.

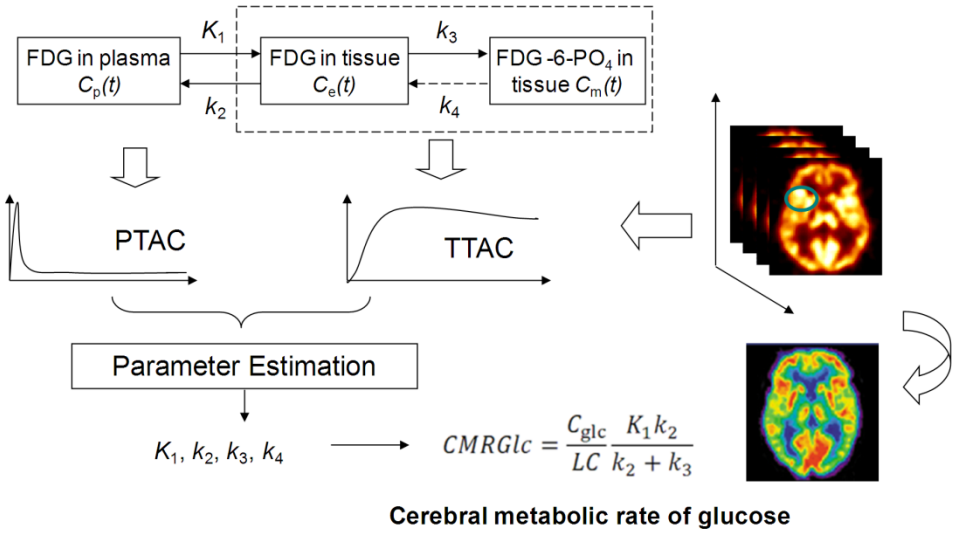

Figure 2-5 The data flow to construct the parametric image of *CMRGLc* (reproduced from [26]).

To obtain the parametric image relies on not only the available dynamic information from measurements of blood samples and PET images but also the suitable curve fitting algorithm for the parameter estimation. As the solution of differential equations is nonlinear, it is required a nonlinear fitting routine to estimate the parameters from the measured data. The most direct curve fitting method is the nonlinear least squares method, which is going to be introduced with other kinetic analysis methods in the following sections.

2.3 Kinetic Analysis Methods

2.3.1 Nonlinear Least Squares Method

Nonlinear least squares (NLS) method is attempting to fit a given TTAC through nonlinear iterative process, which is referred to provide "optimal estimates" of rate constants due to its statistical reliability, as shown in Figure 2-6 [26].

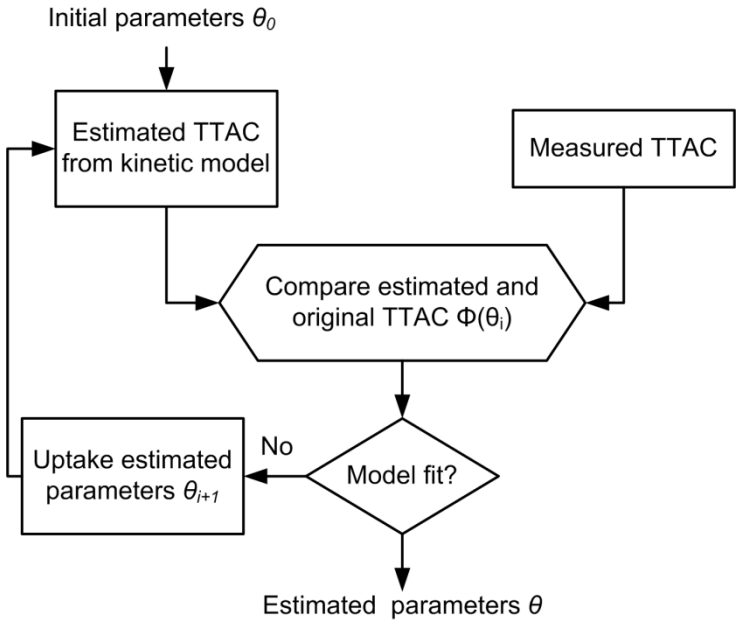

Figure 2-6 The iterative process for fitting model outputs to measurements (reproduced from [26]).

The core of NLS is to minimize an objective function defined as the sum of squared differences between estimated and measured TTACs, which is given by (2-6).

$$\Phi(\theta_i) = \sum_{j=1}^{N} \left[C_t^E(t_j) - C_t^M(t_j) \right]^2 \tag{2-6}$$

where θ_i is the vector of estimated parameters in the i^{th} iteration; N is the number of frames in PET images; $C_t^E(t_j)$ and $C_t^M(t_j)$ are the estimated and measured time-activities at the mid-scan time t_j.

In each iteration, the estimated parameters θ_i are adjusted to θ_{i+1} using the multidimensional optimization methods, such as Newton-Gauss or Levenberg-Marguardt algorithms. The entire process is terminated when the objective function reaches its minimum. The final estimated parameters are regarded as the result of NLS method. Because random statistical noise exits in the measurements of PET images and shorter frame duration would induce low signal to noise ratio (SNR), an appropriate weighted term is usually included in the objective function as given by (2-7). These weights can be chosen to be proportional to the imaging durations or to the inverse of variance of the measurements [26]. This approach could be referred to as weighted nonlinear least squares (WNLS) method.

$$\Phi_{\mathrm{w}}(\theta_i) = \sum_{j=1}^{N} w_j \left[C_{\mathrm{t}}^{\mathrm{E}}(t_j) - C_{\mathrm{t}}^{\mathrm{M}}(t_j) \right]^2 \tag{2-7}$$

where w_j is the relative weight for each imaging frame.

WNLS method can provide statistically reliable results for parameter estimations in tracer kinetic analysis. Meanwhile, WNLS method has been integrated and improved in many quantification software packages, such as Kinetic Imaging System (KIS) [81], COMKAT [82], and SAAM II [83], *et al*. However, WNLS has the disadvantage that the estimated results are relying on the initial guess of parameters given at the beginning. WNLS process may be trapped in local minima for inappropriate initial parameters. Furthermore, the choice of initials and iterative processes of WNLS cause a heavy computational expense. Thus, WNLS is impractical for the construction of parametric images.

2.3.2 Linear Least Squares Method

To address the shortcoming of initialization in WNLS method, the linear least squares (LLS) method has been developed for the computational efficient parameter estimation without requirement of initial guess [84]. According to the differential equations derived from the three-compartment four-parameter FDG model given by (2-1), the differential equation for $C_{\mathrm{t}}(t)$ can be converted into (2-8).

$$\frac{d^2C_{\mathrm{t}}(t)}{dt^2} = K_1\frac{dC_{\mathrm{p}}(t)}{dt} + K_1(k_3+k_4)C_{\mathrm{p}}(t) - (k_2+k_3+k_4)\frac{dC_{\mathrm{t}}(t)}{dt} - k_2k_4C_{\mathrm{t}}(t) \tag{2-8}$$

This differential equation can be expressed by the second-order integration for N-frame imaging protocol with the measurement noise terms, as shown in (2-9).

$$\begin{cases} C_{\mathrm{t}}(t_1) = P_1\int_0^{t_1}C_{\mathrm{p}}(\tau)d\tau + P_2\int_0^{t_1}\int_0^{t}C_{\mathrm{p}}(\tau)d\tau^2 + P_3\int_0^{t_1}C_{\mathrm{t}}(\tau)d\tau \\ \qquad\qquad +P_4\int_0^{t_1}\int_0^{t}C_{\mathrm{t}}(\tau)d\tau^2 + \varepsilon_1 \\ C_{\mathrm{t}}(t_2) = P_1\int_0^{t_2}C_{\mathrm{p}}(\tau)d\tau + P_2\int_0^{t_2}\int_0^{t}C_{\mathrm{p}}(\tau)d\tau^2 + P_3\int_0^{t_2}C_{\mathrm{t}}(\tau)d\tau \\ \qquad\qquad +P_4\int_0^{t_2}\int_0^{t}C_{\mathrm{t}}(\tau)d\tau^2 + \varepsilon_2 \\ \qquad\qquad \vdots \\ C_{\mathrm{t}}(t_{\mathrm{N}}) = P_1\int_0^{t_{\mathrm{N}}}C_{\mathrm{p}}(\tau)d\tau + P_2\int_0^{t_{\mathrm{N}}}\int_0^{t}C_{\mathrm{p}}(\tau)d\tau^2 + P_3\int_0^{t_{\mathrm{N}}}C_{\mathrm{t}}(\tau)d\tau \\ \qquad\qquad +P_4\int_0^{t_{\mathrm{N}}}\int_0^{t}C_{\mathrm{t}}(\tau)d\tau^2 + \varepsilon_{\mathrm{N}} \end{cases} \tag{2-9}$$

where $P_1 = K_1$, $P_2 = K_1(k_3+k_4)$, $P_3 = -(k_2+k_3+k_4)$, and $P_4 = -k_2k_4$; $t_i(i = 1,2,\dots N)$ denotes the mid-scan time for i[th] imaging frame; ε_i $(i = 1,2,\dots N)$ is the corresponding measurement noise.

These equations can be rearranged into the matrix form expressed by (2-10).

$$\mathrm{y} = X\theta_{\mathrm{LLS}} + \varepsilon \tag{2-10}$$

where $y = [C_t(t_1), C_t(t_2), \dots C_t(t_N)]^T$, $\theta_{LLS} = [P_1, P_2, P_3, P_4]^T$, $\varepsilon = [\varepsilon_1, \varepsilon_2, \dots \varepsilon_N]^T$,

and $X = \begin{bmatrix} \int_0^{t_1} C_p(\tau)d\tau & \int_0^{t_1}\int_0^{t_1} C_p(\tau)d\tau^2 & \int_0^{t_1} C_t(\tau)d\tau & \int_0^{t_1}\int_0^{t_1} C_t(\tau)d\tau^2 \\ \int_0^{t_2} C_p(\tau)d\tau & \int_0^{t_2}\int_0^{t_2} C_p(\tau)d\tau^2 & \int_0^{t_2} C_t(\tau)d\tau & \int_0^{t_2}\int_0^{t_2} C_t(\tau)d\tau^2 \\ \vdots & \vdots & \vdots & \vdots \\ \int_0^{t_N} C_p(\tau)d\tau & \int_0^{t_N}\int_0^{t_N} C_p(\tau)d\tau^2 & \int_0^{t_N} C_t(\tau)d\tau & \int_0^{t_N}\int_0^{t_N} C_t(\tau)d\tau^2 \end{bmatrix}$.

Hence, the estimation of θ_{LLS} can be derived using (2-11).

$$\hat{\theta}_{LLS} = (X^T X)^{-1} X^T Y \tag{2-11}$$

After getting $\hat{\theta}_{LLS}$, the micro-parameters of the model can be estimated to derive the biological parameter of interest (e.g. *MRGlc*).

The LLS method does not require any optimization or prior initial parameters. However, statistically dependent error terms result in the potentially biased estimation of the LLS method. As a result, generalized linear least squares (GLLS) method has been proposed to deal with the influence of error terms in LLS method by applying the auto-regressive filter [85, 86]. The detail process of GLLS method has been expressed in the references [85, 86]. Finally, the GLLS method accompanying with LLS can provide a computationally efficient approach to generate the parametric images.

2.3.3 Graphic Analysis

The graphic analysis techniques employ simple linear regression to derive the relevant biological parameters without iterative process. The biological parameter of interest is usually proportional to the slope or intercept of the linear regression. The graphic analysis techniques have the advantages of computational efficiency, feasibility, and high reliability. They are playing an important role in the quantitative analysis of PET images [87].

A. Patlak Graphic Analysis

Patlak graphical analysis (PGA) is the first proposed graphic analysis techniques with the assumption of $k_4 = 0$ for a three-compartment four-parameter FDG model [88]. Thus, the differential equations in (2-1) can be transformed into the new expressions in (2-12).

$$\begin{cases} \dfrac{dC_{\mathrm{e}}(t)}{dt} = K_1 C_{\mathrm{p}}(t) - (k_2 + k_3) C_{\mathrm{e}}(t) \\ \dfrac{dC_{\mathrm{m}}(t)}{dt} = k_3 C_{\mathrm{e}}(t) \\ C_{\mathrm{t}}(t) = C_{\mathrm{e}}(t) + C_{\mathrm{m}}(t) \end{cases} \tag{2-12}$$

The TTAC, $C_{\mathrm{t}}(t)$, which is the sum of $C_{\mathrm{e}}(t)$ and $C_{\mathrm{m}}(t)$, can be expressed by (2-13).

$$\frac{dC_{\mathrm{t}}(t)}{dt} = \frac{K_1 k_3}{k_2 + k_3} C_{\mathrm{p}}(t) + \frac{k_2}{k_2 + k_3} \frac{dC_{\mathrm{e}}(t)}{dt} \tag{2-13}$$

After performing the integration and dividing by $C_{\mathrm{p}}(t)$ in both sides, (2-13) could be reformed as (2-14).

$$\frac{C_{\mathrm{t}}(t)}{C_{\mathrm{p}}(t)} = \frac{K_1 k_3}{k_2 + k_3} \frac{\int_0^t C_{\mathrm{p}}(\tau) d\tau}{C_{\mathrm{p}}(t)} + \frac{k_2}{k_2 + k_3} \frac{C_{\mathrm{e}}(t)}{C_{\mathrm{p}}(t)} \tag{2-14}$$

If there is a sufficient long time post tracer administration ($t > t^*$), it can be assumed that equilibrium has been reached between tracer concentrations in the plasma and the free tissue. That is, $C_{\mathrm{e}}(t)/C_{\mathrm{p}}(t)$ tends to be a constant when $t > t^*$. The simple relationship between PTAC and TTAC can be expressed by (2-15).

$$\frac{C_{\mathrm{t}}(t)}{C_{\mathrm{p}}(t)} = K_i \frac{\int_0^t C_{\mathrm{p}}(\tau) d\tau}{C_{\mathrm{p}}(t)} + I, t > t^* \tag{2-15}$$

where the slope $K_{\mathrm{i}} = \frac{K_1 k_3}{k_2 + k_3}$ is the influx rate; I is the constant intercept, which could equal with the sum of distribution volume of $C_e(t)$ and the fractional plasma volume

V_p if considering the vascular effects from surrounding vascular systems; t^* is sufficient long time when the equilibrium is reached between tracer concentrations in the plasma and the free tissue.

In this case, the estimate of K_i can be simply derived by the slope of the linear plot of $\frac{\int_0^t C_\mathrm{p}(\tau)d\tau}{C_\mathrm{p}(t)}$ vs. $\frac{C_\mathrm{t}(t)}{C_\mathrm{p}(t)}$. The process of PGA is shown in Figure 2-7. In clinical applications, the value of t usually ranges from approximately 15 to 60 minutes post tracer administration in FDG-PET studies [89]. In some small-animal studies the range of t has been suggested as 3-22 minute after tracer injection [90].

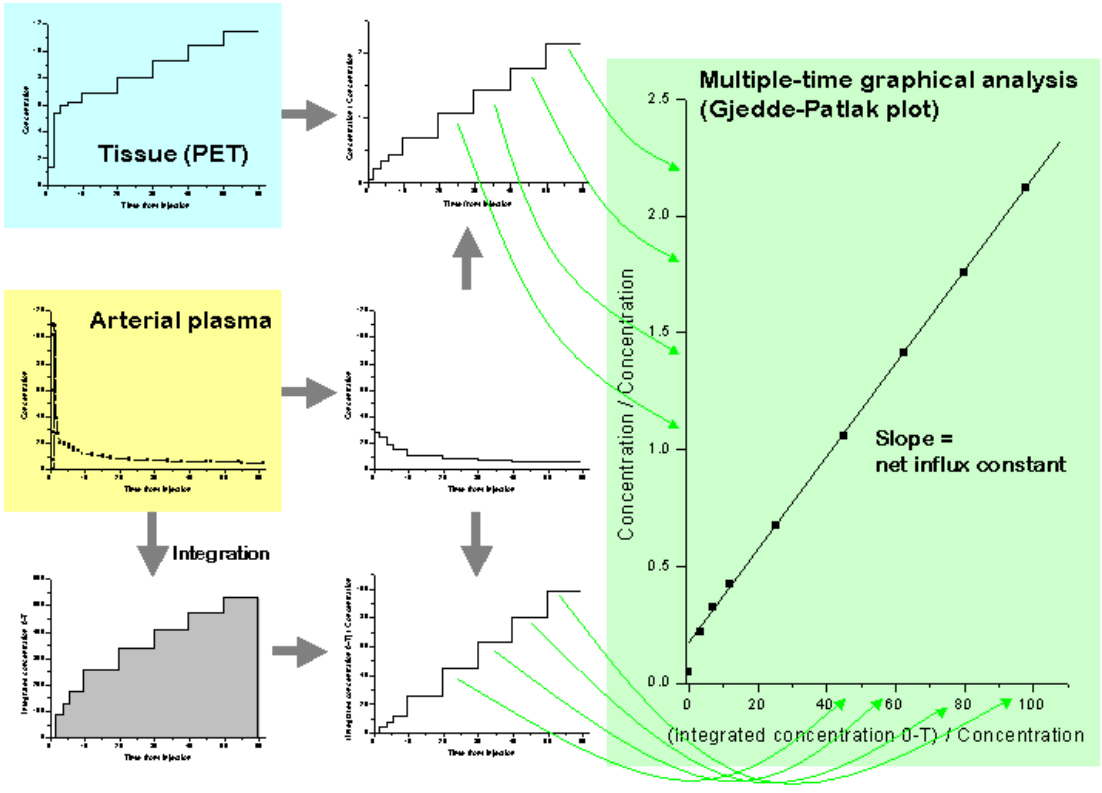

Figure 2-7 The process of Patlak graphic analysis (from Turku PET Center, http://www.turkupetcentre.net/modelling/guide/patlak_plot.html). In the largest figure, the y-axis contains apparent distribution volumes, i.e. the ratio of tracer concentrations in tissue and in plasma. On x-axis is normalized plasma integral, i.e. the ratio of the integral of plasma concentration and the plasma concentration.

B. Logan Graphic Analysis

The Logan graphic analysis (LGA) has been proposed by taking account of reversible compartment [91, 92]. Based on the differential equations in (2-1), the total TTAC can be expressed by (2-16).

$$C_{\mathrm{t}}(t) = \frac{K_1}{k_2}\frac{k_3 + k_4}{k_4} C_{\mathrm{p}}(t) - \frac{k_3 + k_4}{k_2 k_4}\frac{dC_{\mathrm{t}}(t)}{dt} - \frac{1}{k_4}\frac{dC_{\mathrm{m}}(t)}{dt} \tag{2-16}$$

After performing the integration and dividing by $C_{\mathrm{t}}(t)$ in the both sides, (2-16) could be rewritten as (2-17).

$$\frac{\int_0^t C_{\mathrm{t}}(\tau)\, d\tau}{C_{\mathrm{t}}(t)} = \frac{K_1}{k_2}\frac{k_3 + k_4}{k_4}\frac{\int_0^t C_{\mathrm{p}}(\tau)\, d\tau}{C_{\mathrm{t}}(t)} - \frac{k_3 + k_4}{k_2 k_4} - \frac{1}{k_4}\frac{C_{\mathrm{m}}(t)}{C_{\mathrm{t}}(t)} \tag{2-17}$$

Similar with the assumption in PGA method, the ratio between $C_{\mathrm{m}}(t)$ and $C_{\mathrm{t}}(t)$ can be a constant after reaching the equilibrium ($t > t^*$). The linear equation is given by (2-18).

$$\frac{\int_0^t C_{\mathrm{t}}(\tau)\, d\tau}{C_{\mathrm{t}}(t)} = V_d \frac{\int_0^t C_{\mathrm{p}}(\tau)\, d\tau}{C_{\mathrm{t}}(t)} + I \tag{2-18}$$

where the slope V_d denotes the volume of distribution and the intercept I is a constant. If $C_{\mathrm{m}}(t)$ is far less than $C_{\mathrm{t}}(t)$ after the equilibrium is reached, the K_1 can be calculated by $K_1 \approx -V_{\mathrm{d}}/I$.

When there is a reference tissue model available, LGA can be extended to non-invasive LGA (see **2.5.2**) for deriving binding potential (BP) in neuroreceptor studies. Furthermore, the prior knowledge of underlying tracer kinetics is not necessary for applying LGA for deriving the volume of distribution (V_{d}) [93].

2.4 Semi-Quantitative Parameters

In addition to the dynamic PET imaging, static imaging protocol that only collects one image frame is widely applied in PET studies. Static PET imaging is especially attractive to conduct whole-body scans for human in a short period. For example, it takes about 16 minutes for a modern PET/CT scanner to perform the whole-body scan of human with 8 beds. The static PET imaging is quite simple, and also increases the subject throughput both in clinical examinations and pre-clinical studies. However, due to only one frame is available, the static-imaging related parameters, including standard uptake value (SUV), fraction uptake rate (FUR), and percent injected-dose per gram of tissue (%ID/g), are referred to as semi-quantitative parameters.

SUV is a widely used semi-quantitative parameter in clinical applications especially for FDG-PET because of its computational efficiency and clinical practicality. It can be calculated by (2-19). However, the accuracy of SUV could be affected by many factors such as patient size, standardized measurement time, plasma glucose level and partial volume effects *etc* [28, 94].

$$SUV = \frac{C_t(T)}{ID/BW} \tag{2-19}$$

where $C_t(T)$ is the tracer time-activity of a given ROI at time T, ID is the injected dose of tracer, and BW is the bodyweight of the subject.

Another simple semi-quantitative index is FUR, which is calculated by (2-20) [95, 96]. It is similar with SUV but requires a continuous blood sampling in the period from the injection to the imaging time. The application of FUR may suffer from the problems caused by the invasive approach to get blood samples.

$$FUR = \frac{C_{\mathrm{t}}(T)}{\int_0^T C_{\mathrm{p}}(\tau)d\tau} \tag{2-20}$$

where $C_{\mathrm{t}}(T)$ is the tissue-time activity at time T; $C_{\mathrm{p}}(t)$ is the tracer PTAC obtained from the blood sampling.

The relationship between FUR and SUV is deduced and shown in (2-21) [97]. It is found that the estimated result of FUR is highly related with SUV if the PTAC is known.

$$FUR = SUV \cdot k_{\mathrm{p}}(T) \cdot V_0, \qquad k_p(T) = \frac{C_{\mathrm{p}}(0)}{\int_0^T C_{\mathrm{p}}(\tau)d\tau} \tag{2-21}$$

where $k_{\mathrm{p}}(T)$ is the average plasma clearance rate at time T; $C_{\mathrm{p}}(0)$ is the initial tracer time-activity in plasma; and V_0 is the initial distribution volume of tracer.

One more useful semi-parameter is $\%\,\mathrm{ID/g}$, which is a way of normalizing the single frame at a given location for the amount of tracer injected into the subject with an assumption that the injected dose is available for the entire area of the subject [70]. It is calculated according to (2-22).

$$\%\,\mathrm{ID/g} = C_{\mathrm{t}}(T) \cdot \frac{V}{W} \cdot \frac{1}{ID} \cdot 100\% \tag{2-22}$$

where $C_{\mathrm{t}}(T)$ is the tissue time-activity at time T, ID is the injected dose. W and V are the weight and volume of the tissue. The density of tissue is usually assumed as ~1g/ml.

The relationship between $\%\,\mathrm{ID/g}$ and SUV can be expressed by (2-23).

$$\%\,\mathrm{ID/g} = \frac{SUV}{BW} \cdot 100\% \tag{2-23}$$

Because the static PET images only have one frame and neglect the dynamic information of tracer kinetics, these semi-quantitative parameters don't reflect the

changes of tracer delivery, uptake, trapping, competition with other molecules and routs of clearance [70].

2.5 Noninvasive Methods

Generally, frequent invasive arterial blood sampling is required to derive PTAC in tracer kinetic modeling. However, the procedure of invasive arterial blood sampling may discomfort patients even though the arterialized-venous method is used to avoid the harmful arterial puncture [77]. Moreover, the invasive blood sampling induces extra radiations and risks associated with handling blood samples to the operators. Many challenges exist for invasive blood sampling in small-animal investigations due to the small-size blood vessel and limited blood volume of the subjects. Thus, efforts have been paid to develop non-invasive methods in quantifications of dynamic PET images, to avoid or use less blood samples.

2.5.1 Image-Derived Input Function

The image-derived input function (IDIF) method relies on placing a sufficiently large vascular structure in the imaging FOV. It is direct and convenient without extra supporting information. The blood TAC can be obtained from a ROI simply placed on the large blood cavity such as the left ventricle of heart [98]. The blood TAC can be transferred into PTAC using several methods [90, 99, 100]. However, the measured blood TAC from one predefined ROI is usually affected by the spillover effects from the adjacent structures due to the limited spatial resolution of PET. Especially for the FDG PET studies using the ROI of left ventricle, the spillover from the myocardium can introduce a large bias to the estimated IDIF.

Hence, the IDIF with correction of the spillover effects has been well established by using a supplemental ROI in the myocardium [52, 53].

The FDG dynamic behavior in myocardium has been characterized by the three-compartment four-parameter FDG model whose corresponding differential equations are given in (2-1) [101]. Two ROIs are carefully delineated in the blood cavity (e.g. left ventricle) and the myocardium to get the measured TACs. The TAC measured from the ROI of the myocardium is a combination of the TTAC of myocardium and the spillover from blood cavity. Similarly, the TAC measured from the ROI of blood contains the spillover from myocardium and PTAC. These relationships can be described by (2-24).

$$\begin{cases} \tilde{C}_{\mathrm{t}}(t) = C_{\mathrm{t}}(t) + f_{\mathrm{m}}^{\mathrm{b}} C_{\mathrm{p}}(t) \\ \tilde{C}_{\mathrm{b}}(t) = f_{\mathrm{b}}^{\mathrm{m}} C_{\mathrm{t}}(t) + C_{\mathrm{p}}(t) \end{cases} \tag{2-24}$$

where $\tilde{C}_{\mathrm{t}}(t)$ and $\tilde{C}_{\mathrm{b}}(t)$ are the measured TACs of myocardium and blood, respectively. $C_{\mathrm{t}}(t)$ is the TTAC and $C_{\mathrm{p}}(t)$ is the PTAC. $f_{\mathrm{m}}^{\mathrm{b}}$ and $f_{\mathrm{b}}^{\mathrm{m}}$ are the mixing coefficients reflected the spillover effects between blood and myocardium.

By introducing (2-24), the model in (2-1) can be represented by the measured TACs, as shown in (2-25) [10].

$$\begin{cases} \dfrac{dC_{\mathrm{e}}(t)}{dt} = -[(k_2 + k_3) + K_1 f_{\mathrm{b}}^{\mathrm{m}}] C_{\mathrm{e}}(t) + (k_4 - K_1 f_{\mathrm{b}}^{\mathrm{m}}) C_{\mathrm{m}}(t) + K_1 \tilde{C}_{\mathrm{b}}(t) \\ \dfrac{dC_{\mathrm{m}}(t)}{dt} = k_3 C_{\mathrm{e}}(t) - k_4 C_{\mathrm{m}}(t) \\ \tilde{C}_{\mathrm{t}}(t) = \left(1 - f_{\mathrm{b}}^{\mathrm{m}} f_{\mathrm{m}}^{\mathrm{b}}\right) C_{\mathrm{t}}(t) + f_m^{\mathrm{b}} \tilde{C}_{\mathrm{b}}(t) \end{cases} \tag{2-25}$$

The input function with spillover correction can then be expressed by (2-26).

$$C_{\mathrm{p}}(t) = \frac{\tilde{C}_{\mathrm{b}}(t) - f_{\mathrm{b}}^{\mathrm{m}} \tilde{C}_{\mathrm{t}}(t)}{1 - f_{\mathrm{b}}^{\mathrm{m}} f_{\mathrm{m}}^{\mathrm{b}}} \tag{2-26}$$

By considering (2-25) and (2-26) together, $\tilde{C}_b(t)$ was used as the new input for the represented model with the dual outputs of $\tilde{C}_t(t)$ and $C_p(t)$. There were six unknown parameters in this represented model: four rate constants (k_1, k_2, k_3, and k_4) and two spillover factors (f_m^b and f_b^m). These parameters can be estimated using WNLS method.

This non-invasive approach is appropriate to estimate the IDIF for the thoracic PET imaging or whole-body PET imaging which includes the heart in FOV. Otherwise, the ROI can be placed on the other sufficiently large vessels for deriving blood TAC, such as the intracranial vessels [102, 103], the hepatic arteries as well as the portal vein [104, 105], carotid artery [106] and so on. In some small-animal studies, the liver TAC derived from the PET images has been used as a surrogate input function based on the assumption that the liver is a large blood pool and has relatively low tracer uptakes [107, 108].

2.5.2 Reference Tissue Model

The reference tissue model has been introduced to estimate binding potential for quantifying the neuroreceptor study without measuring arterial input function [54, 55]. Its principle is the assumption that there is a reference tissue without specific binding of the ligand while the levels of nonspecific binding are the same in the reference and target tissues. The neuroreceptor kinetic in target tissue can be described by three-compartment model while the two-compartment model is used in the reference tissue. These models are depicted in Figure 2-8.

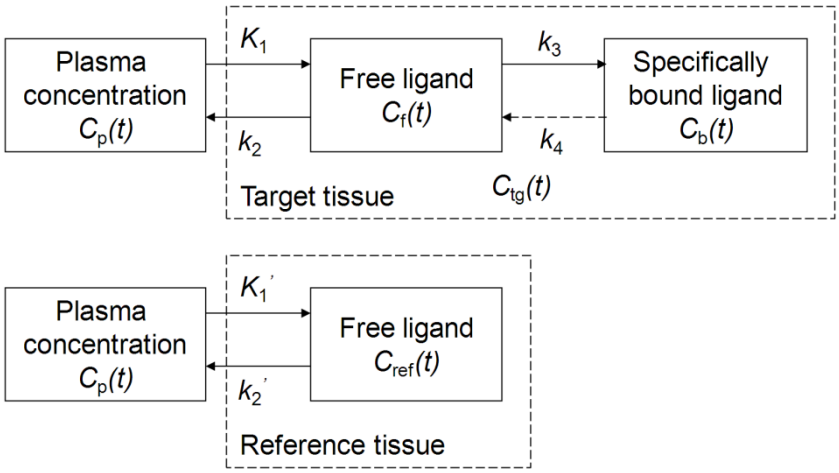

Figure 2-8 The three-compartment model for the target tissue and two-compartment model for the reference tissue in neuroreceptor study (reproduced from [26]).

The corresponding differential equations are given in (2-27).

$$\begin{cases} \dfrac{dC_{\mathrm{ref}}(t)}{dt} = K_1' C_{\mathrm{p}}(t) - k_2' C_{\mathrm{ref}}(t) \\ \dfrac{dC_{\mathrm{f}}(t)}{dt} = K_1 C_{\mathrm{p}}(t) - (k_2 + k_3) C_{\mathrm{f}}(t) + k_4 C_{\mathrm{b}}(t) \\ \dfrac{dC_{\mathrm{b}}(t)}{dt} = k_3 C_{\mathrm{f}}(t) - k_4 C_{\mathrm{b}}(t) \end{cases} \tag{2-27}$$

where $C_{\mathrm{p}}(t)$ is the PTAC; $C_{\mathrm{ref}}(t)$ is the TTAC of the reference tissue; $C_{\mathrm{f}}(t)$ is the TAC of free ligand; and $C_{\mathrm{b}}(t)$ is the TAC of specially bound ligand. K_1', k_2', K_1, k_2, k_3 and k_4 are the rate constants for the models. The total TTAC in target tissue is the sum of $C_{\mathrm{f}}(t)$ and $C_{\mathrm{b}}(t)$, namely $C_{\mathrm{tg}}(t) = C_{\mathrm{f}}(t) + C_{\mathrm{b}}(t)$.

According to the first equation in (2-27), $C_{\mathrm{p}}(t)$ can be described by $C_{\mathrm{ref}}(t)$. The relationship between $C_{\mathrm{tg}}(t)$ and $C_{\mathrm{p}}(t)$ can be obtained from the rest two equations. The relationship between $C_{\mathrm{t}}(t)$ and $C_{\mathrm{ref}}(t)$ can then be derived. This relationship is an equation contains six parameters. Assuming that the volumes of distribution of the nonspecifically bound tracer in reference and target tissues are the same, that is $K_1'/k_2' = K_1/k_2$, the relationship between $C_{\mathrm{tg}}(t)$ and $C_{\mathrm{ref}}(t)$ can be simplified as an equation with four parameters (R_{I}, k_2, k_3, and BP). R_{I} denotes the

relative rate of delivery as the ratio of K_1 and K_1', $R_\mathrm{I} = K_1/K_1'$. BP is the binding potential calculated as $BP = k_3/k_4$.

If the tracer kinetic of the target tissue is simply described by the two-compartment model instead of the three-compartment model, the second and third equations in (2-27) can be replaced by a single equation as (2-28).

$$\frac{dC_\mathrm{tg}(t)}{dt} = K_1 C_\mathrm{p}(t) - k_{2\mathrm{a}} C_\mathrm{tg}(t) \tag{2-28}$$

where $k_{2\mathrm{a}}$ is the apparent rate constant for transfer from specific compartment to plasma. Because the total tracer volume of distribution should be the same as that described by three-compartment model, $k_{2\mathrm{a}}$ has a relationship with BPas$K_1/k_{2\mathrm{a}} = (K_1/k_2) \cdot (1 + BP)$.

Based on this simplification, the simplified reference tissue model is derived and the relationship between $C_\mathrm{tg}(t)$ and $C_\mathrm{ref}(t)$ can be rewritten as an equation with three parameters in (2-29).

$$C_\mathrm{tg}(t) = R_\mathrm{I} C_\mathrm{ref}(t) + \left(k_2 - \frac{R_\mathrm{I} k_2}{1 + BP}\right) C_\mathrm{ref}(t) \otimes e^{-\frac{k_2 t}{1+BP}} \tag{2-29}$$

These three parameters of simplified reference tissue model can be estimated by WNLS method. In most cases, the three-parameter simplified reference tissue model can produce the stable results compared with the four-parameter reference tissue model [109].

The noninvasive LGA method based on the reference tissue model is proposed for estimating the distribution volume ratios, which can be expressed by (2-30) [93].

$$\frac{\int_0^t C_\mathrm{tg}(\tau)d\tau}{C_\mathrm{tg}(t)} = DVR \cdot \frac{\int_0^t C_\mathrm{ref}(\tau)d\tau}{C_\mathrm{tg}(t)} + I \tag{2-30}$$

where DVR denotes distribution volume ratios, which is equal to $1 + BP$ when the reference tissue and target tissue have the same degrees of nonspecific binding. I is constant when $C_{\mathrm{ref}}(t)/C_{\mathrm{tg}}(t)$ reaches equilibrium ($t > t^{*}$).

2.6 Summary

In this chapter, a brief review has been given for the principles of PET imaging as well as the basics of quantification techniques for PET images, including the tracer kinetic modeling and the semi-quantitative parameters. The non-invasive methods are also introduced in this chapter as a notable quantification technique for dynamic PET imaging. These fundamental approaches are going to be used, improved and discussed in the further investigations of this thesis.

Chapter 3

Automatic Image-Based Method with Improved SUVs for Static Small-Animal PET Imaging

3.1 Introduction

SUV is usually used to measure the tracer uptake in the quantitative analysis for static FDG-PET images. However, many factors can influence the variability of SUV as reviewed in **1.3**. Recently the impact of renal function variation has been studied for FDG-PET studies [110, 111], since SUV is regularly defined as the local target concentration normalized by injected dose per unit body weight without taking the differences in plasma FDG clearance into account [112]. As a result, changing the amount of excreted FDG by renal function could affect the estimation of SUV, even if the glucose utilization in the rest of the body stays unchanged.

On the other hand, the subject's body weight and the injected dose, which are necessary in SUV calculation, are measured separately from PET imaging. Generally, the body weight is measured by a scale, while the injected dose is

measured by a dosimeter. Because it is difficult to redo the measurement of injected dose, any missing records of injected dose would lead to the failure in the calculation of SUV. This is a notable issue in the data reutilization especially for multidisciplinary and inter-institution sharing in education and scientific research, when the data were stored in a shared database such as Mouse Quantitation Program [113]. The tumor-to-background ratio (TBR), which is calculated as the ratio of the tracer time-activity in tumor over that in normal tissue, is sometimes used as an index to quantify the tracer uptake without measurements of body weight and injected dose [114, 115]. However, to find a suitable normal tissue as background may be difficult for some oncologic images [116].

This chapter aims to develop an automatic image-based method to estimate SUV and, further, to find a way to reduce SUV variability that will eventually assist SUV for differentiation of malignancy from benign lesions. Two improved SUVs, image-derived SUV (iSUV) and modified SUV (mSUV), are evaluated in a set of mouse FDG-PET studies.

3.2 Theory of Image-Based Method with Improved SUVs

3.2.1 Automatic Image-Based Method

To conveniently derive the iSUV and mSUV, an automatic image-based method was developed to obtain the whole-body mask (composed of the bone mask, body mask and lung mask) and bladder mask based on the microCT and microPET images. These masks were used to locate the corresponding targets in the microPET and microCT images, and then to get the parameters for calculating iSUV and

mSUV. Figure 3-1 shows the flow chart of this method. The entire process was described as follows.

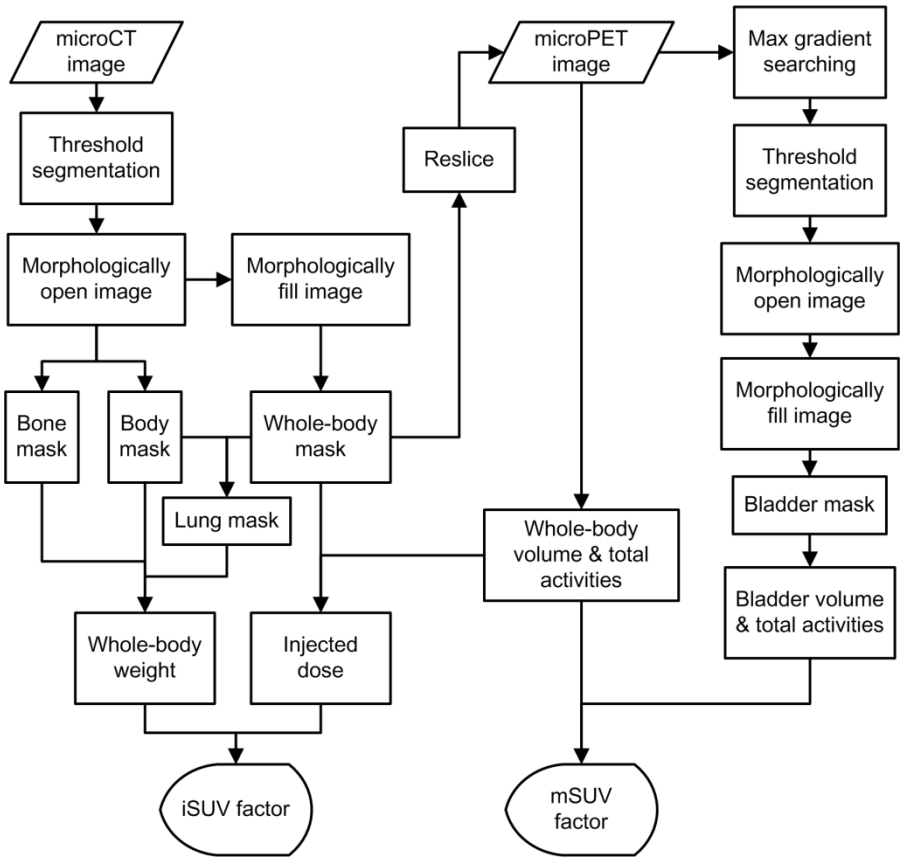

Figure 3-1 The flow chart of automatic image-based method for the estimation of iSUV and mSUV.

In the reconstructed microCT image (in Hounsfield units, HU), the threshold method was firstly utilized to segment the mouse body from background using an empirical threshold window of [-250, 4000] HU. That is, the voxels with intensity values higher than -250 HU and lower than 4000 HU were considered as belonging to the rough body mask. Within the rough body mask, the bone tissue was further segmented using another empirical threshold window of [400, 4000] HU, so that the voxels with intensity values higher than 400 HU and lower than 4000 HU were set to as the rough bone mask. These two rough masks were saved as two binary images in the same matrix dimension as the microCT image.

Secondly, the “morphological opening” operation was applied to smooth the boundary of the rough body mask and bone mask. The voxels within the body part that have low density (i.e., lung, trachea and the gas in the alimentary system) were excluded in the rough body mask at the first step. The “morphological fill” operation was then applied to fill the holes in the body mask to obtain a whole-body mask that included all the voxles within the body. The lung mask was then derived by subtracting the whole-body mask from the rough whole-body mask in the upper body. The lung mask was then refined by using the “morphological opening” operation to remove the artifacts of the trachea. Using these masks, the microCT image of the mouse body was separated into three regions, namely soft tissue, lung and bone. The details of morphological operations were expressed in Appendix B.

Next, the total numbers of voxels of the body, bone and lung regions were counted, and then the volumes were calculated by multiplying the voxel number with the voxel volume (0.008mm^3). The volumes of these different regions derived from microCT image were used to estimate the body weight of the subject. The whole-body mask was resampled into the image matrix of the microPET in order to define the whole-body region in the microPET image and estimate the injected dose. The estimated body weight was calculated as the sum of weights of the soft tissue, bone and lung regions, which is shown in (3-1). The specific densities of soft tissue, bone and lung parts were assumed as 1, 1.14 and 0.28 *g/ml*, respectively [117, 118].

$$BW_{\mathrm{e}} = V_{\mathrm{nb}} \times D_{\mathrm{nb}} + V_{\mathrm{b}} \times D_{\mathrm{b}} + V_{\mathrm{l}} \times D_{\mathrm{l}} \tag{3-1}$$

where BW_{e} is the estimated body weight; V_{nb} is the soft tissue volume; V_{b} is the bone volume; V_{l} is the lung volume; D_{nb}, D_{b} and D_{l} are the specific densities of the soft tissue, bone and lung, respectively.

The estimated injected dose was calculated as the sum of the time-activity within the whole-body. Since the FOV of microPET is smaller than that of the microCT, some parts of the animal were not imaged by the microPET. The average voxel time-activity of the part outside the microPET image was assumed to be equal to the average voxel time-activity of the part inside the microPET image. Thus, the injected dose was calculated by (3-2).

$$ID_{\mathrm{e}} = (A_{\mathrm{in}} + A_{\mathrm{out}}) \times CF = \left(\frac{A_{\mathrm{in}}}{V_{\mathrm{wb\_in}}} \times V_{\mathrm{wb}}\right) \times CF \tag{3-2}$$

where ID_{e} denotes the estimated inject dose, A_{in} is the total time-activity of the body within microPET image, and A_{out} is the time-activity of the part outside the microPET image (but inside the corresponding microCT image). $V_{\mathrm{wb\_in}}$ is the body volume in microPET image. V_{wb} is the whole-body volume in microCT image, and CF is the calibration factor that converts radioactivity unit from *PET units* to *MBq/ml*.

In the static microPET image, the bladder had a high time-activity, which was different from the surrounding tissues, so the max gradient searching method was applied to derive the bladder mask automatically. This method consisted of four steps.

Step 1: Define the bottom region of the microPET image which contained bladder;

Step 2: Calculate the gradient at each voxel within the predefined bottom region using the equation in (3-3).

$$G(x,y,z) = \sqrt{\left(\frac{\partial C(x,y,z)}{\partial x}\right)^2 + \left(\frac{\partial C(x,y,z)}{\partial y}\right)^2 + \left(\frac{\partial C(x,y,z)}{\partial z}\right)^2} \tag{3-3}$$

where $C(x,y,z)$ is the value of tracer time-activity at the voxel (x,y,z).

Step 3: Any voxel with gradient greater than 90% of the maximal gradient within the bottom region would be marked as the bladder boundary. All voxels within the bottom region with image values above the minimal value of bladder boundary voxels were used to form the bladder mask image.

Step 4: Apply the “morphological opening” and “morphological fill” operations to the bladder mask image to remove residual artifacts.

The total bladder volume was calculated by multiplying the voxel number of the bladder mask by the microPET voxel volume ($0.4\times0.4\times0.796$ mm^3). The total time- activity of the bladder was calculated as the sum of the time-activities of voxels within the bladder mask multiplied with the microPET voxel volume.

3.2.2 Image-Derived SUV and Modified SUV

A. Image-Derived SUV (iSUV)

Similar with the formula of SUV in (2-13), iSUV can be calculated by (3-4), where the body weight and injected dose were estimated from microPET/CT images by the automatic imaged-based method described in **3.2.1**.

$$iSUV = \frac{C_{\mathrm{i}}}{ID_{\mathrm{e}}/BW_{\mathrm{e}}} \tag{3-4}$$

where ID_{e} and BW_{e} are the estimated injected dose and body weight obtained by the automatic imaged-based method. The term in the denominator is referred to as the iSUV factor; C_{i} is the tracer time-activity within the target ROI.

B. Modified SUV (mSUV)

Because the amount of the extracted tracer by renal function varied among subjects, the variability of SUV can be influenced by the tracer excretion. In order to reduce the variability of SUV, mSUV was calculated based on the target

concentration normalized by the total uptake of the whole-body excluding the amount excreted into the bladder. If the average body density was assumed to be 1 g/cm^3, the body volume could be used instead of body weight in the calculation. Thus, mSUV can be calculated by (3-5). The term in the denominator of (3-5) will be referred to as the mSUV factor.

$$mSUV = \frac{C_{\mathrm{i}}}{(A_{\mathrm{wb}} - A_{\mathrm{bl}})/(V_{\mathrm{wb}} - V_{\mathrm{bl}})} \tag{3-5}$$

where C_{i} is the tracer time-activity within the target ROI (in *PET units*); A_{wb} and A_{bl} are the total time-activity in the whole-body and the bladder; V_{wb} and V_{bl} are the volumes of the whole-body and the bladder, respectively.

3.3 Experiments

3.3.1 Small-Animal Studies

All animal experiments were conducted in compliance with the Animal Care and Use Program established by the Chancellor's Animal Research Committee of UCLA. Thirty-one SCID mice (20-33g) were implanted with U251 tumor in the left flank at least one week before the investigation with tumor volumes reaching 100 mm^3. All the mice were fasted overnight (about 15 hours) before microPET and microCT studies. For each mouse, the body weight was measured using a standard lab weighting scale. The injected dose was measured by a dosimeter and corrected for the residue of dose remained in the syringe. At 60 minutes post intraperitoneal injection of FDG (4.81-5.92 MBq), a 10 minutes static PET imaging was performed on a microPET Focus 220 tomography (Siemens Preclinical Solutions, Knoxville, TN), whose imaging field of view (FOV) is 51.2 mm diameter in transverse by 75.6

mm in axial. The spatial resolution at the center of FOV was 1.7 mm full width at half maximum (FWHM). The microPET images were reconstructed using 2D filtered back-projection with a voxel size of 0.4×0.4×0.796 mm^3 in a 128×128×95 matrix. The PET image was corrected for scatter radiation, random coincidence, dead time and physical decay. After static PET imaging, a 7-10 minutes microCT scan was acquired on a MicroCAT II tomography (Siemens Preclinical Solutions, Knoxville, TN), which has an imaging field of 51.2 mm in diameter in transverse by 99.2 mm in the axial direction. The microCT image had a voxel size of 0.2×0.2×0.2 mm^3 in 256×256×496 matrix. These mice were anesthetized (~2% isoflurane) and placed in an imaging chamber with a heating bed during the scans [119]. The imaging chamber was compatible with the microPET and microCT systems [120, 121]. The microCT image was aligned to the mircoPET image using a predetermined, geometric transformation matrix [122]. The aligned microCT image was used in PET image reconstruction for attenuation correction [123].

In the image analysis, AMIDE software [124] was used to manually remove the imaging chamber and nose cone in the microCT image. In every mouse study, ellipsoidal ROIs were drawn for major organs (brain, heart, lung, liver, kidney and muscle) in microPET images with the guide of aligned microCT images. To reduce the effects of ROI delineation, the ellipsoidal ROIs for the same major organ were of the same size and were placed in the core part of the organ for all mouse studies. The tumor volume for each mouse was large enough for manually delineating the ellipsoidal ROI on the left flank where the implanted tumor was. The size of the tumor ROI depended on the shape of the lesions in the microPET/CT images. The ROI of the bladder was also manually delineated with the visual guide from microCT and microPET images by an experienced operator for each mouse study.

The volumes of the manually drawn bladder ROIs were used as the standard for validation of the bladder volumes derived from the automatic image-based method.

3.3.2 Estimation of iSUV and mSUV

The average and maximum tracer time-activity of the delineated ROIs were calculated for calculating iSUV and mSUV. When using average tracer time-activity to calculate the iSUV and mSUV, the improved SUVs were noted as $iSUV_{mean}$ and $mSUV_{mean}$. Otherwise, the improved SUVs estimated by the maximum tracer time-activity were recorded as $iSUV_{max}$ and $mSUV_{max}$. Similarly, the SUV can also be estimated used the average and maximum tracer time-activity and noted as SUV_{mean} and SUV_{max} respectively. The predicted iSUV and mSUV were validated by the corresponding SUV.

3.3.3 Statistical Analysis

A. iSUV Validation

The estimated body weight and injected dose were compared with the actual measurements of body weight and injected dose. The percent errors of the estimated body weight and injected dose compared with the actual measurements were calculated. The iSUV factor, which is defined as the ratio between the estimated body weight and injected dose, was compared with the SUV factor calculated by the actual measurements. To evaluate iSUV, the percent errors of the 1/(iSUV factor) to 1/(SUV factor) were calculated for the comparison. In addition, the linear regression between iSUV factor and SUV factor were performed to evaluate their correspondence. The significant difference between the iSUV factor and SUV factor

was evaluated by paired t-test. A p-value <0.05 was considered statistically significant.

Moreover, $iSUV_{mean}$ was validated by SUV_{mean}, and $iSUV_{max}$ was validated by SUV_{max}. The average and standard deviation (SD) of these two sets of SUV and iSUV were compared, and linear regressions were performed both for $iSUV_{mean}$ vs. SUV_{mean} and $iSUV_{max}$ vs SUV_{max} for all target ROIs (major organs and tumor). Paired t-test was also performed to detect the significant difference between the iSUV and SUV for each target ROI.

B. mSUV Evaluation

$mSUV_{mean}$ was compared with $iSUV_{mean}$ and SUV_{mean}, while $mSUV_{max}$ was compared with $iSUV_{max}$ and SUV_{max}. The average and SD of the two sets of mSUV, iSUV and SUV were calculated for all target ROIs. The coefficient of variation (CV) was used as a measure to evaluate the inter-subject variability. The tumor-to-background separations for these two sets of mSUV, iSUV and SUV were quantified by the Mahalanobis distance that is defined in mathematical classification theory as in (3-6).

$$D = \frac{|mean_{\mathrm{t}} - mean_{\mathrm{b}}|}{\sqrt{SD_{\mathrm{t}}^2 + SD_{\mathrm{b}}^2}} \tag{3-6}$$

where D is Mahalanobis distance; $mean_{\mathrm{t}}$ is the population average value of SUV/iSUV/mSUV for tumor while $mean_{\mathrm{b}}$ is that for background; SD_{t} is the standard deviation of SUV/iSUV/mSUV for tumor while SD_{b} is that for background.

3.4 Results

3.4.1 iSUV vs. SUV

In the statistical analysis, average percent errors of the estimated body weight and injected dose to their actual measurements were -9.5±7.3% and -8.5±11.5%. The comparisons are shown in Figure 3-2 by box-and-whisker diagrams. Considering the reciprocal of iSUV factor, its average percent error to the reciprocal of SUV factor was about -0.7±14.3%. Figure 3-3 shows the linear regression for 31 pairs of iSUV factor and SUV factor. The corresponding regression equation was $y=0.83x+0.037$ with $R^2=0.44$. Paired t-test did not show significant difference between SUV factor and iSUV factor.

The $iSUV_{mean}$ and $iSUV_{max}$ for each major organ were validated by their corresponding SUV_{mean} and SUV_{max}. Figure 3-4 shows the comparisons using box-and-whisker diagrams. The average and standard deviation of SUV_{mean} and $iSUV_{mean}$ for each defined major organ and tumor are listed in Table 3-1, and those for SUV_{max}, and $iSUV_{max}$ are listed in Table 3-2. The average of iSUV was quite close with that of SUV for all major organs, while the values of their SD were also similar. Meanwhile, Figure 3-5 (a) shows the linear regression between SUV_{mean} and $iSUV_{mean}$ of all the major organs for all mouse studies. The linear regression line was $y=0.99x+0.018$ with $R^2=0.95$. Similarly, Figure 3-5 (b) shows the plot of SUV_{max} vs. $iSUV_{max}$. The linear regression line was $y=0.99x+0.027$ with $R^2=0.95$.

For each major organ, the paired t-test did not detect any significant difference between SUV_{mean} and $iSUV_{mean}$. The same results were found between SUV_{max} and $iSUV_{max}$. This indicated that the automatic image-based method is able provide the

method to estimate SUV when the measurements of body weight and inject dose were not available.

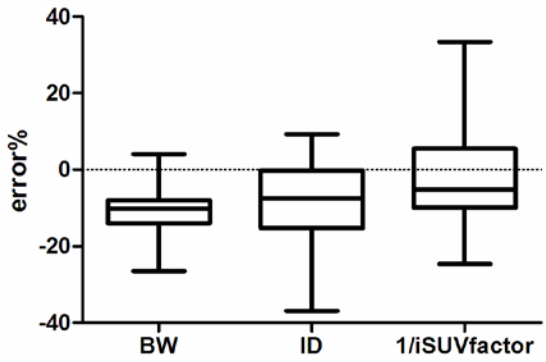

Figure 3-2 Box-and whisker diagrams of estimated error percentage of body weight (BW), injected dose (ID) and 1/iSUVfactor. Box height shows inter-quartile range. The line in the box is for the median. Whiskers indicate the largest observation (minimum to maximum).

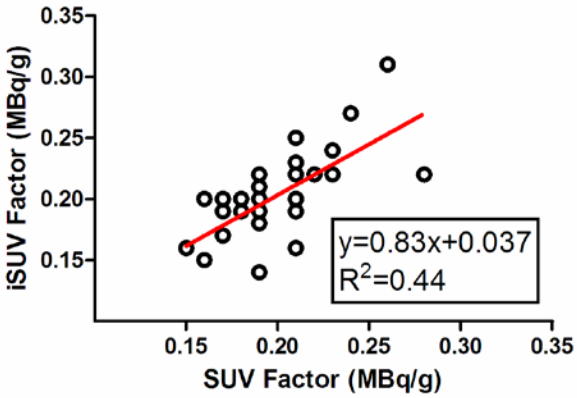

Figure 3-3 The linear regression performed for all 31 pairs of SUV factor and iSUV factor. The open circle symbols note the scatter plot of the 31 pairs of iSUV factor and SUV factor. The red solid line is the regression line.

Table 3-1 The comparison of SUV_{mean}, $iSUV_{mean}$ and $mSUV_{mean}$ by average, standard deviation and coefficient of variance.

N=31	SUV_{mean}			$iSUV_{mean}$			$mSUV_{mean}$		
	Avg.	**SD**	**CV**	**Avg.**	**SD**	**CV**	**Avg.**	**SD**	**CV**
brain	4.14	1.00	24%	4.14	1.09	26%	5.14	1.11	22%
heart	0.71	0.26	37%	0.70	0.24	35%	0.88	0.32	36%
lung	0.41	0.06	15%	0.40	0.06	14%	0.50	0.05	10%
liver	0.51	0.08	16%	0.50	0.08	15%	0.63	0.09	15%
kidney	1.76	0.42	24%	1.77	0.51	29%	2.21	0.58	26%
muscle	0.29	0.08	27%	0.29	0.09	31%	0.36	0.10	27%
tumor	2.05	0.55	27%	2.06	0.63	30%	2.55	0.65	25%

* For each ROI, the lowest CV% among SUV, iSUV, and mSUV is shaded.

Table 3-2 The comparison of SUV_{max}, $iSUV_{max}$ and $mSUV_{max}$ by average, standard deviation and coefficient of variance.

N=31	SUV_{max}			$iSUV_{max}$			$mSUV_{max}$		
	Avg.	**SD**	**CV**	**Avg.**	**SD**	**CV**	**Avg.**	**SD**	**CV**
brain	5.67	1.31	23%	5.67	1.44	25%	6.90	1.41	20%
heart	1.10	0.42	39%	1.08	0.38	36%	1.32	0.48	36%
lung	0.58	0.09	15%	0.58	0.08	14%	0.71	0.08	11%
liver	0.67	0.13	19%	0.67	0.14	21%	0.82	0.15	18%
kidney	2.35	0.62	27%	2.37	0.73	31%	2.90	0.83	29%
muscle	0.70	0.18	26%	0.70	0.18	25%	0.85	0.21	24%
tumor	2.48	0.64	26%	2.48	0.68	27%	3.02	0.70	23%

* For each ROI, the lowest CV% among SUV, iSUV, and mSUV is shaded.

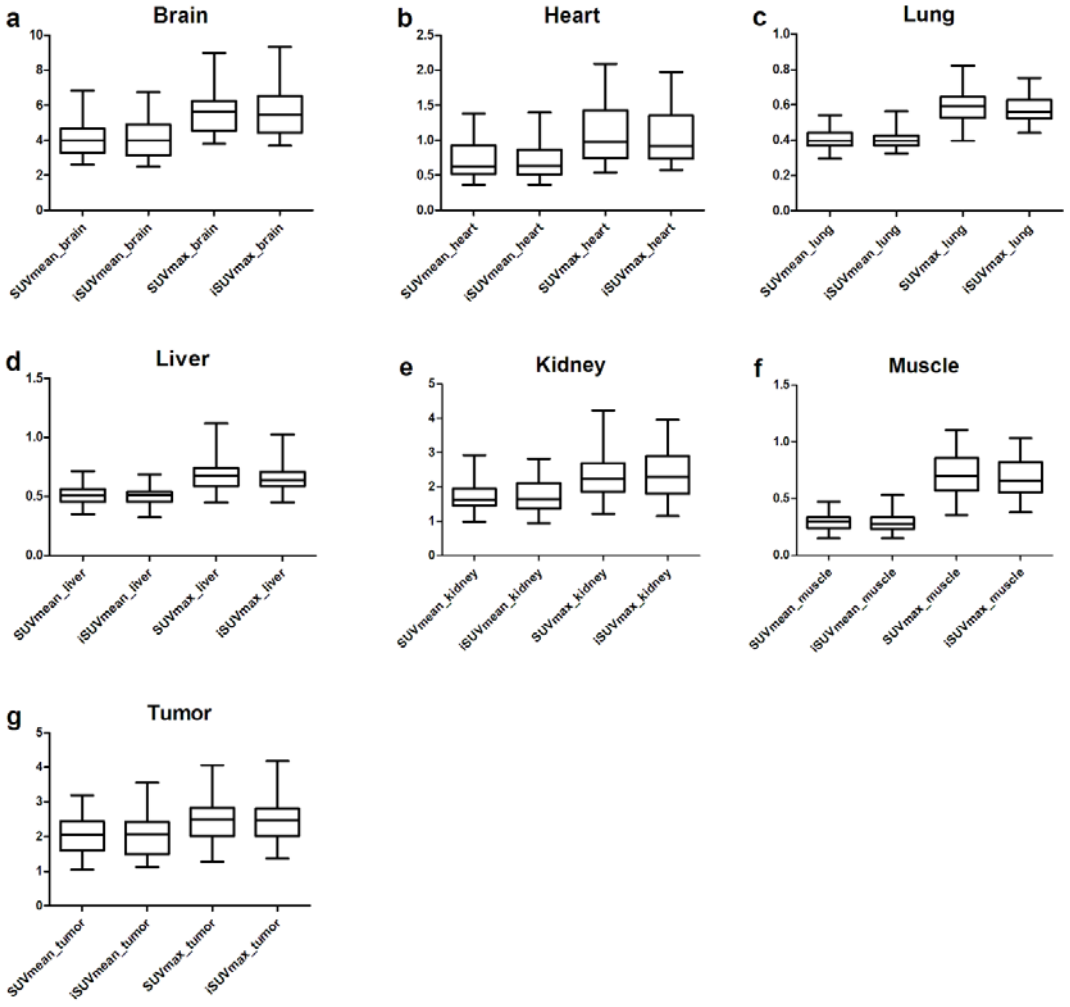

Figure 3-4 The comparisons between two sets of SUV and iSUV, SUV_{mean} vs. $iSUV_{mean}$ and SUV_{max} vs. $iSUV_{max}$, for (a) brain, (b) heart, (c) lung, (d) liver, (e) kidney, (f) muscle, and (g) tumor shown by box-and-whisker diagram. In each sub-figure, box height shows inter-quartile range. The line in the box is for the median. Whiskers indicate the largest observation (minimum to maximum).

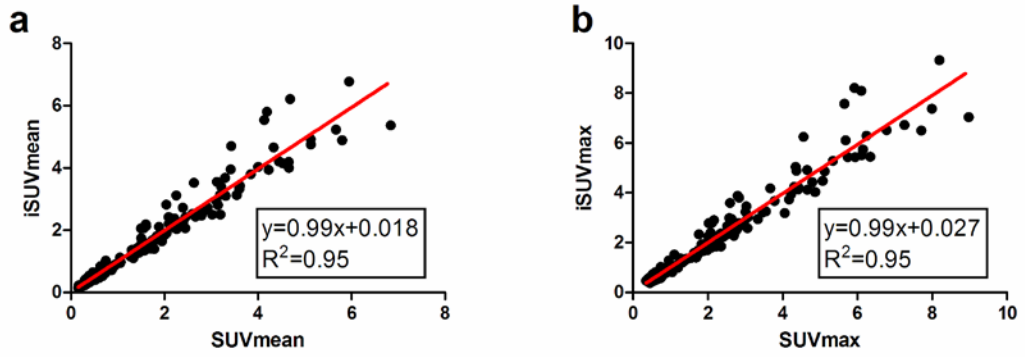

Figure 3-5 The linear regression plots between SUV and iSUV. (a) Linear regression is performed for 217 (7×31, 7 major organs for 31 mice studies) pairs of $iSUV_{mean}$ and SUV_{mean}. (b) Linear regression is performed for 217 (7×31, 7 major organs for 31 mice studies) pairs of $iSUV_{max}$ and SUV_{max}. The black dot symbols note the scatter plot of pairs of iSUV and SUV. The red solid line is the regression line.

3.4.2 mSUV vs. SUV

The bladder volumes estimated from the automatic image-based method were compared with that obtained from manual definitions. Figure 3-6 shows the linear regression between the two estimates of bladder volumes. The linear regression line was expressed as y=1.10x-4.25. The regression slope was close to 1 with R^2=0.97.

The averages, SDs and CVs for SUV_{mean}, $iSUV_{mean}$ and $mSUV_{mean}$ in each defined ROI of major organ are shown in Table 3-1. Those metrics for SUV_{max}, $iSUV_{max}$ and $mSUV_{max}$ are given in Table 3-2. From the results, the CV of $mSUV_{mean}$ decreased by about 1-5% in the brain, heart, lung and liver compared to those of SUV_{mean}, while the CV of $mSUV_{max}$ decreased by about 1-4% in the comparison with SUV_{max}. For the tumor ROI, the CV of $mSUV_{mean}$ was 2% lower than that of SUV_{mean} and the CV of $mSUV_{max}$ was 3% lower than that of SUV_{max}. Compared with $iSUV_{mean}$, the CV of $mSUV_{mean}$ was decreased by about 1-5% for

the selected major organs and tumor, except in the heart the CV of $mSUV_{mean}$ was increased by about 1%. Similar results were observed in the comparisons between $mSUV_{max}$ and $iSUV_{max}$.

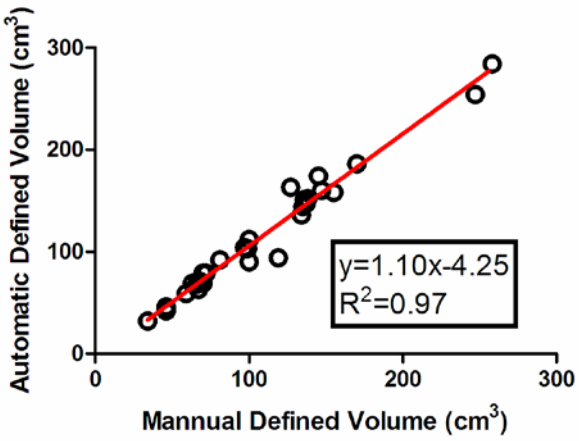

Figure 3-6 The validation of bladder volume. The estimated bladder volume obtained by the automatic image-based method is compared to the value obtained by manual method with visual support from microCT image. The open circle symbols denote the scatter plot of the pairs of automatic and manual results. The red solid line denotes the linear regression line.

Tumor-to-background separation was increased by using mSUV because of the decrease in the variances of the mSUV values in the tumor and background regions. In this study, lung, liver and muscle were chosen as the background. The Mahalanobis distance was used to quantify the tumor-to-background separation. From the values of Mahalanobis distance listed in Table 3-3, among SUV_{mean}, $iSUV_{mean}$, and $mSUV_{mean}$ the highest values were obtained for $mSUV_{mean}$ regardless of the background used, which was about 5% and 20% higher than those of SUV_{mean} and $iSUV_{mean}$. Figure 3-7(a) shows the tumor-to-background separation distribution of SUV_{mean}, $iSUV_{mean}$ and $mSUV_{mean}$. The result indicated that $mSUV_{mean}$ had the largest separation between the tumor and the background. Similar results were obtained when comparing the tumor-to-background separations among SUV_{max},

$iSUV_{max}$ and $mSUV_{max}$ (shown in Table 3-3). It is clear that $mSUV_{max}$ had the largest separation which is about 8% and 17% higher in Mahalanobis distance than SUV_{max} and $iSUV_{max}$. Figure 3-7(b) shows the tumor-to-background separation distribution of SUV_{max}, $iSUV_{max}$ and $mSUV_{max}$. In this figure, a threshold of 1 (gray dash line) is given as an example to separate tumor form background. From the example, it was found that using SUV_{max} and $iSUV_{max}$ could both yield some false positives, while $mSUV_{max}$ could separate tumor from background without error.

The automatic image-based method was run in Matlab 7.0. It took ~38 seconds to do all the calculations for one animal using a Mac with OS X 10.5.5 (2.4GHz Intel Core 2 Duo, 4GB SDRAM).

Table 3-3 Comparison of Mahalanobis distance to evaluate SUV, iSUV and mSUV for tumor-to-background separation.

	Mahalanobis distance*		
	tumor to lung	**tumor to liver**	**tumor to muscle**
SUV_{mean}	2.99	2.80	3.18
$iSUV_{mean}$	2.61	2.44	2.77
$mSUV_{mean}$	3.15	2.94	3.34
SUV_{max}	2.95	2.78	2.69
$iSUV_{max}$	2.77	2.60	2.53
$mSUV_{max}$	3.27	3.06	2.96

* The higher value of Mahalanobis distance means more separation between tumor and background. The highest values for each background reference are shaded.

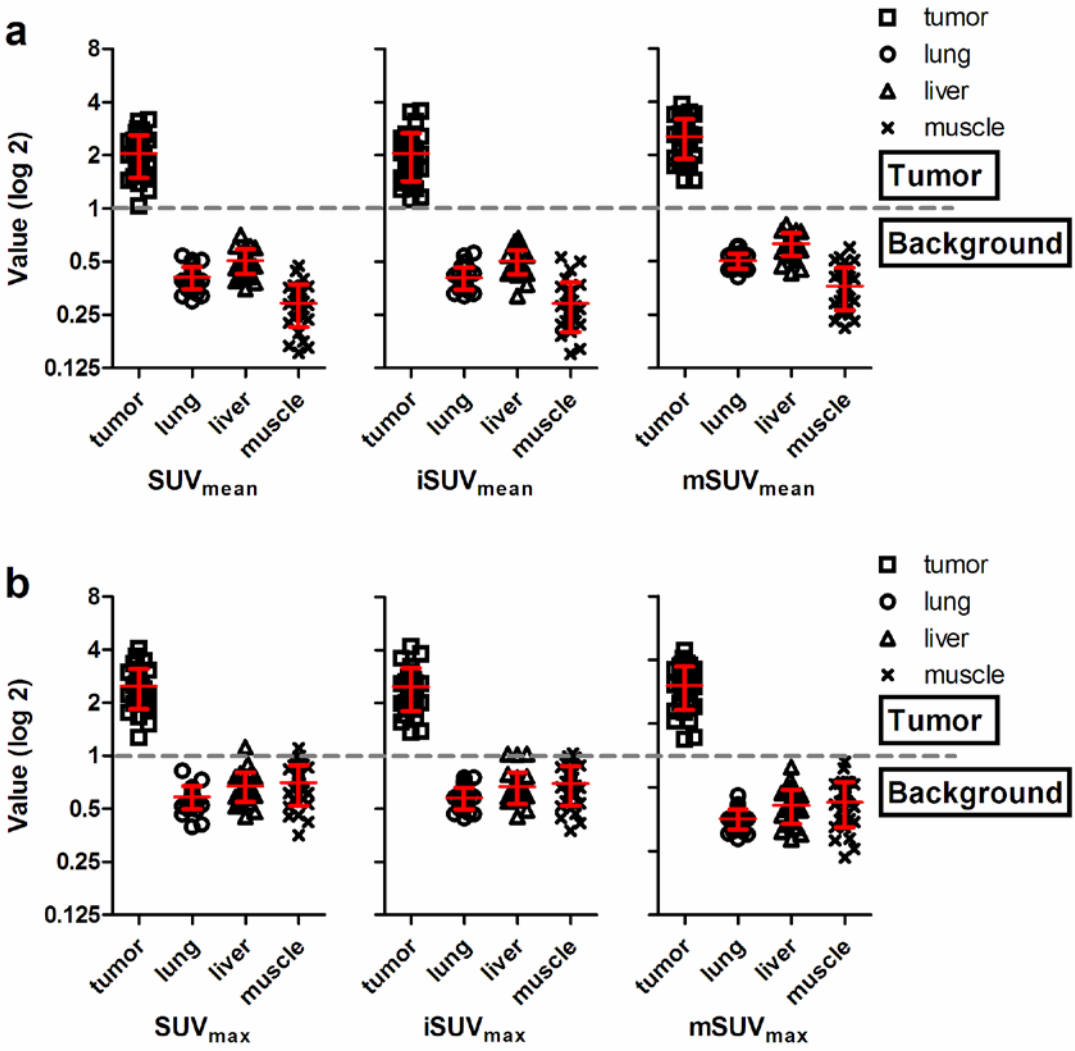

Figure 3-7 Plot of tumor and background (lung, liver and muscle) SUVs, iSUVs and mSUVs. The values for tumor (square), lung (circle), liver (triangle) and muscle (cross) are grouped for SUV, iSUV and mSUV to compare the tumor-to-background separations (quantitative measurements of the separation are listed in Table 3-3). (a) This figure shows that the tumor-to-background separation is increased using $mSUV_{mean}$ compared with using SUV_{mean} and $iSUV_{mean}$. A threshold of 1 (gray dash line) is given as an example to separate tumor from background in this figure. (b) This figure shows that the tumor-to-background separation is increased using $mSUV_{max}$ compared with using SUV_{max} and $iSUV_{max}$. A threshold of 1 (gray dash line) is given as an example to separate tumor from background in this figure.

3.5 Discussion

This study developed a robust and automatic image-based method for calculating iSUV which can be used as a substitute of the regular SUV in mouse FDG-PET studies, when the body weight or injected dose is not available or unreliable. Based on this image-based method, a modification of SUV was applied to reduce the inter-subject variability with regards of the tracer excretion variability among subjects. The microPET/CT images used in the image-based method were obtained in separate scanners. In this condition, a hardware registration method was applied to minimize the error in the alignment of two modalities images [122]. Moreover, the scans were performed when the implanted tumors had relatively large volumes (>100 mm3). This also allowed the reliable PET-to-CT alignment for the tumor lesions.

The results from the present mouse studies indicated that the average percent error of estimated body weight was about -9.5% and that of estimated injected dose was about -8.5%. The worst case percentage errors of the estimated body weight and injected dose were -22.5% and -35.1%, respectively. The underestimations of the body weight and the injected dose, however, occurred together, thus resulted in much less error in the ratio (e.g., the iSUV factor).

There are several error sources that might have affected the accuracy of the estimations using the image-based method in this study. First is the incomplete coverage of the whole body in the microCT and the microPET images, as shown in Figure 3-8 (a) and (b) respectively. In this case, part of the tail and the hind legs were missing because of the limited FOV in microCT. The missing parts are manually sketched out in Figure 3-8(c). In addition, the tracer time-activity outside

the FOV of the microPET would introduce out-of-field scatter and affected the quantitative accuracy of the image values [125]. The accuracy of the injected dose estimate also relied on that of the PET data correction, including the normalization, attenuation correction, scatters correction, random correction, dead-time corrections and the calibration. Urine leakage from the bladder during the microPET scan can also impact the injected dose estimation. Another source of error is in the assumed values of specific density for various tissues. The densities used in the body weight estimation were assumed uniform in each type of tissue, which were grouped into soft tissue, bone and lung. The lung has only a small impact on the body weight estimation, and its density could be assumed to be zero without much effect to the estimated body weight.

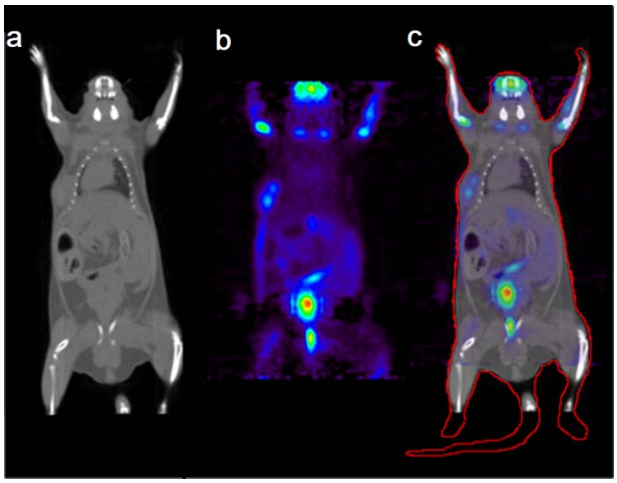

Figure 3-8 The microCT and microPET images and the missing body parts in the images. (a) the microCT image has a field of view of 51.2mm×51.2mm×99.2mm. The microCT image voxel size is 0.2mm×0.2mm×0.2mm in a 256×256×496 matrix. (b) The microPET image has a field of view of 51.2mm×51.2mm×75.6mm. The microPET image voxel size is 0.4mm×0.4mm×0.796mm in a 128×128×95 matrix. (c) The fused mircoPET/CT image. In this figure, the contour of the whole body, included the missing parts of the mouse body, is sketched out by red solid line.

It is expected that the major improvement in the accuracy of estimation is to position more consistently the mouse in the imaging chamber during the scans, and to fit the entire body in the FOV. This may reduce the influence from the missing regions in the estimation of body weight and injected dose by the image-based method. Newer microPET scanners (e.g., Inveon Dedicated PET System) have larger FOVs, and studies using these scanners are expected to have less variability due to this problem of not covering the entire animal within the FOV. Also, the conversion of the attenuation coefficient from microCT images to that of microPET for attenuation correction could also be improved to give a better estimate of the injected dose.

However, the correlated underestimations of body weight and injected dose didn't introduce a large estimation error to the iSUV factor, of which the percent error was about -0.7% in average compared with SUV factor. Including all 217 pairs of iSUV and SUV (7 major organs for 31 mice studies) in linear regression, the results in Figure 3-5(a) and (b) indicated that iSUV closely match the SUV (R^2=0.95), either for $iSUV_{mean}$ vs. SUV_{mean} or $iSUV_{max}$ vs. SUV_{max}. These data demonstrated the validity of the iSUV from the automatic image-based method in this study.

In future work, the body surface area could be obtained directly from the microCT image (e.g., by a marching cubes algorithm [126]), and it could be used as the normalization factor instead of body weight. To use of body surface area has been reported in some studies to be preferable in SUV calculation [31], e.g. for obese subjects with increased fraction of body fat.

On the other hand, mSUV was proposed to improve SUV reliability for accurate diagnosis of tumor malignancy by removing the tracer excretion variability among subjects. To a certain extent, mSUV could be considered as the SUV with FDG excretion correction. Bladder voiding performed immediately before a FDG-PET scan as part of the animal preparation procedure can achieve the same objective, and can be considered to be equivalent to replacing the image processing procedures for calculating the accumulated bladder radioactivity. However, the renal pelvis beside bladder usually also contained urine. This could influence the mSUV in the kidney ROI. As a result, CV of mSUV in kidney was found to be 2% higher than that of SUV both for $mSUV_{mean}$ vs. SUV_{mean} and $mSUV_{max}$ vs. SUV_{max}. It is assumed in this study that the amount of FDG in renal pelvis is much less than that in bladder, and mSUV mainly considered the influence of the FDG excreted into bladder. The influence from the renal pelvis could be expected to remove in the calculation of mSUV by defining kidney ROIs to exclude the renal pelvis in future.

In common practical application, a predefined threshold of SUV is usually set for determining malignancy. That is, the lesion would be regarded as malignant when its SUV is higher than the predefined threshold. Therefore, to enlarge the separation between the tumor and background is expected to be helpful for defining a threshold in the malignancy detection and improving the accuracy of classification. The mSUV is shown to increase the separation between the tumor and background in Figure 3-7. Especially, $mSUV_{max}$ showed its advantage in eliminating the false positive compared with SUV_{max} and $iSUV_{max}$. The Mahalanobis distance was adopted to measure the separation and the results indicated that the tumor to the background (liver, lung or muscle) separation all increased by using mSUV compared with using SUV.

The amount of reduction in CV of tumor mSUV shown in this study is not very large, since all the animals studied were quite uniform in size, in their preparations, and in the study procedure. When the physiological condition of the animals is more variable and the study condition is less uniform, the amount of improvement in mSUV is expected to be increased. Also, other body tissues that have large population variability in FDG extraction could also be excluded, just like the bladder that are addressed in this study. That is, the tracer time-activities in these tissues and the corresponding volume/weight could be taken out of the injected dose and the body weight, respectively, in the calculation of mSUV. The reliability of the predicted mSUV is expected to be further improved, though further work is needed to demonstrate the amount of improvement in practical situations.

The present study is focused on mouse FDG-PET study to improve the reliability of SUV. The underlying concept of mSUV can be extended to whole-body human FDG-PET studies. It is impractical for iSUV in clinical studies, because the partial body imaging is usually performed for clinical routines. However, the methodology to obtain iSUV can be transformed to quantify the partial body tracer uptake value instead of the SUV for whole-body. Although the effectiveness of the approach for improving SUV reliability in the human studies needs more investigations, results from the present study clearly indicated its feasibility and potentials.

3.6 Summary

In this chapter, an automatic image-based method was developed to derive the improved SUVs for static mouse FDG-PET imaging. Firstly, iSUV is feasibly

calculated based on the information of microCT and microPET images for mouse studies. It is demonstrated that iSUV could be used as a semi-quantitative index to substitute for SUV when directly measured body weight and/or injected dose are missing or unreliable. Secondly, the mSUV is shown to reduce the inter-subject variability of SUV and increase the tumor-to-background separation. Therefore, with further investigations mSUV has the potential to be useful for increasing the accuracy to separate malignancy from benign lesions in FDG PET studies.

Chapter 4

Generalized Optimal Quantitative Index for Dual-Time PET Imaging

4.1 Introduction

FDG-PET imaging has been widely used in clinical environment for cancer diagnosis because “hot” spot of lesions can be easily visualized on FDG-PET images due to higher glucose metabolism in tumors than that in normal tissues. In addition to visual evaluation, SUV is a popular semi-quantitative index for cancer diagnosis using static PET imaging, although it has a number of limitations. For example, the lesion with SUV>2.5 in the lung is usually regarded as malignancy. Nevertheless, benign lesion and inflammation tissue may also demonstrate similar evaluated uptake of FDG for general static FDG-PET imaging. This gives rise to false positive in the diagnosis of cancer, resulting in inaccurate cancer staging and inappropriate choice of therapies [127, 128]. Dynamic imaging has shown its efficiency in providing distinct physiological parameter in differentiating malignancy from benign or inflammation lesions. However, it is impractical for the clinical routine due to the substantially longer imaging time required and lower

patient throughput. Hence, dual-time imaging protocol with one early scan and one delayed scan has been proposed to address this dilemma by using the change of SUVs to classify lesions [39]. Usually, the change of SUVs is referred as retention index (RI). Recently some reports have been published for doubting dual-time FDG-PET imaging about its usefulness or necessary in the differentiation of malignancy from benign lesions [115, 129]. In these published studies, the empirical dual-time imaging protocols and RI, which relied on the experience of operators, were adopted for the differentiation, which might be the reason for the low accuracy in cancer diagnosis.

A simulation framework has been proposed to evaluate dual time protocols, where RI was used to optimize dual-time imaging protocol resulting a rigid optimal dual-time protocol [44]. Recently, a generalized quantitative index (QI) was proposed to add an exponential weight into the traditional RI for increasing diagnostic accuracy of malignancy detection [45]. However, the optimization for the weight of QI was based on a fixed dual-time imaging protocol. The suitable threshold for differentiating malignancy from benign lesions and the noise effects have not been discussed yet in this pioneer study.

This chapter aims to develop a framework for simultaneously optimizing the weight of QI and the dual-time imaging protocol of FDG-PET in lung cancer diagnosis. Meanwhile, the performance of the optimal QI and the corresponding imaging protocol are investigated and compared with the traditional RI approach at various noise levels by computer simulations.

4.2 Methods

4.2.1 Optimization of Quantitative Index

As mentioned in **2.4**, SUV can be calculated using (2-13) for a lesion in static PET image. For dual-time imaging, SUV_{E} and SUV_{D} were respectively obtained at the early and delayed scans, and then the percent change between the SUVs was often referred as to RI. In some cases, $SUV_{\mathrm{D}}/SUV_{\mathrm{E}}$ can be also referred as to RI, which was used in this study. Generally a predefined threshold of RI was adopted to classify malignancy in dual-time FDG-PET imaging. That is, the lesion was regarded as malignancy when its RI was higher than the given threshold.

QI was proposed based on RI with an exponential weight, n, which added to the dominator of RI, as shown in (4-1) [45]. In this case, RI is a special case of QI when $n = 1$.

$$QI = \frac{SUV_{\mathrm{D}}}{SUV_{\mathrm{E}}^{n}} \tag{4-1}$$

The process of separating the malignancy from benign lesions could be regarded as a two-class classification problem using QI as the feature. Suppose the lesions which might be malignant or benign were examined by a given dual-time imaging protocol, the optimal weight n in (4-1) was derived according to the Fisher discriminant given in (4-2).

$$f = \frac{det(S_{\mathrm{b}})}{det(S_{\mathrm{w}})} \tag{4-2}$$

where S_{b} and S_{w} are the between-class and within-class scatter matrixes of two classes, det denotes the operation of matrix determinant.

The prior probabilities of malignant and benign lesions were both assumed as 50%. Thus, between-class scatter matrix was calculated by (4-3) while within-class scatter matrix was expressed as (4-4).

$$S_{\mathrm{b}} = \sum_{i=1,2} \frac{1}{2} [(\overline{QI}_i - \overline{QI})(\overline{QI}_i - \overline{QI})^T] \tag{4-3}$$

where, $\overline{QI}$ is the average of all samples in malignant and benign classes, $\overline{QI}_i$ is the average of samples in either class of benign and malignancy.

$$S_w = \sum_{i=1,2} \frac{1}{2} E\left[\left(QI_j - \overline{QI}_i\right)\left(QI_j - \overline{QI}_i\right)^T \middle| QI_j \in C_i\right] \tag{4-4}$$

where, QI_j is the j$^{\mathrm{th}}$ sample in the i$^{\mathrm{th}}$ class; E denotes expectation operation; C_i is the class of benign or malignancy.

When the mid-scan time points of early and delayed scans were varied within given ranges, the optimal n for each dual-time imaging protocol can be searched by maximizing the Fisher discriminant. The maximum values of the cost function for each dual-time imaging protocol were then transformed into point intensity, followed by plotting a two-dimensional map with early imaging time as x axial and delayed imaging time as y axial. This map was named as cost map. Similarly, the values of optimal n corresponding to the maximum values of the cost function are plotted in a two-dimensional map, which was named as optimal n map.

According to the optimal n map, if the value of optimal weight n was keeping unchanged along with varying imaging protocols, it indicated that the appropriate value of optimal n was insensitive with imaging protocol. Thus, the generalized optimal QI can be obtained by this optimal n. Meanwhile the corresponding flexible optimal dual-time imaging protocol can also be fixed on.

4.2.2 Computer Simulations

The general FDG model introduced in **2.2.1** was used to simulate TTACs of malignant and benign lesions based on its corresponding differential equations in (2-1). The rate constants of the general FDG model for malignant and benign lesions used in the computer simulation are listed in Table 4-1, which were obtained from [44]. The PTAC was defined by the Feng's input function model given in (4-5) with the parameters derived from population studies [130].

$$C_{\mathrm{p}}(t) = \begin{cases} [A_1(\mathrm{t}-\tau) - A_2 - A_3]e^{\lambda_1(t-\tau)} + A_2 e^{\lambda_2(t-\tau)} + A_3 e^{\lambda_3(t-\tau)}, \mathrm{t} > \tau \\ 0, \mathrm{t} \le \tau \end{cases} \quad (4\text{-}5)$$

where A_1= 851.123$\mu Ci/mL/min$, A_2=21.880$\mu Ci/mL$, A_3= 20.811$\mu Ci/mL$, λ_1= -4.134$/min$, λ_2= -0.119$/min$, λ_3= -0.0104$/min$ and τ =0 min.

Table 4-1 Rate constants of malignant and benign lesions in lung

Lesions	K_1 ($mL/min/mL$)	k_2 ($/min$)	k_3 ($/min$)	k_4 ($/min$)
Stage III non-small-cell lung cancer (M1)	0.084	0.021	0.072	0
Lung carcinoma (M2)	0.139	0.296	0.164	0
Lung aspergillosis infection (B1)	0.199	0.978	0.240	0.010
Lung coccidiomycosis infection (B2)	0.181	0.869	0.039	0.0007

Gaussian noise was then added to the simulated TTACs as the measurement error with the consideration of the influences from decay time, scan duration, noise level and uptake activities [44, 131]. The variance can be described by (4-6).

$$\sigma^2 = \frac{c \times e^{\lambda t} \times C_t(t)}{\Delta t} \quad (4\text{-}6)$$

where, c is proportional to noise level; $\lambda = \ln(2)/T_{half}$, T_{half} is the half life time of isotope Fluorine-18 (^{18}F), and Δt is the imaging duration.

The time-activities at the early and delayed scans (C_{E} and C_{D}) were obtained from the simulated TTACs. SUV_{E} and SUV_{D} were calculated by multiplying C_{E} and C_{D} with the mean scale factor of 0.1795 [44]. It was supposed that the range of early imaging time (t_{E}) should be varied from 30 to 100 minute post tracer injections, and the delayed imaging time (t_{D}) should be changed from 40 to 160 min with the constraint of $t_{\mathrm{E}} < t_{\mathrm{D}}$, while the duration of each scan was simply set as 5 min. For each type of lesions given in Table 4-1, 1000 sets of SUVs were simulated under the noise level of 0.5 ($c = 0.5$). In total, there were 4000 pairs of SUV as training samples to figure out the generalized optimal QI and its corresponding flexible optimal dual-time imaging protocol.

4.2.3 Performance Evaluation

To evaluate the performance, the approach using the generalized optimal *QI* and the corresponding flexible dual-time imaging protocol (QI_flexible) was compared with the other two previous approaches: one used the RI with the flexible dual-time imaging protocol (RI_flexible), and the other one adopted the RI with fixed dual-time imaging protocol (RI_fixed). Here, the flexible dual-time imaging protocol is obtained in **4.2.1**. The fixed dual-time imaging protocol is derived from our previous investigation [44], whose early and delayed scans are performed at 45 min and 120 min post tracer injection.

Under the noise level of 0.5, 1000 pairs of SUVs were then regenerated for each approach according to fixed or flexible imaging protocol. The optimal classification thresholds were searched for all the simulated samples in order to achieve the maximum accuracy of the classification. Meanwhile, the effect of noise was also investigated for these three approaches. Five noise levels (c = 0.5, 1.0, 2.0,

3.0 and 4.0) were used in the computer simulations to generate 4000 pairs of SUVs (1000 for each lesion) per noise level.

4.3 Results

4.3.1 Generalized Optimal Quantitative Index

Figure 4-1 plots the cost map of maximum cost function and optimal *n* map. For the simplicity, top 50% maximum values of cost function are illuminated with colors while the others are marked by white in Figure 4-1a.

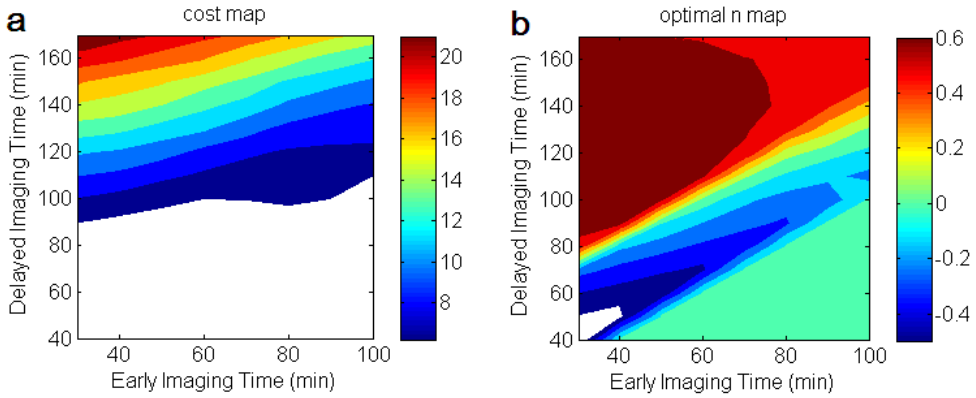

Figure 4-1 (a) the obtained cost map and (b) the optimal n map.

As the definition of cost map, the higher value of intensity meant higher result from cost function with better performance of separation between two classes for the investigated dual-time imaging protocols. By taking two maps into account, a plateau (optimal n =0.6) was observed in the optimal *n* map (Figure 4-1(b)) while the corresponding values of this region in cost map (Figure 4-1(a)) were still relatively high (top 50%). This implied that this optimal n could achieve relatively stable classification in the region of $30 < t_{\mathrm{E}} < 70$ and $90 < t_{\mathrm{D}} < 140$. So the generalized optimal *QI* were suggested setting as (4-7).

$$QI_{op} = \frac{SUV_D}{SUV_E^{0.6}} \tag{4-7}$$

Thus, the corresponding flexible dual-time imaging protocol was suggested as that t_E can vary from 30*min* to 70*min* and t_D can change in the range of from 90*min* to 140*min*. The interval between two scans was advised as no more than 70*min*.

4.3.2 Threshold and Accuracy

The distributions of the criteria's values for three approaches (RI_flexible, RI_fixed and QI_flexible) are respectively plotted in Figure 4-2. From the figures, it was obvious that QI_flexible achieved the largest separation between malignant and benign classes.

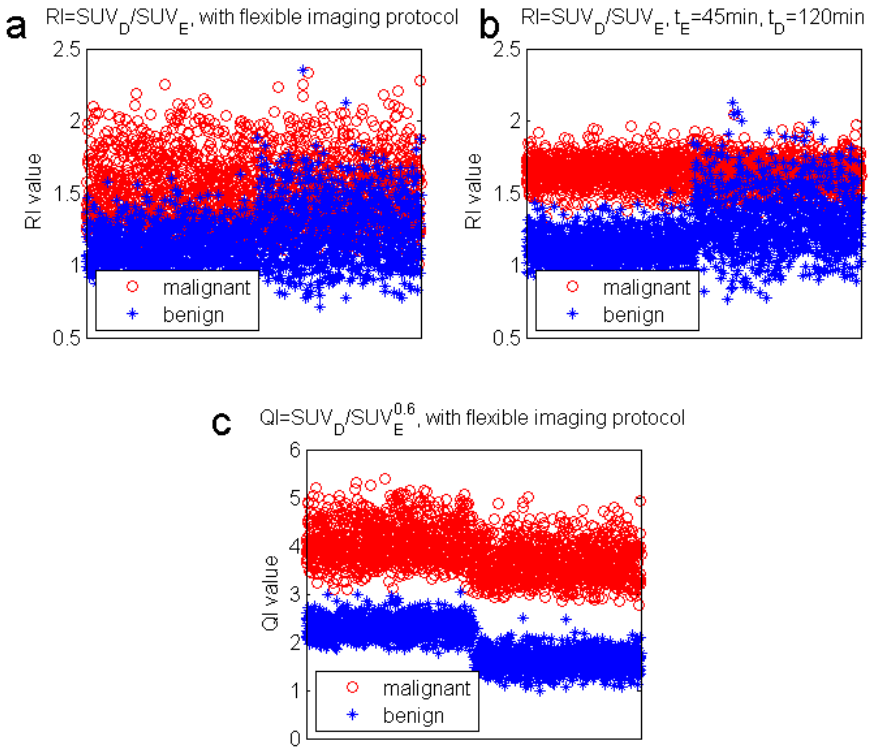

Figure 4-2 The distributions of quantitative measures of three different approaches: (a) RI_flexible, (b) RI_fixed, and (c) QI_flexible. In each subfigure, the red circle denotes the malignant class and blue star denotes the benign class.

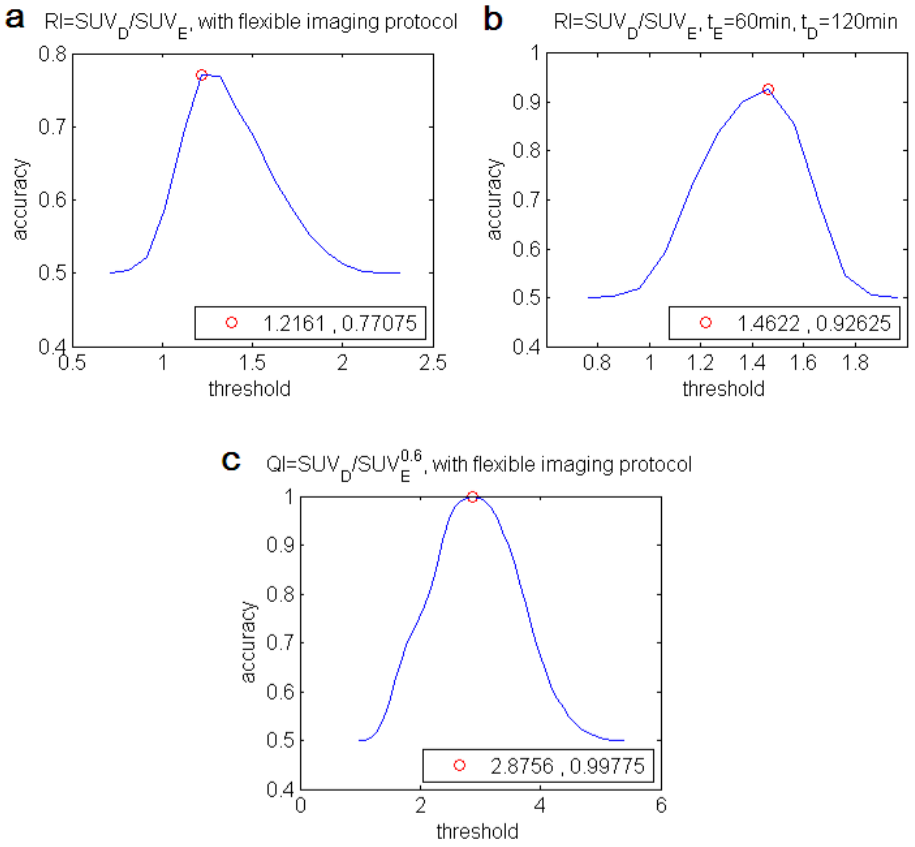

Figure 4-3 Plots of classification accuracies for three approaches. (a) RI_flexible; (b) RI_fixed; (c) QI_flexible. The best threshold with greatest accuracy for each approach is illuminated by red circle. The values of the optimum thresholds and greatest accuracies are given in the legends.

4.3.3 Effect of Noise

Three approaches (RI_flexible, RI_fixed, and QI_flexible) with their optimum thresholds obtained in **4.3.2** were also investigated for their performances in separating malignancy from benign lesions under five noise levels (0.5, 1.0, 2.0, 3.0, and 4.0). And the accuracies for three approaches under five noise levels are listed in Table 4-2. From this table, the results demonstrated the application of generalized optimal QI with flexible imaging protocol achieved substantially high accuracy, which seemed to be less sensitive to the noise levels. On the contrary, the other two

approaches suffered from the noisy condition with decreasing accuracy when noise tended to be higher.

Table 4-2 Accuracy of classification at different noise levels

Noise Level	Accuracy of Classification		
	RI _flexible	RI _fixed (t_E=45, t_D=120)	QI_flexible
0.5	0.771	0.926	0.998
1.0	0.756	0.847	0.992
2.0	0.727	0.785	0.973
3.0	0.700	0.736	0.951
4.0	0.676	0.721	0.935

4.4 Discussion

Due to the limited availability of kinetics for lung lesions including inflammation, only four sets of kinetics were obtained from literature review. This is the reason why the classification accuracy was so “perfect” for the approach QI_flexible. In addition, the approach QI_flexible was evaluated by a set of published data of dual-time FDG-PET in lung [40]. As a result, the generalized optimal QI increased the highest accuracy of differentiation to 89%, comparing with that of RI about 84%. Despite the small improvement in this application, it still demonstrated that the application of generalized optimal QI is helpful to improve the performance of dual-time FDG-PET in differentiating malignancy from benign lesions with a flexible imaging protocol that was suitable in high-throughput clinical environments.

In the future, further data analysis including full Monte Carlo simulations and validation on clinical data would be warranted to derive more convincing protocol including differentiating criterion for clinical dual-time FDG PET imaging.

4.5 Summary

In this chapter, a simulation framework has been developed for search better solution for dual-time FDG-PET imaging in the diagnosis of lung cancer using generalized optimal quantitative index (QI). The results demonstrated that generalized optimal QI ($QI_{op} = \frac{SUV_D}{SUV_E^{0.6}}$) with the threshold of 2.9 provided the highest accuracy in differentiating malignancy from benign lesions for lung cancer under varied noise levels. The corresponding optimal range of dual-time imaging protocol was suggested that early and delayed scans commenced at 30~70 minutes and 90~140 minutes post tracer injection, and the interval was no more than 70 minutes.

Chapter 5

Non-Invasive Patlak Quantification Method for Dynamic Small-Animal PET Imaging

5.1 Introduction

As is known to us, PTAC is usually required as input function in the quantitative analysis for dynamic PET images regardless of using tracer kinetic modeling with WNLS method or graphic analysis (GA) method. However, the invasive arterial blood sampling to obtain PTAC is relatively inconvenient and harmful. It also tends to be much challenging for preclinical studies with small-animal. In this condition, great efforts have been made to develop non-invasive methods for the reduction or elimination of the invasive blood samples, which have been reviewed in **1.3**.

Given multiple regions of interest (ROIs) with distinct TTACs, complex biological systems can be modeled as a single-input-multi-output (SIMO) system [46, 47]. In this case, the kinetic parameters and the input function can be estimated

simultaneously [46]. Non-invasive GA methods have also been proposed to avoid the problems associated with invasive approaches. For example, if a reference region that reflects the non-specific binding in a neuroreceptor study is available, the Logan graphic analysis method can be transformed to a non-invasive Logan method (introduced in **2.5.2**) in which the slope of the linear plot represents the ratio of the distribution volume between the target and the reference regions [93]. It is possible that the non-invasive estimation of the influx rate in FDG-PET studies may also benefit from the use of reference tissues.

A non-invasive PGA (nPGA) method that used a reference region to derive the relative influx rate for FDG-PET studies was recently proposed and evaluated using simulated TTACs of the human brain [132]. This chapter aims to extend nPGA to provide a non-invasive quantification approach in small-animal studies. The performance of the nPGA method was systematically compared with that of the traditional PGA method by using computer simulations and mouse FDG-PET studies. The results of the WNLS method were also used in the evaluation of the estimated biases of nPGA.

5.2 Theory of Non-Invasive Patlak Graphic Analysis

The non-invasive PGA (nPGA) method was proposed for the derivation of a relative influx rate using a reference region in the quantification of MRGlc for human brain FDG-PET studies [132]. It can be assumed that the input functions for different ROIs are the same PTAC. The PGA equations for two distinct ROIs (one being the reference, the other being the target) are described by (5-1).

$$\begin{cases} C_{\mathrm{ref}}(t) = K_{\mathrm{ref}} \int_0^t C_{\mathrm{p}}(\tau)d\tau + I_{\mathrm{ref}}\, C_{\mathrm{p}}(t) \\ C_{\mathrm{tg}}(t) = K_{\mathrm{tg}} \int_0^t C_{\mathrm{p}}(\tau)d\tau + I_{\mathrm{tg}}\, C_{\mathrm{p}}(t) \end{cases}, t > t^* \tag{5-1}$$

where $C_{\mathrm{ref}}(t)$ and $C_{\mathrm{tg}}(t)$ are TTACs of the reference and target ROIs.

Combining the equations for the two ROIs in (5-1) into (5-2) eliminates the contribution of the PTAC and derives the relative influx rate, i.e. the ratio of influx rates between the target and reference regions. The relative influx rate can also be referred to as the target to reference relative influx rate. See the Appendix C for more details on the derivation of (5-2).

$$\begin{aligned} \int_{t_0}^t C_{\mathrm{tg}}(\tau)d\tau = K_{\mathrm{tr}} \int_{t_0}^t C_{\mathrm{ref}}(\tau)d\tau + I_{\mathrm{tr}}[C_{\mathrm{ref}}(t) - C_{\mathrm{ref}}(t_0)] \\ - I_{\mathrm{rr}}\big[C_{\mathrm{tg}}(t) - C_{\mathrm{tg}}(t_0)\big], t > t_0 > t^* \end{aligned} \tag{5-2}$$

where, t_0 is the first imaging frame whose mid-scan time is later than t^*; and K_{tr} is the target to reference relative influx rate.

For the mid-scan time of the TTAC, where $t_0, t_1, t_2, \cdots, t_n > t^*$, (5-2) can be expressed in matrix form as given by (5-3).

$$y = X\theta_{\mathrm{r}} + \varepsilon \tag{5-3}$$

where ε denotes the equation error term; For the mid-scan time $t > t^*$, $y = \begin{bmatrix} \int_{t_0}^{t_1} C_{\mathrm{tg}}(\tau)d\tau & \int_{t_0}^{t_2} C_{\mathrm{tg}}(\tau)d\tau & \cdots & \int_{t_0}^{t_{\mathrm{N}}} C_{\mathrm{tg}}(\tau)d\tau \end{bmatrix}^{\mathrm{T}}$, $X = \begin{bmatrix} \int_{t_0}^{t_1} C_{\mathrm{ref}}(\tau)d\tau & C_{\mathrm{ref}}(t_1) - C_{\mathrm{ref}}(t_0) & -C_{\mathrm{tg}}(t_1) + C_{\mathrm{tg}}(t_0) \\ \int_{t_0}^{t_2} C_{\mathrm{ref}}(\tau)d\tau & C_{\mathrm{ref}}(t_2) - C_{\mathrm{ref}}(t_0) & -C_{\mathrm{tg}}(t_2) + C_{\mathrm{tg}}(t_0) \\ \vdots & \vdots & \vdots \\ \int_{t_0}^{t_{\mathrm{N}}} C_{\mathrm{ref}}(\tau)d\tau & C_{\mathrm{ref}}(t_{\mathrm{N}}) - C_{\mathrm{ref}}(t_0) & -C_{\mathrm{tg}}(t_n) + C_{\mathrm{tg}}(t_0) \end{bmatrix}$, $\theta_r = \begin{bmatrix} K_{\mathrm{tr}} \\ I_{\mathrm{tr}} \\ I_{\mathrm{rr}} \end{bmatrix}$, $\varepsilon = \begin{bmatrix} \varepsilon_1 \\ \varepsilon_2 \\ \vdots \\ \varepsilon_{\mathrm{N}} \end{bmatrix}$.

The target to reference relative influx rate, noted as $\hat{\theta}_{\mathrm{r}}$, can be solved using the linear least squares method as given by (5-4).

$$\hat{\theta}_{\mathrm{r}} = (\mathrm{X}^{\mathrm{T}}\mathrm{X})^{-1}\mathrm{X}^{\mathrm{T}}\mathrm{y} \tag{5-4}$$

5.3 Experiments

5.3.1 Small-Animal Studies

All small-animal experiments were conducted in compliance with the Animal Care and Use Program established by the Chancellor's Animal Research Committee of UCLA. Fifteen C57BL/6 mice (~27g, non-fasting) were anesthetized with ~2% isoflurane and administered with FDG (~13 MBq, tail vein bolus). Five of these mice had been implanted with MCak tumors in both shoulders about one week prior to the FDG-PET studies. After FDG was administered, a 60-minute dynamic imaging study was performed for each mouse on a Focus 220 microPET scanner (Siemens Medical Solutions USA, Inc.). Sixteen blood samples were manually taken from a femoral catheter during the scan. Seven of these FDG-PET studies were conducted with a 31-frame imaging protocol: 15×0.5s, 1×2s, 1×4s, 1×6s, 1×15s, 3×30s, 1×60s, 1×120s, 3×80s, and 4×900s frames. The other eight FDG-PET studies were conducted with a 26-frame imaging protocol: 1×1.2s, 10×0.4s, 1×1.7s, 2×5s, 1×17.5s, 1×45s, 1×60s, 1×90s, 1×150s, 1×180s, 1×220s, 1×365s, and 4×550s frames. After PET imaging, a 10-minute CT scan was acquired for each mouse on a MicroCAT II. The CT image was then aligned to the PET images. The PET images were reconstructed using 2D filtered back-projection with CT-based attenuation correction. Each frame was reconstructed with an image resolution of 128×128×95

voxels with a voxel size of 0.4×0.4×0.796 mm^3. Equation (5-5) was used to derive the PTACs, as a means to obtain the plasma activity from the blood samples [90].

$$\begin{cases} C_{\mathrm{p}}(t) = C_{\mathrm{b}}(t) \times R_{\mathrm{FDG}}(t) \\ R_{\mathrm{FDG}}(t) = 0.386e^{-0.191t} + 1.165 \end{cases} \tag{5-5}$$

where t is the blood sampling time in minutes after FDG injection; $C_{\mathrm{p}}(t)$ is the PTAC, $C_{\mathrm{b}}(t)$ is the FDG TAC of whole-blood samples; and $R_{\mathrm{FDG}}(t)$ is a function for the ratio of plasma to whole blood.

Using the AMIDE software [124], ellipsoidal ROIs were manually delineated on the reconstructed microPET images for the major organs, with the aligned CT images acting as a guide. For the whole-body PET imaging with small-animal, the ROIs can be delineated by covering whole organs, due to the comparably small volumes of the animals. The tumor ROI was also defined for the five tumour-bearing mice. The brain, lungs, liver, muscle and tumor ROIs were numbered from 1 to 5, respectively. The TTAC was derived by averaging the values of all the voxels within the ROI.

5.3.2 Computer Simulations

The PTAC, $C_{\mathrm{p}}(t)$, was simulated based on a mathematical model with 4 exponential components, as given by (5-6).

$$C_{\mathrm{p}}(t) = A_1 e^{\lambda_1 t} + A_2 e^{\lambda_2 t} + A_3 e^{\lambda_3 t} - (A_1 + A_2 + A_3) e^{\lambda_4 t} \tag{5-6}$$

where A_1 =63.01 *MBq/mL*, A_2 =4.95 *MBq/mL*, A_3 =1.105 *MBq/mL*, λ_1 =9.27/*min*, λ_2=0.178/*min*, λ_3=0.0157/*min*, and λ_4=41/*min*. These parameters were assigned by the mean values given by Ferl *et al* [133]. An 18-point blood sampling protocol was used with time points at 0.07, 0.11, 0.14, 0.17, 0.21, 0.24, 0.27, 0.31, 0.59, 0.9, 1.5, 4.5, 9.5, 15.5, 24.5, 34.5, 45.5 and 58.5 minutes post-injection.

A 26-frame 60-minute imaging protocol was used in the simulation with 1×1.2s, 10×0.4s, 1×1.7s, 2×5s, 1×17.5s, 1×45s, 1×60s, 1×90s, 1×150s, 1×180s, 1×220s, 1×365s, and 4×550s frames. The TTAC was then simulated based on the general FDG model described by (2-4) (introduced in **2.2.1**). A Gaussian noise $\varepsilon(t)$ was then added to obtain the measurement of the TTAC, as given by (5-7).

$$\begin{aligned}\bar{C}_{\mathrm{t}}(t) &= C_{\mathrm{t}}(t) + \varepsilon(t) \\ &= \frac{K_1}{\alpha_2 - \alpha_1}\left[(k_3 + k_4 - \alpha_1)e^{-\alpha_1 t}\right. \\ &\quad \left. + (\alpha_2 - k_3 - k_4)e^{-\alpha_2 t}\right] \otimes C_{\mathrm{p}}(t) + V_{\mathrm{b}}C_{\mathrm{p}}(t) + \varepsilon(t)\end{aligned} \tag{5-7}$$

where, $\bar{C}_{\mathrm{t}}(t)$ is the measurement of the TTAC; and the macro parameters, α_1 and α_2, are the combination of the rate constants as given in (2-3), which can be obtained using the average rate constants of certain organ derived from fifteen FDG-PET mouse studies listed in Table 5-1. $\varepsilon(t)$ is the PET measurement noise, which is assumed to be an additive, independent Gaussian noise with zero mean and variance as specified by (4-6).

The square root of c can range from 0.25 to 8 [131]. In this investigation, the values of c were set to as 0.1, 0.5, 1, 2 and 4, corresponding to noise levels ranging from 0.7% to 3% at the last measurement of TTAC. 100 TTACs were simulated for each noise level. One noise free TTAC with was also simulated. As such, five noise levels were used in the computer simulation.

5.3.3 Performance Evaluation

The target to reference relative influx rate in both the small animal studies and the computer simulations can be defined as the ratio of the influx rate between the target and reference ROIs, calculated as (5-8).

$$K_{tr} = \frac{K_{\mathrm{tg}}}{K_{\mathrm{ref}}} \tag{5-8}$$

where, *t* is the index number of the target ROI, and *r* is the index number of reference ROI. The target index number *t* can be set to 1, 2, 3, 4 or 5 for the brain, lungs, liver, muscle or tumor, respectively. For the reference ROI, the maximum index number is 4. The tumor ROI is not used as a reference ROI in this investigation.

In small-animal studies, the WNLS method (introduced in **2.3.1**) was applied to derive estimates for the rate constants of the general FDG model using the kinetic imaging system (KIS) [81]. The weights in WNLS method were chosen to be proportional to the ratio between the imaging duration and the measurement in each frame [26]. Influx rates for each ROI were calculated according to $K_i = \frac{K_1 k_2}{k_2 + k_3}$, and the relative influx rate was then derived based on (5-8). This relative influx rate was referred to as $K_{\mathrm{tr,WNLS}}$.

In the computer simulations, the mean rate constant for each ROI in the small-animal studies were used to derive the true value of the relative influx rate. For a given pair of target and reference ROIs, the true value of the relative influx rate was also obtained by (5-8), and was referred to as $K_{\mathrm{tr,true}}$.

The PGA and nPGA methods, respectively introduced in **2.3.3** and **5.2**, were both used to calculate the relative influx rates for the computer simulations and the small-animal studies. For the PGA method, TTACs in the range of 3-22 minutes were used to estimate the influx rate for each ROI in order to minimize the influence of k_4 [90], allowing the derivation of the relative influx rate, $K_{\mathrm{tr,PGA}}$. For the nPGA method, the relative influx rates could be directly obtained by using the TTACs of

the reference and target ROIs (excluded the data in the first 3 minutes). The relative influx rate as calculated by nPGA was referred to as $K_{\mathrm{tr,nPGA}}$.

In the small-animal studies, for each pair of target and reference ROIs, the mean and standard deviation (SD) of $K_{\mathrm{tr,WNLS}}$, $K_{\mathrm{tr,PGA}}$ and $K_{\mathrm{tr,nPGA}}$ was calculated across the fifteen mice. Linear regression analysis was applied between $K_{\mathrm{tr,WLNS}}$ and $K_{\mathrm{tr,nPGA}}$ to evaluate the performance of the nPGA method. The linear relationship between $K_{\mathrm{tr,PGA}}$ and $K_{\mathrm{tr,nPGA}}$ was also investigated. Similarly, the mean and SD values of $K_{\mathrm{tr,PGA}}$ and $K_{\mathrm{tr,nPGA}}$ were calculated to evaluate the estimated $K_{\mathrm{tr,PGA}}$ and $K_{\mathrm{tr,nPGA}}$ in the computer simulations. The coefficient of variation (CV) was then calculated. Moreover, percent biases were calculated for the average $K_{\mathrm{tr,PGA}}$ and $K_{\mathrm{tr,nPGA}}$ compared with $K_{\mathrm{tr,true}}$ under different noise levels in order to evaluate the performances of the nPGA and PGA methods.

To further investigate the effect of the different kinetic models used in WNLS, new reference parameters were directly estimated by WNLS using different kinetic models for the comparisons. In addition to the general FDG model that is three-compartment and four-parameter FDG kinetic model with vascular volume (3c4pVb) mentioned in 2.2.1, three additional models were used: the general FDG model with k_4=0, V_b=0 (3c3p), the general FDG model with k_4=0 (3c3pVb), and the general FDG model with V_b=0 (3c4p). The percent bias of K_{tr} estimated by PGA and nPGA methods were calculated according to the true relative influx rate from these four models.

5.4 Results

5.4.1 Estimated Parameters and Simulated TTACs

The rate constants of the general FDG model were estimated for five main organs and tumor from a set of fifteen mouse FDG-PET studies. The average of the estimated rate constants for the brain, lungs, liver, muscle and tumor are listed in Table 5-1. They were used to derive the TTAC in the computer simulations for further evaluation of the nPGA method. Figure 5-1 plots the PTAC and TTACs obtained from one sample mouse study and its simulated noise-free PTAC and TTACs.

Table 5-1 The rate constants derived by WNLS in mouse FDG-PET studies

ROI #	1	2	3	4	5
Parameter	**brain**	**lung**	**liver**	**muscle**	**tumor***
K_1 **(*ml/min/g*)**	0.217	0.139	0.84	0.036	0.221
k_2 **(*/min*)**	0.413	0.644	1.432	0.324	0.263
k_3 **(*/min*)**	0.113	0.104	0.02	0.074	0.712
k_4 **(*/min*)**	0.017	0.011	0.008	0.019	0.021
V_b **(*ml/ml*)**	0.076	0.161	0.098	0.014	0.057

* The results with tumor as target are derived from the five tumor-bearing mouse studies.

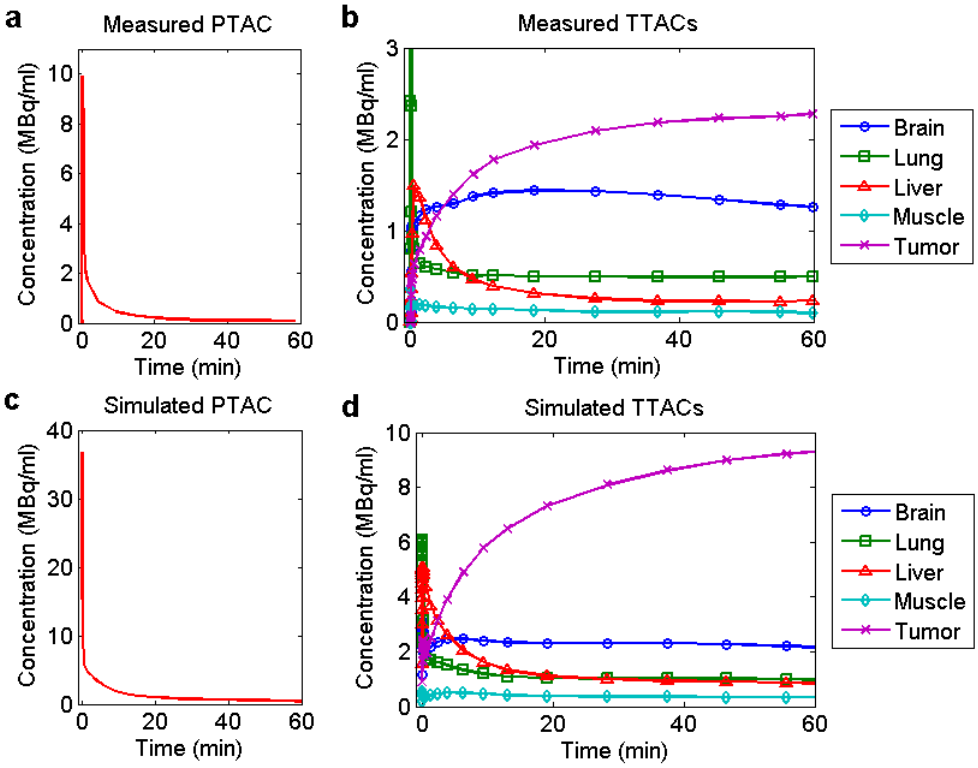

Figure 5-1 Measured and simulated PTAC and TTACs. (a) Measured PTAC of one sample mouse study; (b) Measured TTACs of one sample mouse study; (c) Simulated noise-free PTAC obtained using (5-6) ; (d) Simulated noise-free TTACs using the rates constants in Table 5-1.

5.4.2 Effect of Relative Influx Rate in Small-Animal Studies

Table 5-2 lists the relative influx rate derived by WNLS method ($K_{\mathrm{tr,WNLS}}$), PGA method ($K_{\mathrm{tr,PGA}}$) and nPGA method ($K_{\mathrm{tr,nPGA}}$). When the brain was chosen as the reference ROI, comparably similar values of relative influx rates were observed by $K_{\mathrm{tr,WNLS}}$, $K_{\mathrm{tr,nPGA}}$ and $K_{\mathrm{tr,PGA}}$ for the targets of lungs, muscles and tumors. The results for the liver were the exception. Similar results were observed when the lung ROI was used as the reference. When the muscles were chosen as the reference ROI, similar results were observed between $K_{\mathrm{tr,nPGA}}$ and $K_{\mathrm{tr,PGA}}$ for the brain, lungs and tumors, with the liver results again being an exception. However, both $K_{\mathrm{tr,nPGA}}$ and

$K_{tr,PGA}$ were underestimates of the relative influx rate when compared to $K_{tr,WNLS}$. The results were quite different when the liver was chosen as the reference ROI. Compared to $K_{tr,WNLS}$, $K_{tr,PGA}$ was an overestimate while $K_{tr,nPGA}$ was an underestimate.

Table 5-2 Relative influx rates for the studied pair of target and reference

Reference	K_{tr}	Target (mean ± SD)				
		1 brain	2 lung	3 liver	4 muscle	5 tumor*
1 brain	$K_{tr,WNLS}$		0.55±0.27	0.37±0.27	0.17±0.11	1.58±0.43
	$K_{tr,PGA}$		0.55±0.26	0.24±0.26	0.20±0.11	1.69±0.40
	$K_{tr,nPGA}$		0.62±0.24	0.57±0.29	0.19±0.09	1.76±0.44
2 lung	$K_{tr,WNLS}$	2.25±1.05		0.64±0.22	0.32±0.19	5.07±0.84
	$K_{tr,PGA}$	2.21±0.96		0.44±0.14	0.37±0.18	5.23±0.81
	$K_{tr,nPGA}$	1.85±0.83		0.86±0.26	0.31±0.10	5.14±1.06
3 liver	$K_{tr,WNLS}$	4.04±2.45	1.72±0.51		0.53±0.30	10.53±1.06
	$K_{tr,PGA}$	5.72±3.10	2.61±1.12		0.95±0.63	13.81±4.15
	$K_{tr,nPGA}$	2.35±1.53	1.24±0.39		0.35±0.14	8.68±1.88
4 muscle	$K_{tr,WNLS}$	9.89±9.44	4.25±2.61	2.6±1.60		27.13±19.26
	$K_{tr,PGA}$	7.96±6.37	3.37±1.70	1.46±0.92		23.39±11.69
	$K_{tr,nPGA}$	7.10±6.23	3.58±1.55	3.22±1.59		26.15±18.49

* The results with tumor as target are derived from the five tumor-bearing mouse studies.

Table 5-3 lists the results of the linear regression analysis for $K_{tr,nPGA}$ vs. $K_{tr,WNLS}$ and $K_{tr,nPGA}$ vs. $K_{tr,PGA}$ for the same reference groups, where *a* and *b* are the calculated slope and intercept, respectively. From the results, high linear correlations (R^2>0.9) were achieved in $K_{tr,nPGA}$vs. $K_{tr,WNLS}$ and $K_{tr,nPGA}$ vs. $K_{tr,PGA}$when the brain, lungs and muscle were used as reference. However, the results when using the liver as the reference region were not as good as expected especially in $K_{tr,nPGA}$ vs. $K_{tr,PGA}$,

where a was much lower than 1 and R^2 was less than 0.9. For the fair comparison, Table 5-4 lists the results of linear regression analysis of the estimates of $K_{\mathrm{tr,nPGA}}$ vs. $K_{\mathrm{tr,WNLS}}$ and of $K_{\mathrm{tr,nPGA}}$ vs. $K_{\mathrm{tr,PGA}}$ for the same target groups. High correlation was still observed for $K_{tr,nPGA}$ vs. $K_{\mathrm{tr,WNLS}}$ and $K_{\mathrm{tr,nPGA}}$ vs. $K_{\mathrm{tr,PGA}}$ when the brain, lungs and tumor ROIs were chosen as targets. The worst correlation was observed when the muscle ROI was used as the target. However, the results when using the tumor ROI as the target indicated that the estimated $K_{\mathrm{tr,nPGA}}$ were quite similar to $K_{\mathrm{tr,PGA}}$ and $K_{\mathrm{tr,WNLS}}$. Thus, nPGA potentially has a better capacity for malignant tumor detection.

Table 5-3 A summary of linear regression for the same reference groups.

Reference ($y=ax+b$)	$K_{\mathrm{tr,nPGA}}$ **vs.** $K_{\mathrm{tr,WNLS}}$			$K_{\mathrm{tr,nPGA}}$ **vs.** $K_{\mathrm{tr,PGA}}$		
	a	b	R^2	a	b	R^2
brain	1.01	0.102	0.953	0.944	0.151	0.923
lung	0.918	0.0702	0.971	0.891	0.146	0.964
liver	0.764	-0.197	0.959	0.525	-0.134	0.884
muscle	1.11	-0.635	0.915	1.12	-0.036	0.939

Table 5-4 A summary of linear regression for the same target groups.

Target ($y=ax+b$)	$K_{\mathrm{tr,nPGA}}$ **vs.** $K_{\mathrm{tr,WNLS}}$			$K_{\mathrm{tr,nPGA}}$ **vs.** $K_{\mathrm{tr,PGA}}$		
	a	b	R^2	a	b	R^2
brain	0.663	0.185	0.979	0.824	-0.455	0.894
lung	0.673	0.321	0.918	0.754	0.161	0.812
liver	1.05	0.257	0.941	1.76	0.264	0.874
muscle	0.480	0.114	0.708	0.174	0.194	0.317
Tumor*	0.955	-0.155	0.994	1.18	-2.58	0.945

* The results with tumor as target are derived from the five tumor-bearing mice studies.

5.4.3 Effect of Noise Levels

Table 5-5 lists the mean and SD for the estimated relative influx rates obtained in the computer simulations across different noise levels. A certain pair of target and reference ROIs is specified by the subscripts in Table 5-5. For example, K_{12} represents the relative influx rate when the brain (*t=1*) and lung (*r=2*) ROIs were adopted as the target and reference regions, respectively. It was observed that the mean $K_{\mathrm{tr,PGA}}$ and mean $K_{\mathrm{tr,nPGA}}$ both changed slightly with increasing noise levels. The percent bias of mean $K_{\mathrm{tr,PGA}}$ and $K_{\mathrm{tr,nPGA}}$ compared to $K_{\mathrm{tr,true}}$ were also calculated. The highest bias exceeded 50% when the liver and brain ROIs were chosen as the target and reference regions, respectively. The percent biases of the relative influx rates estimated by PGA and nPGA methods are plotted as a function of the noise levels in

Figure 5-2 to show the changes of the percent bias as noise levels increase. It was demonstrated that the relative influx rate was insensitive to varied noise levels despite the high biases that were observed for the cases of liver ROI versus brain or lung ROIs (K_{13}, K_{23}, K_{31} and K_{32}). However, when tumor was chosen as target, the biases of $K_{\mathrm{tr,nPGA}}$ were around 10% comparing with $K_{\mathrm{tr,true}}$ at the various noise levels and those of $K_{\mathrm{tr,PGA}}$ were no more than 20%. Figure 5-3 plots the CV of the relative influx rates as a function of the noise levels. The reliabilities of the estimated relative influx rates for both $K_{\mathrm{tr,PGA}}$ and $K_{\mathrm{tr,nPGA}}$ were degraded when noise levels increased. For example, the CV of K_{54} reached about 3.5% and CV of $K_{\mathrm{tr,PGA}}$ was about 9.4% at a noise level of 4. Similar trends of CVs were also observed for other relative influx rates by using different target and reference ROIs. The CVs of most $K_{\mathrm{tr,PGA}}$ were about as twice as those of $K_{\mathrm{tr,nPGA}}$.

Table 5-5 Estimates of the relative influx rates (K_{tr}) under different noise levels.

Ref.	Brain (Mean±SD)				Lung (Mean±SD)				Liver (Mean±SD)				Muscle (Mean±SD)			
Target	**lung**	**liver**	**muscle**	**tumor**	**brain**	**liver**	**muscle**	**tumor**	**brain**	**lung**	**muscle**	**tumor**	**brain**	**lung**	**liver**	**tumor**
K_{tr}	K_{21}	K_{31}	K_{41}	K_{51}	K_{12}	K_{32}	K_{42}	K_{52}	K_{13}	K_{23}	K_{43}	K_{53}	K_{14}	K_{24}	K_{34}	K_{54}
$K_{tr,ture}$	0.41	0.25	0.12	3.46	2.41	0.60	0.28	8.35	4.03	1.67	0.47	13.95	8.49	3.52	2.11	29.41
(a) 1 run with noise level c = 0																
$K_{tr,PGA}$	0.38	0.23	0.14	3.86	2.60	0.61	0.37	10.03	4.28	1.65	0.61	16.52	7.08	2.72	1.65	27.31
$K_{tr,nPGA}$	0.44	0.41	0.15	4.05	2.26	0.92	0.34	9.49	2.43	1.10	0.38	11.85	6.64	2.91	2.63	27.73
(b) 100 runs with noise level c = 0.1																
$K_{tr,PGA}$	0.38 ±0.0040	0.23 ±0.0044	0.14 ±0.0024	3.86 ±0.023	2.61 ±0.027	0.61 ±0.013	0.37 ±0.0068	10.05 ±0.093	4.30 ±0.082	1.65 ±0.034	0.61 ±0.015	16.56 ±0.304	7.08 ±0.123	2.72 ±0.050	1.65 ±0.041	27.31 ±0.448
$K_{tr,nPGA}$	0.44 ±0.0013	0.41 ±0.0027	0.15 ±0.0010	4.05 ±0.012	2.26 ±0.0066	0.91 ±0.0071	0.34 ±0.0018	9.49 ±0.041	2.43 ±0.016	1.10 ±0.010	0.38 ±0.002	11.84 ±0.130	6.63 ±0.050	2.90 ±0.015	2.63 ±0.012	27.65 ±0.182
(c) 100 runs with noise level c = 0.5																
$K_{tr,PGA}$	0.38 ±0.0093	0.23 ±0.010	0.14 ±0.0054	3.85 ±0.047	2.61 ±0.064	0.60 ±0.028	0.37 ±0.015	10.07 ±0.231	4.33 ±0.181	1.66 ±0.077	0.61 ±0.034	16.68 ±0.684	7.12 ±0.270	2.73 ±0.115	1.65 ±0.089	27.43 ±1.00
$K_{tr,nPGA}$	0.44 ±0.0013	0.41 ±0.0034	0.15 ±0.0023	4.05 ±0.027	2.25 ±0.013	0.91 ±0.012	0.34 ±0.004	9.47 ±0.081	2.45 ±0.020	1.10 ±0.014	0.38 ±0.004	11.71 ±0.238	6.56 ±0.108	2.89 ±0.036	2.63 ±0.026	27.69 ±0.424
(d) 100 runs with noise level c = 1.0																
$K_{tr,PGA}$	0.38 ±0.013	0.23 ±0.014	0.14 ±0.0075	3.86 ±0.070	2.60 ±0.087	0.61 ±0.039	0.37 ±0.020	10.04 ±0.34	4.27 ±0.246	1.64 ±0.104	0.60 ±0.045	16.47 ±0.901	7.12 ±0.379	2.74 ±0.145	1.67 ±0.124	27.44 ±1.34
$K_{tr,nPGA}$	0.44 ±0.0037	0.41 ±0.0040	0.15 ±0.0035	4.05 ±0.042	2.25 ±0.019	0.91 ±0.012	0.34 ±0.004	9.46 ±0.108	2.45 ±0.024	1.10 ±0.015	0.38 ±0.005	11.65 ±0.319	6.51 ±0.162	2.89 ±0.037	2.63 ±0.035	27.80 ±0.515
(e) 100 runs with noise level c = 2.0																
$K_{tr,PGA}$	0.38 ±0.018	0.23 ±0.018	0.14 ±0.0099	3.87 ±0.102	2.62 ±0.124	0.61 ±0.054	0.37 ±0.028	10.12 ±0.413	4.31 ±0.349	1.65 ±0.149	0.61 ±0.060	16.67 ±1.34	7.13 ±0.513	2.73 ±0.213	1.66 ±0.162	27.56 ±2.01
$K_{tr,nPGA}$	0.44 ±0.0053	0.41 ±0.0055	0.16 ±0.0051	4.05 ±0.058	2.25 ±0.027	0.91 ±0.015	0.35 ±0.0070	9.42 ±0.157	2.46 ±0.034	1.09 ±0.019	0.38 ±0.007	11.43 ±0.419	6.41 ±0.217	2.86 ±0.058	2.63 ±0.049	27.65 ±0.658
(f) 100 runs with noise level c = 4.0																
$K_{tr,PGA}$	0.39 ±0.025	0.23 ±0.029	0.14 ±0.014	3.88 ±0.137	2.60 ±0.165	0.60 ±0.080	0.37 ±0.045	10.06 ±0.648	4.41 ±0.589	1.70 ±0.241	0.62 ±0.092	17.07 ±2.17	7.13 ±0.680	2.76 ±0.328	1.64 ±0.233	27.60 ±2.59
$K_{tr,nPGA}$	0.44 ±0.0072	0.41 ±0.0085	0.16 ±0.0067	4.05 ±0.067	2.25 ±0.036	0.92 ±0.021	0.35 ±0.010	9.41 ±0.277	2.46 ±0.053	1.09 ±0.025	0.38 ±0.012	11.26 ±0.531	6.33 ±0.277	2.85 ±0.076	2.63 ±0.080	27.84 ±0.978

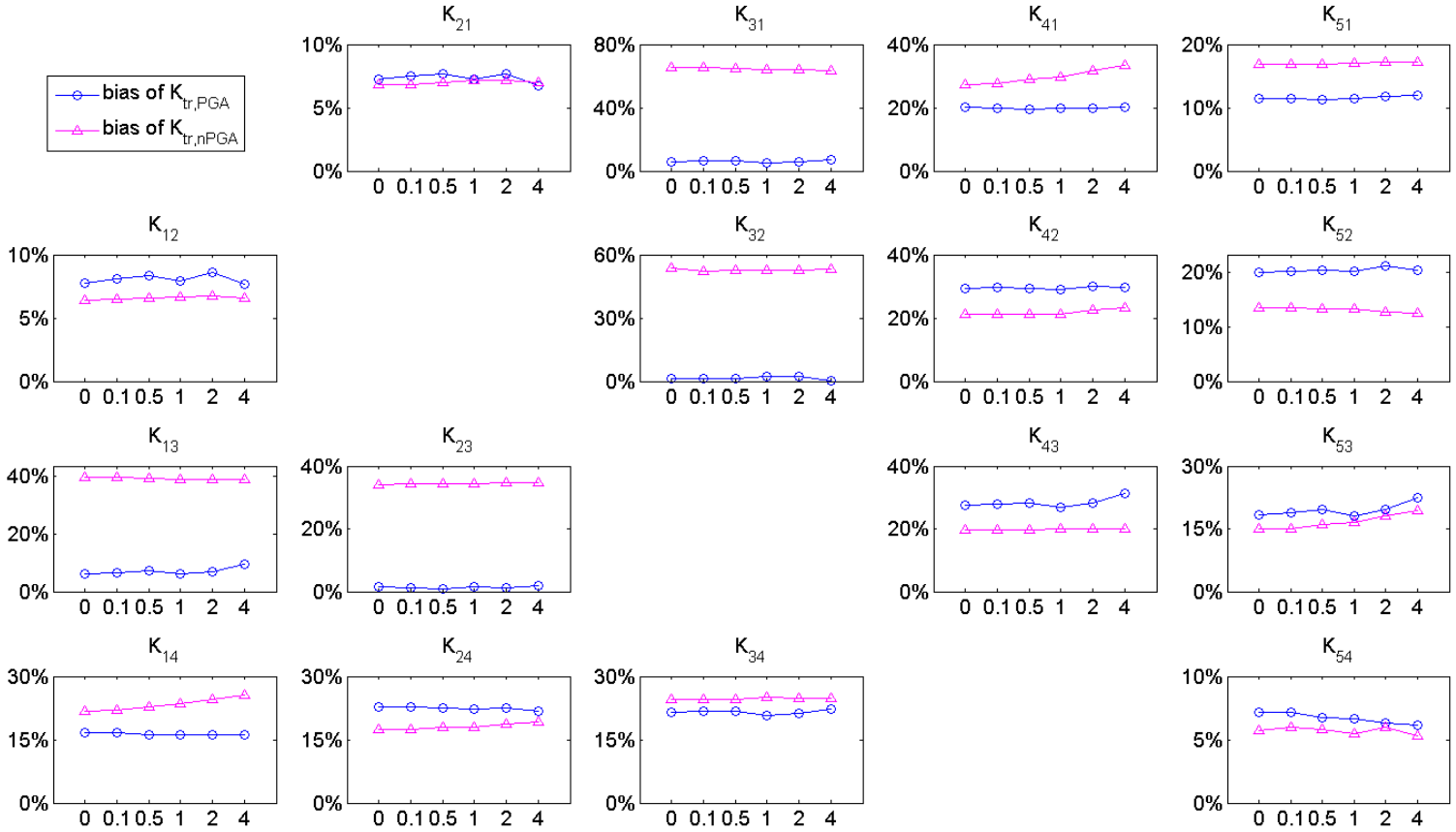

Figure 5-2 Plot of percentage bias of relative influx rates estimated by PGA and nPGA methods at different noise levels. In all the sub-figures, the vertical axis denotes the bias in percentage, and the horizontal axis notes the noise level c, which could be set to 0, 0.1, 0.5, 1, 2 and 4. The blue open circle markers indicate the bias values of $K_{\mathrm{tr,PGA}}$ under different noise levels, while the magenta open triangle markers are for those of $K_{\mathrm{tr,nPGA}}$. The solid lines reflect the change tendencies of bias with the rise of noise level.

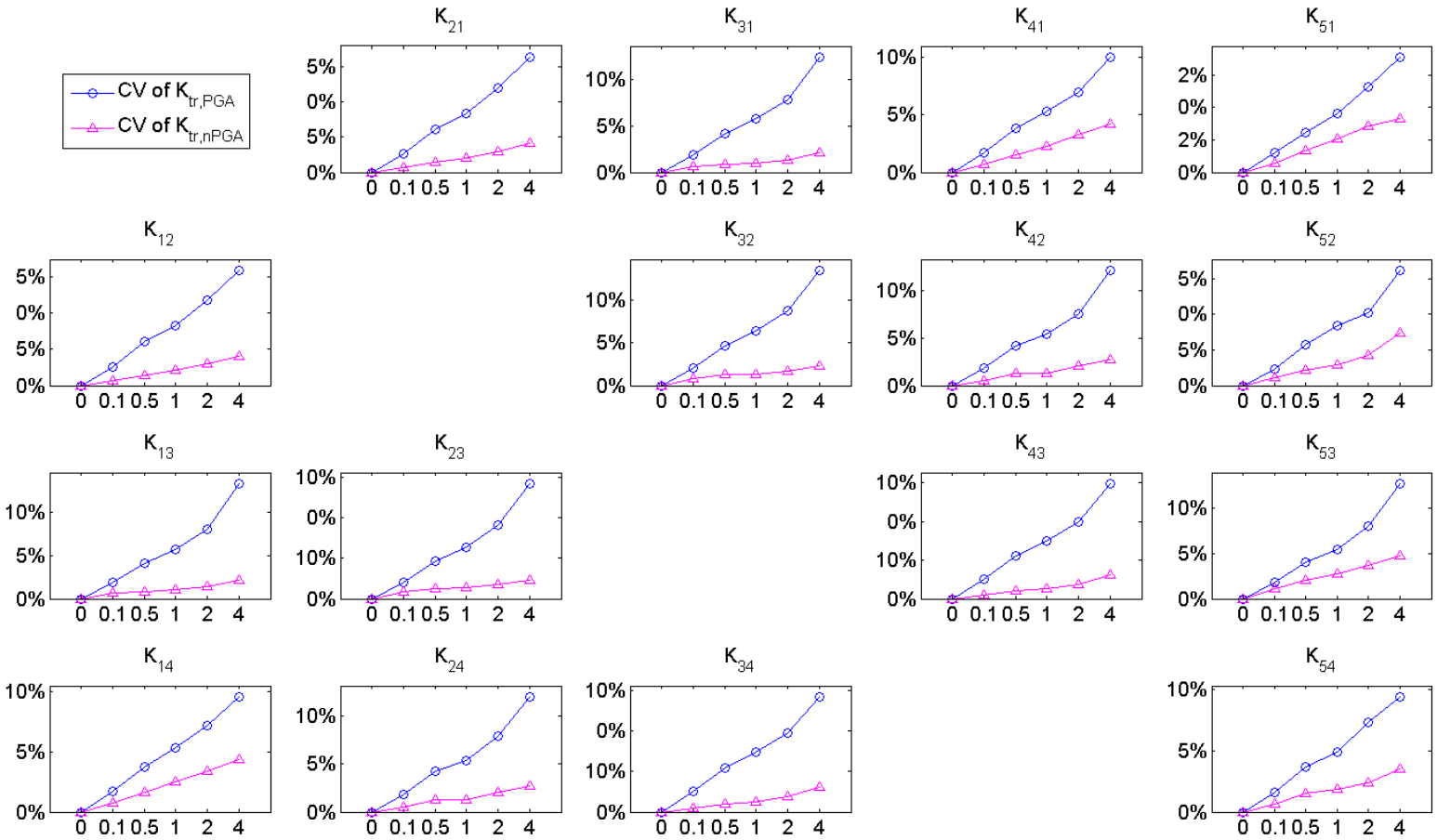

Figure 5-3 Plot of CVs of relative influx rate estimated by PGA and nPGA methods at different noise levels. In all the sub-figures, the vertical axis denotes the CV in percentage, and the horizontal axis denotes the noise level c, which could be set to 0, 0.1, 0.5, 1, 2 and 4. The blue open circle markers indicate the CV values of $K_{\mathrm{tr,PGA}}$ under different noise levels, while the magenta open triangle markers are for those of $K_{\mathrm{tr,nPGA}}$. The solid lines reflect the change tendencies of CVs with the increase of the noise level.

5.4.4 Effect of Kinetic Model in Parameter Estimation

The biases of the relative influx rates derived by PGA and nPGA methods were calculated comparing with their true values from the kinetic model. The four kinetic models that were used in the study of the effect of the kinetic model were the three-compartment four-parameter model with vascular volume (3c4pVb), the three-compartment four-parameter model without vascular volume (3c4p), the three-compartment three-parameter model (k4=0) with vascular volume (3c3pVb), and the three-compartment three-parameter model (k4=0) without vascular volume (3c3p). K_{tr} was estimated using the PGA and nPGA methods. Table 5-6 lists the percent bias of K_{12} and K_{52} derived by PGA and nPGA method compared with their true values for the simulated TTACs at a noise level of 0.

Table 5-6 Percent bias of K_{12} and K_{52} of PGA and nPGA compared with true values for different model at noise level c=0.

Models		**3c4pVb**	**3c4p**	**3c3pVb**	**3c3p**
$\boldsymbol{K_{12}}$	**PGA**	2.7%	11.6%	7.5%	2.0%
	nPGA	6.4%	6.1%	15.9%	1.2%
$\boldsymbol{K_{52}}$	**PGA**	30.7%	16.3%	23.5%	0.9%
	nPGA	13.6%	6.0%	11.6%	0.03%

The lowest bias with the 3c3p model (≤2.0%) was achieved for both PGA and nPGA. The introduction of k_4 in the 3c4p model led to the bias increasing to about 10% for PGA and 6% for nPGA. The addition of the vascular volume in the kinetic model led to another increase of at least 5% for PGA and nPGA.

5.5 Discussion

From the results of the small-animal studies and computer simulations presented in this chapter, it can be determined that the nPGA method was not efficient when the liver was used as either the reference ROI or the target ROI. The PGA method is originally proposed for the simplified FDG model with one irreversible compartment for FDG-6-PO_4 in tissue (k_4=0). Since the nPGA method originates from the PGA method, nPGA should be efficient for tissues with a low value of k_4. If k_4 is sufficiently lower than the other rate constants, the tracer can be assumed to be irreversibly trapped and k_4 can be neglected. However, this assumption of tracer kinetics is violated in the liver. The results of the estimated rate constants in Table 5-1 show that for the liver the average k_4 was comparable with k_3, whereas in the brain, where nPGA and PGA methods performed better, the average k_4 was approximately 10% of k_3. Furthermore, the use of a dual blood input has been proposed for tracer kinetic modeling of the liver [104, 134] in order to precisely reflect the FDG kinetics in this organ. However, it is impractical to delineate ROIs of the hepatic artery and portal vein of the liver in mice due to the small size of the vessels and the limited spatial resolution of the scanner.

The FDG kinetics in muscle ROIs can be reflected by a four-compartment and five-parameter model [135]. The simplified kinetic models that underlie the PGA and nPGA methods might lead to errors during the estimation of parameters. However, high linear correlation of the relative influx was still observed when the muscle was chosen as the reference as shown in Table 5-3, while low linear correlation was achieved when the muscle was chosen as the target region. It

seems that the comparably lower K_1 in the muscle may contribution to such the discrepancy for the muscle.

The three-compartment and four-parameter FDG kinetic model with vascular volume (3c4pVb) was used in WNLS fitting for the experimental data and computer simulations. This was because, according to the Akaike Information Criteria (AIC) and Schwarz Criteria (SC), this model provides the best fit TTACs for the brain and lungs compared to other models. For the lungs, the 3c4pVb model has the lowest AIC and SC values (AIC_{3c4pVb}= -304.8±45.7 and SC_{3c4pVb}= -297.3±45.7) compared with those of the 3c3pVb model (AIC_{3c3pVb}= -259.2±30.4 and SC_{3c3pVb}= -253.2±30.4) and the 3c3p model (AIC_{3c3p}= -235.8±31.2 and SC_{3c3p}= -231.3±31.3). The 3c4pVb model was also chosen as golden standard to analyze the FDG kinetics in lungs [136]. Although the general FDG model (3c4pVb) was not the best model for the liver and muscles, it is reasonable to apply the general FDG model in the simulation and provide referenced parameters because the focus of this study was to evaluate the performance of nPGA compared with traditional PGA in whole-body mouse studies in order to avoid the requirement of invasive blood samples which is challenging in small animal studies. The use of the general FDG model provided a simple and practical approach in the investigation, which is also consistent with previous mice investigations in the literatures [108, 133, 137].

The computer simulations were performed under varied noise levels in order to evaluate the effects of noise on the PGA and nPGA methods. From the results, it was discovered that the average $K_{\mathrm{tr,PGA}}$ and $K_{\mathrm{tr,WNLS}}$ changed very slightly as the noise level increased. This demonstrated that the relative influx rate was

insensitive to varied noise levels. Moreover, the results of the CVs indicated that the reliability of $K_{\mathrm{tr,PGA}}$ became worse than that of $K_{\mathrm{tr,nPGA}}$ with increasing noise levels. This may imply that the use of a reference ROI somehow reduces the effect of noise in the generation of the relative influx rate of the target ROI. Hence, the nPGA method could be applied to PET images that have a low signal-to-noise ratio.

It is not surprising to observe that different biases were obtained for nPGA and WNLS because different models were used in these two methods. When the 3c3p model was used for WNLS fitting, biases that were ≤2% were observed for the PGA and nPGA methods. The addition of k_4 in the model led to a 10% increase of the bias in the fitting. Comparing the 3c3p and 3c3pVb models shows that the introduction of vascular volume also resulted in a 10% increase in the bias. No significant increase of bias was observed for nPGA between the 3c3pVb and 3c4pVb models. This may imply that the procedure for the estimation of the relative influx rate in the nPGA method somehow compensates for the bias during the calculation of the influx rates of the individual ROIs using PGA method.

When the target ROI was placed on the tumor in the computer simulations, the accuracy of the relative influx rate achieved by the nPGA method was considerably higher than that obtained by the PGA method. A high linear correlation was also achieved between $K_{\mathrm{tr,nPGA}}$ vs. $K_{\mathrm{tr,WNLS}}$ and $K_{\mathrm{tr,nPGA}}$ vs. $K_{\mathrm{tr,PGA}}$ for the tumor target in small animal studies. The relative influx rates derived by the nPGA method were reasonably close to the values of $K_{\mathrm{tr,WNLS}}$ compared to those obtained via the PGA method in small animal studies. This implies that the nPGA method may be superior in the non-invasive quantification

of tumors when a suitable reference is available. Because the nPGA method is based upon the PGA method, a suitable reference could be a tissue with low k_4 in the general FDG kinetic model, where the tracer can be assumed to be irreversibly trapped. The results of the mouse studies show that the values of k_4 for the brain, lungs and muscle were relatively lower. Moreover, the results of linear regressions showed that the brain, lungs and muscle could be used as suitable references for the derivation of acceptable relative influx rates by the nPGA method. If the tracer kinetics of the target and reference regions are very distinct, the nPGA method would have a better performance. This may be the reason for the good results obtained for the tumor target, where the FDG kinetics are very different from other regions.

The range of data used in the PGA method can have an impact the on the estimate of the slope in the linear plot. This causes a slight instability in the PGA method. In previous studies, the range of the data has been recommended as 3-22 minutes in order to minimize the effect of k_4 [90, 108]. The range of data used in the PGA method was adopted in order to obtain the target influx rates for ROIs of the selected major organs. The optimal range of the data used in nPGA cannot be derived from the processes that deduce the nPGA method. Thus, a range of $t >$ 3 minutes was used in the nPGA method presented in this paper. Finding the optimal range of the nPGA method warrants further investigation using a larger preclinical dataset.

According to (2-5), MRGlc of the target region can be calculated as (5-9) using relative influx reate when the lump constant is assumed to be uniform in the

reference and target regions. This is allowed to quantify the MRGlc of target tissue when the appropriate reference chosen.

$$MRGlc_{\mathrm{tg}} = MRGlc_{\mathrm{ref}} \frac{K_{\mathrm{tg}}}{K_{\mathrm{ref}}} = MRGlc_{\mathrm{ref}} \times K_{tr} \tag{5-9}$$

The performance of PGA method is often compared with the standard uptake value (SUV), a popular semi-quantitative index, in cancer diagnosis and therapy evaluation [138, 139]. In a future study, the performance of nPGA method will be investigated by comparing with SUV or target to background ratio (TBR) in accurate tumor detection and therapy monitoring. Further investigations could also show that the nPGA method is potentially useful for tumor quantification in human studies.

5.6 Summary

The performance of the nPGA method was systematically investigated by a set of whole-body FDG-PET studies of mice and corresponding computer simulations. The results of the computer simulations demonstrated that for most ROIs, the nPGA method was as accurate as and more reliable than the PGA method. The results of the mouse studies showed that a high linearity of relative influx rates was achieved between nPGA and PGA for most target and reference pairs, when an appropriate underlying kinetic model was used. Considering its simplicity in implementation and the benefits of being a non-invasive technique, the nPGA method could provide a practical solution for the non-invasive quantification of glucose metabolism based on proper selection of reference region in whole-body FDG-PET studies of small-animals, in cases where the contribution

of k_4 and the vascular effect can be neglected. In particular, it could be recommended as a non-invasive and indirect method for quantifying the MRGlc of tumor in preclinical studies.

Chapter 6

Automatic Estimation of Input Function for Dynamic Small-Animal PET Imaging

6.1 Introduction

Chapter 5 has introduced a non-invasive method, nPGA, to measure the MRGlc using the relative influx rate in the small-animal PET imaging. However, the image-derived input function (IDIF) methods referred in **2.5.1**, which rely on a sufficiently large vascular structure in the imaging field of view (FOV), are more direct and convenient than reference region method and population-based method to precisely derive PTAC for estimations of the individual biological parameters. Especially for small-animal PET imaging, the entire body of the subject is often located in the FOV including the heart which could be assumed as a large blood pool. In the exiting IDIF methods, the PTAC can be obtained by simply placing a ROI on a large blood cavity such as left ventricle of the heart [98, 140]. TTACs can be obtained from other ROIs placed on the target tissues for the further quantitative analysis using tracer kinetic modeling. The quality of the ROI delineation depends

upon the experience of the operator. This manual approach is subjective, labor-intensive, and time-consuming, and as such semi- or fully-automatic ROI delineation methods that utilize some objective criterion are necessary in order to overcome these disadvantages.

Despite the significant efforts that have gone into attempting to achieve automatic delineation or segmentation in PET images as reviewed in **1.3**, there are still issues that need to be addressed today. These previous clustering methods handled the TACs or the sinograms as sequences of discrete points in vector form and did not utilize the potentially valuable smoothness or continuous temporal information. Specific statistical techniques based on the regression mixtures framework have been introduced to directly address curve clustering. These techniques could be considered as model-based clustering [141]. Curve clustering using polynomial regression mixture models (PRMMs) is the most computationally efficient method among these statistical techniques.

In this chapter, a novel hybrid clustering method (HCM) was developed based on the method of curve clustering with PRMMs for the automatic delineation of ROIs that will be used to estimate IDIF.

6.2 Theory of Hybrid Clustering Method

The proposed HCM for automatic ROI delineation consisted of three major steps: Step 1: background removal, Step 2: curve clustering with polynomial regression mixture models (PRMMs), and Step 3: classes merging, respectively. The

overall approach is depicted in Figure 6-1. The processes would be described in detail using an FDG-PET image as an example.

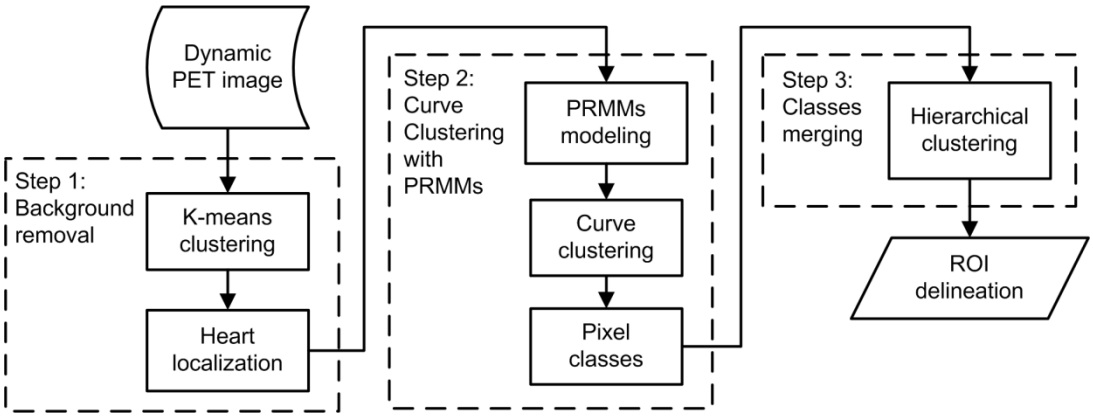

Figure 6-1 Flowchart of the proposed HCM for ROI delineation

6.2.1 Background Removal

In this step, the heart was coarsely localized prior to delineating the myocardium ROI (ROI_{myo}) and blood cavity ROI (ROI_{blc}). The background that was removed included pixels outside the scanned subject, which contained only noise and reconstruction artifacts, and pixels of tissues with lower activities, such as muscles, fat and skin. In late frames, the pixels depicting the heart had higher time-activities than their surroundings. However, it was possible that the bladder could also have high activities during the late frames. As such, only the thoracic part of the FDG-PET image was processed in this step, in order to exclude the bladder based on prior anatomical knowledge. K-means clustering was used to cluster all the pixels of the truncated thoracic FDG-PET image into several classes based on the different magnitudes of tracer activities in the last frame (~60min post tracer injection). This was achieved by minimizing the cost function given by (6-1).

$$\theta = \sum_{j=1}^{k} \sum_{i=1}^{n} \left\| A_i^j - C_j \right\|^2 \quad (6\text{-}1)$$

where, A_i^j is the activity of the i[th] pixel assumed to be in the j[th] class, C_j is the center of the j[th] class, which can be initialized as the equal distance center in dataset. k is the cluster number, and n is the number of pixels in the j[th] class, which can be updated in each iteration.

The pixels in the class with the highest average activity were denoted as a coarse part of the heart. a binary mask was then created in which these pixels were set to be one; the remaining pixels were set to zero, as they were considered to be part of the background and would therefore be removed. In the next two steps, this heart mask was applied to individual temporal frames of the FDG-PET image in order to obtain the coarse heart localization, which included the entire heart as well as parts of surrounding tissues such as partial lungs and blood vessels.

6.2.2 Curve Clustering with PRMMs

Every pixel in a dynamic PET image has a corresponding TAC, which can be represented as a sequence of discrete activities. This sequence has a length of T. The imaging time points can be considered to be a vector x_i. Let n be the number of pixels in the preliminary heart mask obtained from Step 1. These pixels could then be represented as a set of n TACs $\{y_1, y_2, \cdots, y_n\}$. A p^{th} order polynomial regression relationship was assumed between each TAC y_i and the imaging time points x_i with additive Gaussian noise term ε_i, as given by (6-2).

$$y_i = X_i\beta + \varepsilon_i, \qquad \varepsilon_i \sim \mathcal{N}(0, \sigma^2 I) \tag{6-2}$$

where $y_i \in \mathcal{R}^T$ is the TAC of the i[th] pixel, β is the vector containing the p regression coefficients, and X_i is the $T \times p$ Vandermonde regression matrix evaluated at the imaging time points $x_i = [x_{i1} \quad x_{i2} \quad \cdots \quad x_{iT}]^T$, which is formulated as (6-3).

$$X_i = \begin{bmatrix} 1 & x_{i1} & x_{i1}^2 & \cdots & x_{i1}^p \\ 1 & x_{i2} & x_{i2}^2 & \ldots & x_{i2}^p \\ \vdots & \vdots & \vdots & \ddots & \vdots \\ 1 & x_{i\mathrm{T}} & x_{i\mathrm{T}}^2 & \ldots & x_{i\mathrm{T}}^p \end{bmatrix} \tag{6-3}$$

Therefore, the conditional probability density function (PDF) of y_i can be modeled in terms of the regression equation as a normal distribution $\mathcal{N}(y_i|X_i\beta, \sigma^2 I)$. This PDF represents a probabilistic curve model that is associated with a curve cluster. If the set of TACs was separated into K distinct clusters in accordance to the similarity of the physiological kinetics, the density of a TAC y_i could be described as a finite mixture model with a number of component PDFs whose densities were noted by the parameters $\{\beta_k, \sigma_k^2\}$ as $\mathcal{N}(y_i|X_i\beta_k, \sigma_k^2 I)$. In other words, these cluster-dependent PDFs were incorporated into a conditional mixture density model given by (6-4). This resulted in the definition of the PRMMs for curve clustering.

$$p(y_i|X_i, \Theta) = \sum_{k=1}^{K} \alpha_k \, \mathcal{N}(y_i|X_i\beta_k, \sigma_k^2 I) \tag{6-4}$$

where α_k denotes the probability that the i$^{\text{th}}$ TAC y_i is assigned to cluster k. The mixture model parameters $\Theta = (\beta, \sigma^2, \alpha)$ were estimated by maximizing the log-likelihood function of n observed TACs, as given by (6-5).

$$L(Y|\Theta) = \sum_{i=1}^{n} \log\left(\sum_{k=1}^{K} \alpha_k \, \mathcal{N}(y_i|X_i\beta_k, \sigma_k^2 I) \right) \tag{6-5}$$

An expectation-maximization (EM) algorithm was adopted to search the maximum log-likelihood estimates of the parameters for the probabilistic curve model. These parameters depended upon unobserved latent variables.

The latent variable z_i was used to indicate the cluster membership for the TAC y_i. In the E-step, the posterior probability $p(z_i = k|y_i, X_i)$, which indicates the probability of the TAC y_i belonging to the cluster k, was calculated by (6-6).

$$w_{ik} = p(z_i = k|y_i, X_i) = \frac{\alpha_k \mathcal{N}(X_i\beta_k, \sigma_k^2 I)}{\sum_{k=1}^{K} \alpha_k \mathcal{N}(X_i\beta_k, \sigma_k^2 I)} \tag{6-6}$$

In the M-step, the expected value of the complete log-likelihood was maximized with respect to the parameters β_k, σ_k^2 and α_k. This allowed us to calculate updated solutions for mixture model parameters using (6-7).

$$\begin{cases} \hat{\beta}_k = \left[\sum_{i=1}^{n} w_{ik} X_i' X_i\right]^{-1} \sum_{i=1}^{n} w_{ik} X_i' y_i \\ \hat{\sigma}_k = \frac{\sum_{i=1}^{n} w_{ik} \|y_i - X_i\beta_k\|^2}{\sum_{i=1}^{n} w_{ik}} \\ \hat{\alpha}_k = \frac{\sum_{i=1}^{n} w_{ik}}{n} \end{cases} \tag{6-7}$$

After the convergence of the EM algorithm, the polynomial regression function for each cluster could be expressed in terms of the regression coefficients β. The clusters of TACs were thus defined by obtaining the cluster membership from the model parameters. The n pixels within the heart mask could be divided into K classes, based on their corresponding TACs. During the next step, the refined ROI delineations would be obtained by utilizing these K classes.

6.2.3 Classes Merging

In dynamic FDG-PET studies, it is assumed that equilibrium will be reached between plasma and free tissue concentration after a sufficiently long time (approximately 30 minutes) post tracer administration. This process is recorded in the late frames. Moreover, the late frames of dynamic FDG-PET images usually

have a higher SNR than early frames as they have a relatively longer scanning duration. As a result, it is possible that the images of different tissues could be clearer and more stable in the late frames compared to the early frames. The activity information in the late frames was suitable for refining the ROI delineation.

The heart, which is the indispensable organ for the blood circulation, is primarily composed of cardiac muscle tissue. This tissue forms the ventricles and atriums. The heart can be proposed to be divided into two structures: the myocardium and the blood cavity. The heart mask defined in **6.2.1** may include some surrounding tissues, such as partial lung tissue and large blood vessels. After considering the properties of dynamic PET images and the characteristics of the heart's anatomy, the classes derived from **6.2.2** were merged into three major clusters using the activity information from the last three individual frames. This was achieved through hierarchical clustering. The complete linkage clustering algorithm was applied to iteratively merge the two classes with the smallest distance as calculated in (6-8).

$$d(A_m, A_n) = \|A_m - A_n\|^2 = \sum_{i=1}^{3} (A_{mi} - A_{ni})^2 \qquad (6\text{-}8)$$

where A_m and A_n represent the average time activities of the pixels within two distinct classes m and n for the last three individual frames.

The pixels within the heart mask were finally separated into three distinct clusters: one is for the myocardium; another for the blood cavity, and a final cluster for the surrounding tissue. The ROI_{blc} was defined to be the cluster whose mean TAC had the highest peak. The ROI_{myo} was defined from the cluster that had a mean TAC with a high tail, i.e. higher myocardium activity was expected in the late

frames. ROI_{myo} and ROI_{blc} were then recorded as binary images and the ROI delineation was refined by a “morphological opening” operation (see Appendix B) that used a diamond-shaped structuring element with distance of 1 to remove pixel-size artifacts and noise.

6.2.4 Parameters of the HCM

The numbers of clusters for these three steps described before were set as the parameters of the proposed HCM. To achieve optimal performance in ROI delineation, the parameters used in the HCM were chosen empirically according to the properties of the FDG-PET image. The heart, lungs, and muscles were considered as the major organs observed in a thoracic PET image. The muscles often have relatively lower activities in the late frames of dynamic FDG-PET images. As such, they formed a cluster along with the parts outside the scanned subject. For background removal, we therefore set the number of clusters for the K-means clustering in Step 1 to 3. The number of clusters for curve clustering was empirically set to 5 for the detection of small structures. This setting was more stable than having 4 clusters and was less computationally expensive than 6. For Step 3, we set the number of clusters for hierarchical clustering to 3 because the typical properties of FDG concentrations in the heart could lead to the myocardium, the blood cavity and the surrounding tissue being produced as three distinct clusters.

The proposed hybrid clustering method for the ROI delineation was evaluated by the simulation studies in the following sections, and then applied for automatic estimation of the IDIF in a set of mouse FDG-PET studies.

6.3 Estimation of Imaged-Derived Input Function

The basic of the image-derived input function (IDIF) with spillover correction has been introduced in **2.5.1**. By considering (2-25) and (2-26) together, the $\tilde{C}_{\mathrm{b}}(t)$ was used as the new input for the represented model with the dual outputs of $\tilde{C}_{\mathrm{t}}(t)$ and $C_{\mathrm{p}}(t)$. There were six unknown parameters in this represented model: four rate constants (k_1, k_2, k_3, and k_4) and two spillover factors (f_m^b and f_b^m). These parameters were given initial values empirically and were then estimated by fitting the outputs of the model to the measurements of the PET and one blood sample, using the WNLS method to minimize the objective function given in (6-9).

$$\Phi(\theta) = \sum_{i=1}^{N} w_i \left(\tilde{C}_{\mathrm{t}}^{*}(t_i) - \tilde{C}_{\mathrm{t}}(t_i)\right)^2 + w_{\mathrm{b}} \left(C_{\mathrm{p}}(t_s) - p(t_s)\right)^2 \qquad (6\text{-}9)$$

where θ is the vector of parameters, which includes the rate constants for the compartment model and the mixing coefficients for the spillover effects. $\tilde{C}_t^*(t_i)$ and $\tilde{C}_t(t_i)$ are the estimated and measured mean time activities of the myocardium at time t_i (from the i$^{\text{th}}$ frame). w_i is the weight that is calculated as the ratio between the duration of the i$^{\text{th}}$ frame and $\tilde{C}_t(t_i)$ [133]. $C_p(t_s)$ is the TAC of the spillover corrected input function at time t_s, and $p(t_s)$ is the plasma time-activity of blood sample at time t_s. w_b is the weight for the blood sample, which is chosen to be a large value (e.g. 3) so that the measurement from this real blood sample is given more weight [53].

The dispersion and delay of the PTAC usually occur during the circulation of the tracer from heart to the either sampling site or target tissue. This could potentially induce an estimation error for the IDIF compared with the gold standard,

which is obtained by taking the blood samples from femoral catheter. In this case, the dispersion and delay corrections were applied to the IDIF that was already corrected for spillovers [142]. The corrected IDIF can be expressed by (6-10).

$$C_{\mathrm{IDIF}}(t+\Delta) = C_{\mathrm{p}}(t) \otimes \frac{e^{-t/\tau}}{\tau} \tag{6-10}$$

where $C_{IDIF}(t)$ is the corrected input function based on the spillover corrected IDIF, $C_p(t)$, τ is the dispersion time constant which is set as 1 sec, and Δ is the delay time usually measured in seconds [133], which is set as 2.5 sec.

The automatic estimation of the IDIF were applied to a set of mouse FDG-PET studies. The predicted IDIF was compared with the gold standard, which was the PTAC derived from invasive blood samples.

6.4 Computer Simulations

6.4.1 Digimouse Phantom Simulations

A number of dynamic FDG-PET studies were simulated to evaluate the performance of the proposed HCM for ROI delineation. The typical FDG TTACs for different thoracic tissues (myocardium, lungs and surrounding muscles) and blood TAC were generated using the Integrated Whole Body Kinetics Experimentation Lab of the virtual experimentation module in the Kinetic Imaging System (KIS) [81], following a routine 60-minute scanning protocol (1×2s, 10×0.4s, 3×5s, 1×30s, 2×60s, 1×120s, 3×180s, and 5×550s) and a 13.5MBq bolus FDG injection. The parameters of the integrated whole body kinetics experimentation were set to the default values in KIS. The typical TAC of the blood cavity, derived from the blood TAC, included about 50% spillover from the myocardium. The four

typical TACs plotted in Figure 6-2 were assigned to the corresponding tissue regions in a single slice of the Digimouse phantom [143] for generating the homogeneous image without noise. A slice of the phantom included the heart (the myocardium and an added blood cavity), lungs, and surrounding muscles, as shown in Figure 6-3.

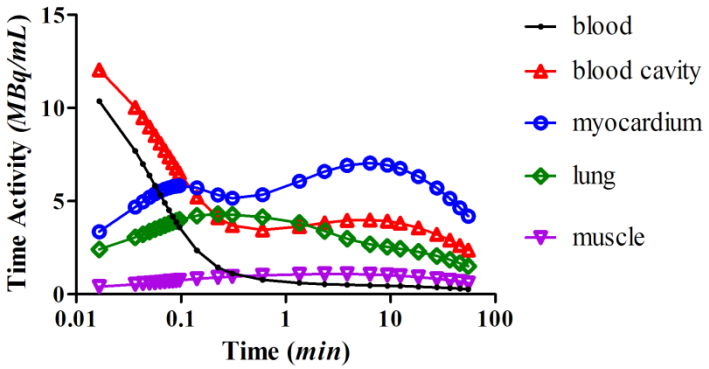

Figure 6-2 The typical FDG TACs for the major thoracic tissues (myocardium, blood cavity, lungs and surrounding muscles) and blood TAC in 60 min.

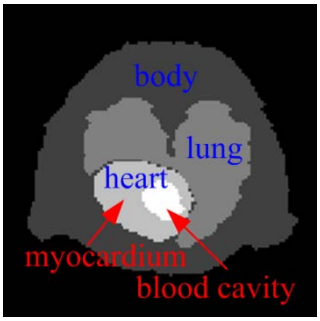

Figure 6-3 A transverse slice of the Digimouse phantom. An extra blood cavity was added inside the heart position, while the rest part of the heart was considered to be the myocardium.

The generated noise-free image was forward projected to obtain a dynamic sequence of sinograms. A normally distributed background related to the scanning duration was added to the sinograms in order to simulate the random and scattering events. Poisson noise was added and amplified by a noise level (0.5, 1, and 2). The noisy sinograms were then used to reconstruct the dynamic PET image frame by

frame, using filtered back-projection with a Hann filter and a cutoff frequency based on the Nyquist frequency. A realistic PET measurement was then generated by applying the Gaussian blur function to the reconstructed noisy PET image. This allowed us to simulate the influences from partial volume effects and physiological movements.

The proposed HCM was used to delineate the ROI_{myo} and ROI_{blc} in the simulated PET images. Generally, the entire measured TACs, each about 60 minutes in duration, were used in Step 2 of the HCM. This process was noted as HCM with entire TACs (HCM_60). Since the peak of the input function is mainly contained in the TACs of the first minute, partial TACs were considered to be sufficient for the detection of the blood cavity. When the partial TACs of the first minute were used in Step 2, the process was recorded as HCM with the first minute partial TACs (HCM_1). A standard clustering was introduced here in addition to these two HCM. After applying the same process of background removal of the HCM, the measured TACs in the heart mask could be considered as *T*-dimensional feature vectors. K-means clustering was then used to classify these feature vectors. This method was noted as K-means clustering method (KCM) and compared with HCM in automatic ROI delineation.

All three approaches (HCM_1, HCM_60 and KCM) were evaluated for the automatic ROI delineation under different noise levels.

6.4.2 Evaluation of the ROI Delineation

The ground truth for each ROI was defined according to the Digimouse phantom. Due to the limited spatial resolution, partial volume effects and the spillover of the PET image, the ROI was usually placed at the core part of the target

tissue or organ, where the TACs were representative of the target's theoretical kinetics with the least impacts from local surroundings and physiological movements. The Digimouse phantom was processed with the same Gaussian blur function that was applied to the reconstructed noisy PET image. The ground truth was then obtained by excluding the blurred margin of the target in the phantom while retaining the stable parts.

The automatically delineated ROI_{myo} and ROI_{blc} were compared with the ground truth, and evaluated using their sensitivity, specificity, and Dice Similarity Coefficient (DSC), which were calculated as given in (6-11) [144]. DSC measures the overlap between the areas of the estimated ROI and the ground truth. The automatically delineated ROI and the ground truth were respectively noted as ROI and GT in the calculations.

$$\begin{cases} \text{Sens.} = \dfrac{TP}{TP + FN} \\ \text{Spec.} = \dfrac{TN}{TN + FP} \\ \text{DSC} = 2 \times \dfrac{TP}{TP + FN + TP + FP} \end{cases} \tag{6-11}$$

where $TP = ROI \cap GT$ is the number of true positives, i.e. the count of pixels common to both ROI and GT; $TN = \overline{ROI} \cap \overline{GT}$ is the number of true negatives, i.e. the count of pixels that were not labeled by neither ROI nor GT; $FN = \overline{ROI} \cap GT$ is the number of false negatives, i.e. the count of pixels that were not labeled by ROI but were labeled by GT; and $FP = ROI \cap \overline{GT}$ is false positives, i.e. the count of pixels that were labeled by ROI but were not labeled by GT.

The mean TACs were also derived from the automatically delineated ROI_{myo} and ROI_{blc}. They were compared with the mean TACs obtained from the ground truth by the root mean square (RMS) and correlation coefficient (ρ).

6.4.3 Results

Figure 6-4 shows the five frames (3s, 6s, 36s, 561s, and 3306s after tracer injection) of the simulated dynamic FDG-PET image under a noise level of 1. The intensity of each pixel in the frames is noted as the magnitude of the time-activity in *MBq/mL*.

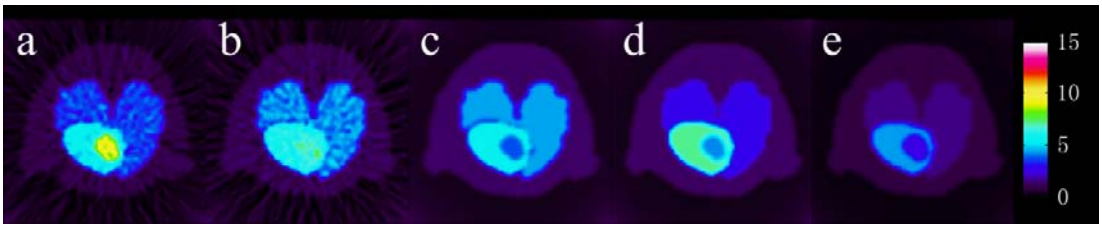

Figure 6-4 Five frames of the simulated dynamic FDG-PET image under noise level of 1. (a) 3s post tracer injection. (b) 6s post tracer injection. (c) 36s post tracer injection. (d) 561s post tracer injection. (e) 3306s post tracer injection.

100 runs were simulated for each noise level in order to compare the performance and reliability of the three proposed approaches (HCM_1, HCM_60 and KCM) in ROI definition. As mentioned in **6.2.4**, the parameters of the HCM were chosen empirically: the number of clusters for background removal was set to 3, the number of curve clusters was set to 5, and the number of clusters for hierarchical clustering was set to 3. The number of K-means clusters for background removal in KCM was the same as HCM, when the number of K-means clusters in KCM was set to 3.

Table 6-1 shows the performance of three approaches in ROI delineation. From our results, it is found that all the ROIs obtained automatically from the three approaches had high sensitivity and specificity (>0.9) when compared with the ground truth. The DSCs of the automatically delineated ROIs from HCM_1 and HCM_60 were around 10% higher than those from KCM. The correlation coefficient of the mean TACs were high for HCM (nearly 1.0). The RMS values for

HCM were about 2/3 lower than those for KCM. The results indicated that the HCM obtained more precise ROI delineation than KCM when compared with the ground truth.

Table 6-1 The Mean Values of The Evaluation Metrics*

Method	ROI# noise level	Myocardium DSC	Sens.	Spec.	ρ	RMS
HCM_1	0.5	0.936	0.913	0.999	0.999	0.264
	1	0.934	0.913	0.999	0.998	0.278
	2	0.930	0.914	0.998	0.998	0.293
HCM_60	0.5	0.950	0.948	0.999	0.999	0.192
	1	0.949	0.949	0.998	0.999	0.196
	2	0.948	0.949	0.998	1.000	0.193
KCM	0.5	0.837	0.990	0.999	0.994	1.061
	1	0.848	1.000	0.989	0.995	0.735
	2	0.830	0.980	0.989	0.995	1.383
Method	**ROI# noise level**	**Blood Cavity DSC**	**Sens.**	**Spec.**	**ρ**	**RMS**
HCM_1	0.5	0.894	1.000	0.998	1.000	0.615
	1	0.894	1.000	0.998	1.000	0.626
	2	0.893	1.000	0.998	1.000	0.625
HCM_60	0.5	0.889	1.000	0.998	1.000	0.649
	1	0.889	1.000	0.998	1.000	0.651
	2	0.883	1.000	0.998	1.000	0.697
KCM	0.5	0.787	1.000	0.996	0.995	1.723
	1	0.791	1.000	0.996	0.999	1.640
	2	0.781	1.000	0.995	0.990	1.848

* The evaluation metrics included Dice Similarity Coefficient (DSC), Sensitivity (Sens.), Specificity (Spec.), Root Mean Square (RMS), and the Correlation Coefficient (ρ). They were used to compare the automatic ROIs obtained by HCM_1, HCM_60 and KCM across three noise levels.

Figure 6-5 gives examples of ROI definitions obtained by the three approaches (HCM_1, HCM_60 and KCM) under a noise level of 2. In each sub-picture of Figure 6-5 the automatic ROI_{myo} is sketched by a red solid line along its contour, while its ground truth is highlighted in green. The automatic ROI_{blc} is shown with a blue solid line, while its ground truth is represented in magenta. The result shown in Figure 6-5(a) was obtained by HCM_1, whose corresponding DSCs were respectively 0.939 and 0.906 for ROI_{myo} and ROI_{blc}. The RMS values for the estimated mean TACs were about 0.211 and 0.488, while their correlation coefficients were both 0.999. The corresponding DSCs were 0.980 and 0.902 for HCM_60 as shown in Figure 6-5(b), and 0.863 and 0.785 for KCM as depicted in Figure 6-5(c).

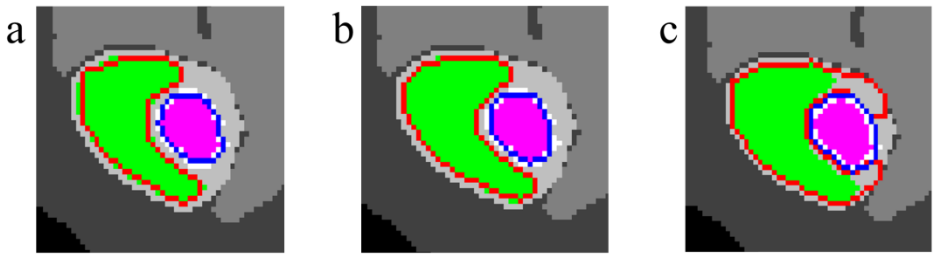

Figure 6-5 The delineations of the automatic ROI_{myo} and ROI_{blc} obtained by (a) HCM_1, (b) HCM_60, and (c) KCM. The contours of the automatic ROI_{myo} and ROI_{blc} are sketched by red and blue solid line, while the ground truths are respectively highlighted by green and magenta on the Digimouse phantom.

During the complete 60 minutes scanning time, the peak that occurred in the first minute post tracer injection reflected the typical feature of the TACs from ROI_{blc}. The tail part that appeared at 30 minutes after tracer injection represented the typical feature of the TACs from ROI_{myo}. HCM_1 used partial TACs of the first minute for curve clustering with PRMMs. Thus, the cluster of TACs from ROI_{blc} was accurately defined by HCM_1. HCM_60 used entire TACs for curve clustering

and as such the tail part led to the accurate clustering of TACs for ROI_{myo}. As a result, HCM_1 performed better in the delineation of ROI_b than HCM_60, while HCM_60 was better at delineating ROI_{myo}.

Early frames usually have a lower SNR than late frames as they have a shorter scanning duration. This could potentially impact the results of ROI delineation. Although small artifacts and noise could be removed by morphological processing, the contours of ROIs obtained by HCM_60 were smoother than those derived by HCM_1, as depicted in Figure 6-5. The blurred parts were included in the ROIs derived from KCM. However, the ground truth has been defined as the core part of the target neglected the burred margins. Hence, KCM had the higher sensitivity but the lower DSC than HCM.

6.5 Small-Animal Studies

6.5.1 Dynamic Mouse FDG-PET Studies

Twelve dynamic FDG-PET studies of mouse were obtained from http://dragon.nuc.ucla.edu/mqp/index.html, which is a public domain for mouse FDG-PET image datasets originally collected at the Department of Molecular and Medical Pharmacology at UCLA [113]. The data were acquired from non-fasted C57BL/6 mice with an average weight of 28g. The mice were anesthetized with ~2% isoflurane. A 60 minute dynamic PET scan was performed for each mouse on a microPET Focus 220 scanner after a tail vein bolus injection of approximately 13*MBq* FDG. For seven of these twelve studies, the dynamic PET image was reconstructed with a 29-frame imaging protocol: 1×3s, 10×0.5s, 1×2s, 1×4s, 6×5s,

1×10s, 2×30s, 2×120s, 1×180s, 2×600s, and 2×900s frames. Two of the remaining five datasets were conducted with a 26-frame imaging protocol: 1×2s, 10×0.4s, 3×5s, 1×30s, 2×60s, 1×120s, 3×180s, and 5×550s frames. Two other studies followed a 31-frame image protocol: 14×0.5s, 1×2s, 1×4s, 1×6s, 3×10s, 1×60s, 2×120s, 3×180s, and 5×550s. The final study had a 32-frame imaging protocol that was 15×0.4s, 1×2s, 1×4s, 1×6s, 2×15s, 3×30s, 1×60s, 1×120s, 3×180s, and 3×900s. After 60-minute PET imaging, a 10-minute computed tomography (CT) scan was acquired on a MicroCAT II. The CT image was aligned to PET image. The PET image was reconstructed using the filtered back-projection algorithm with CT-based attenuation correction [123]. The dead-time, scatter, and radiation-decay corrections were performed using software provided by the vendor. Around 16 blood samples were manually taken from a femoral catheter during the dynamic PET imaging.

We adopted the proposed HCM and KCM to delineate the ROIs for the automatic estimation of the IDIF in the mouse FDG-PET studies. It is possible for the proposed HCM to work on 3D images as it utilizes only temporal information rather than spatial information. The HCM could be adapted to make use of spatial information if it was necessary to cluster contiguous regions. In this study, the HCM and KCM were performed independently on each transverse slice in order to reduce the computational complexity. In addition, the HCM_1 was selected for this evaluation, because the simulation study demonstrated that HCM_1 produced comparably accurate ROIs to HCM_60 while having a lower computational cost.

6.5.2 Evaluation of the ROI Delineation and IDIF Estimation

ROIs were manually drawn in the myocardium and blood cavity by an experienced operator for the later evaluations. As the blood cavity has a very small size, the ROIs were defined in one transverse slice where there was a clearly defined blood cavity, e.g. left ventricle. The manually drawn ROIs were used as a standard to evaluate the ROIs obtained automatically by HCM or KM from the same transverse slice. In a similar manner to the evaluation of the computer simulation studies, the DSC of each automatic ROI and the correlation coefficient (ρ) of its mean TAC was calculated.

To evaluate the predicted IDIF, the PTAC derived from the invasive blood samples using (6-12) (the same as given in (5-5)) [90] was used as the gold standard.

$$\begin{cases} C_{\mathrm{GS}}(t) = B(t) \times R_{\mathrm{FDG}}(t) \\ R_{\mathrm{FDG}}(t) = 0.38e^{-0.191t} + 1.165 \end{cases} \tag{6-12}$$

where $C_{GS}(t)$ is the gold standard derived from the whole blood samples $B(t)$. $R_{PB}(t)$ is the FDG concentration ratio of plasma to whole blood.

This gold standard (GS) was used to evaluate the predicted IDIF, which was corrected for spillovers, delay and dispersion. The area under the curve (AUC), a commonly used criterion in the evaluation for the estimation of input functions [133, 145, 146], was calculated by (6-13). The AUC for the predicted IDIF (AUC_{IDIF}) and the gold standard (AUC_{GS}) were calculated with an integral interval that ranged from 0 to 60 minutes.

$$AUC = \int_0^t C_{\mathrm{IF}}(\tau)\, d\tau \tag{6-13}$$

where $C_{\mathrm{IF}}(\tau)$ is the predicted IDIF or the gold standard input function.

After re-sampling the predicted IDIF to the sampling time points of the blood samples, we used (6-14) to calculate the ratio of the non-overlapping area and AUC_{GS}. This was used as a supplementary criterion for evaluating the estimation of the IDIF.

$$r = \frac{\sum_{i=1}^{N} |eIF_i - GS_i| * int_i}{AUC_{GS}} \tag{6-14}$$

where eIF_i is the re-sampled value from the predicted IDIF at the i^{th} blood sampling time point, GS_i is the i^{th} measured value of the gold standard, and int_i is the i^{th} blood sampling interval.

The influx rate constant (K_i) was estimated for three selected target tissues (brain, myocardium, and muscle). This influx rate constant, which is an appropriate quantitative index for measuring glucose metabolism, can be estimated by the PGA method (introduced in **2.3.3**) using the predicted IDIF or the gold standard as input function. For calculating the Patlak K_i, the mean TTACs for the brain and muscles were obtained using the manually drawn ROIs. The mean TTAC of the myocardium was obtained from the automatic ROI_{myo}. These influx rate constants estimated using the predicted IDIF and the gold standard were compared in pairs for each tissue in the evaluation.

6.5.3 Results

The means and standard deviances (SD) of evaluation metrics (the DSC and correlation coefficient (ρ) of the mean TACs) were calculated in order to compare the performance of HCM_1 and KCM in automatic ROI delineation. The results are listed in Table 6-2. The ROIs derived automatically by HCM_1 were highly congruent with the corresponding manually derived ROIs, while KCM failed to

delineate the ROI_{myo} and ROI_b for most cases in the mouse studies. The ROIs derived automatically by HCM_1 had a DSC about 0.670 and 0.762 on average for ROI_b and ROI_{myo}, respectively, when compared with the manually defined ROIs across the 12 mouse studies. The best ROI delineation was obtained using HCM_1, where the values of DSC were 0.747 and 0.871 for ROI_b and ROI_{myo}, respectively. The lowest DSC of the ROI derived automatically by HCM_1 was about 0.419. Much lower mean values with higher SD were observed in the results of the KCM method. For direct comparison, the best and worst cases of ROI delineation using HCM_1 and KCM are shown in Figure 6-6. The correlation coefficient (ρ) was used for the calculation and comparison of the mean TACs for the ROIs derived automatically and manually. For HCM_1, the mean values of ρ were about 0.99 for ROI_{myo} and ROI_b: these were higher than the ρ for the ROIs obtained by KCM.

Table 6-2 The Mean and Standard Deviance (SD) of The Evaluation Metrics For The ROIs Derived By HCM_1 and KCM*

Method	**ROI#**	**Myocardium**		**Blood Cavity**	
	Metrics	DSC	ρ	DSC	ρ
HCM_1	Mean	0.762	0.991	0.670	0.990
	SD	0.075	0.009	0.115	0.008
KCM†	Mean	0.269	0.465	0.362	0.786
	SD	0.321	0.491	0.358	0.225

* The evaluation metrics included Dice Similarity Coefficient (DSC), and Correlation Coefficient (ρ). They were used to compare the automatic ROIs obtained by HCM_1 and KM across12 mice studies.

† For KCM,the DSC and ρ of failed cases were recorded as 0 in the statistical computations. There were 6 cases failed to get ROI_{myo} across 12 mice studies. In addition, other 3 cases lost the ROI_b.

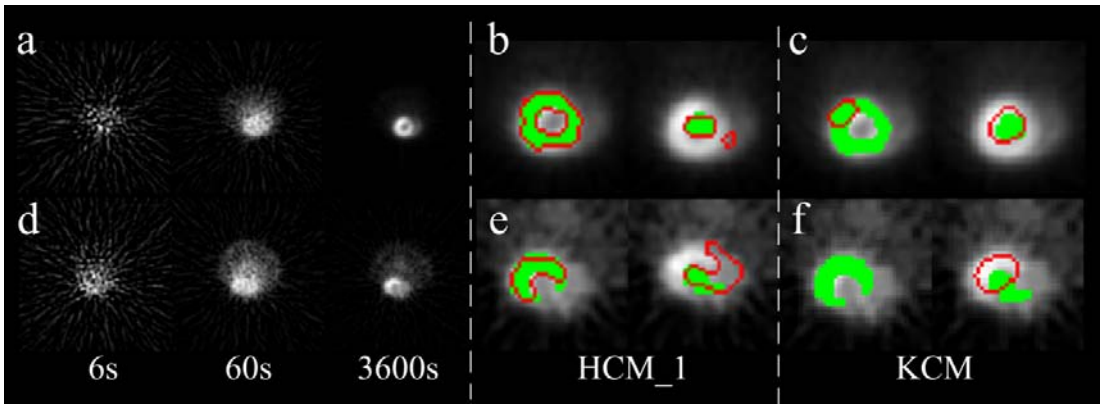

Figure 6-6 Illustrations of the best and worst cased of ROI delineation among the 12 mice studies. The top row shows the best case (m17332) of ROI delineation using HCM_1 and the results from KCM for comparison. The bottom row depicts the worst case (m19019) using HCM_1 and the results from KCM for comparison. (a) and (d) show the original PET image frames at about 6s, 60s and ~3600s post injection. (b) and (e) exhibit the ROIs derived automatically from HCM_1 compared with the manual ROIs. (c) and (f) display the results from KCM. In (f), KCM failed to get ROImyo. In (b), (c), (e) and (f), the left sub-figure shows the results of automatic ROI delineation compared with the ground truth for myocardium, while the right sub-figure shows the same for the blood cavity. The contours of the automatically derived ROIs are sketched using a red solid line, while the manually defined ROIs are colored in green.

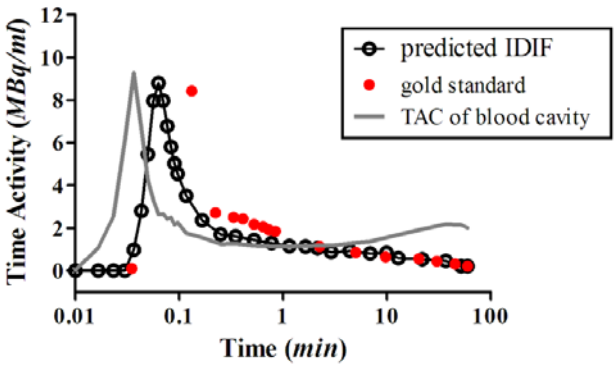

Figure 6-7 The plot of the predicted IDIF for one mouse (m17332) comparing with gold standard obtained from invasive blood sampling.

The mean TACs of the ROIs obtained automatically by HCM_1 were used to estimated the IDIF. The predicted IDIF was processed for spillover, dispersion, and

delay correction. Figure 6-7 shows one example comparison of the predicted IDIF and the gold standard.

The IDIF estimation was evaluated by comparing AUC_{IDIF} with AUC_{GS}. The ratio between the non-overlapping area and AUC_{GS} was calculated for the predicted IDIF. The Patlak K_i estimated using the predicted IDIF was compared with that derived using the gold standard for each selected target tissue. Linear regression was then performed to evaluate the results of the predicted IDIF.

In Figure 6-8(a), the AUC_{IDIF} is plotted against the AUC_{GS} for all 12 mouse studies. The slope of liner regression was 0.990 and R^2 was 0.974. The percentage of the absolute error between AUC_{IDIF} and AUC_{GS} was about 4.4%±3.0% on average. The Wilcoxon signed-rank test did not detect significant difference ($P>0.05$) between AUC_{IDIF} and AUC_{GS}. Furthermore, the average ratio between the non-overlapping area and AUC_{GS} across the 12 mouse studies was 0.18±0.04. The plots of the linear regression of the Patlak K_i are shown in Figure 6-8(b) for the brain, Figure 6-8(c) for the myocardium, and Figure 6-8(d) for the muscles. The slope were all close to 1 with high R^2 (>0.9). The percentage of the absolute error of the Patlak K_i was 5.3%±4.9% when considering all the results of three target tissues as a group. According to the Wilcoxon signed-rank test, the Patlak Ki estimated by the predicted IDIF was not significantly different ($P>0.05$) from that obtained by the gold standard for each target tissue.

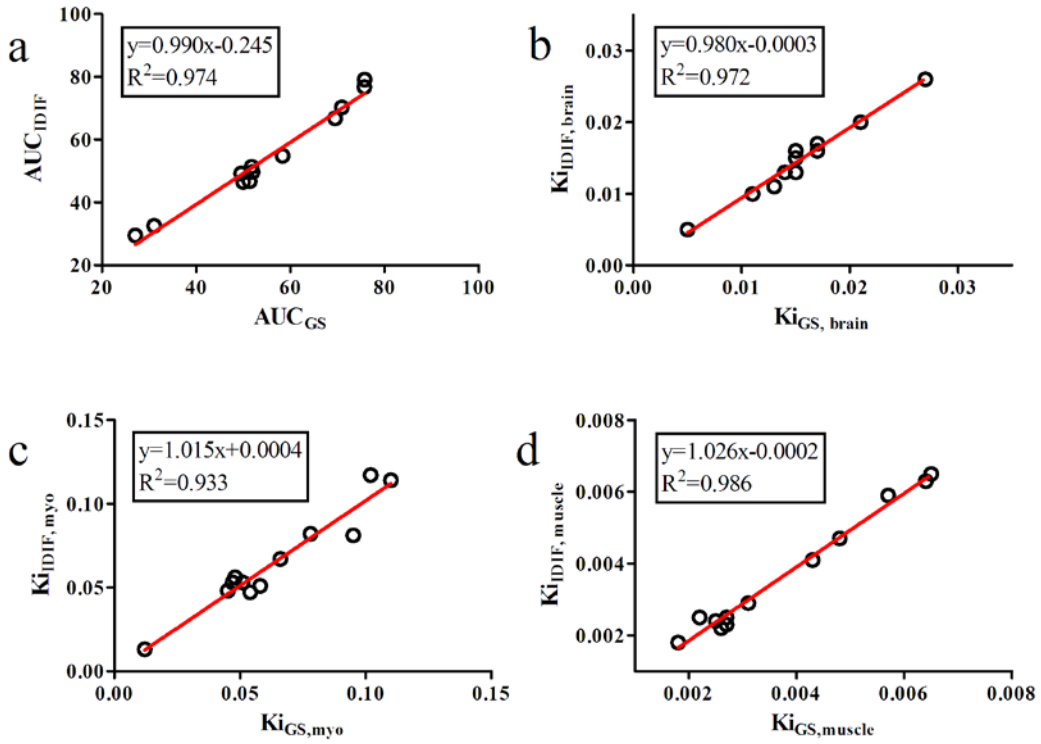

Figure 6-8 Comparison of (a) the AUC of the predicted IDIF and the gold standard (GS), (b) the Patlak K_i of the brain, (c) the Patlak K_i of the myocardium, and (d) the Patlak K_i of the muscles.The results of linear regression are shown in the legends.

6.6 Discussion

The results showed that the proposed hybrid clustering method (HCM) was effective in delineating ROIs for the myocardium and the blood cavity in the heart, using computer simulations and actual small-animal studies. In general PET studies, the pixels preferred for forming the ROI are the pixels within the region that are further from the border of the target organ, tissue or structure. When obtaining the theoretical kinetics, these pixels are less likely to be effected by the spillover and physiological movements that affect the pixels near the border. Therefore it is necessary for the automatic ROI delineation to also exclude the blurred borders in

the forming the ROIs. Furthermore, the limited spatial resolution and relatively higher noise of PET images usually hamper ROI definition in small structures, such as the blood cavity in the heart. HCM has demonstrated that it possesses an advantage over K-means clustering for these cases in simulated and experimental FDG-PET studies. The success of the HCM has a critical dependency on curve clustering with PRMMs as it is the key step of the HCM. It contributes to the extraction of the curve-specific memberships for clustering. In this step, the curve clustering employs a polynomial fit to restrain noise fluctuations and reduce the impact of clustering. On the other hand, curve clustering methods that represent the TACs by probabilistic curve models can be considered as curve modeling techniques that naturally allow for curves of variable lengths and missing measurements. As a particular type of modeling technique, curve clustering with PRMMs has proven to be more efficient in dealing with curves with missing measurements than non-curve-based techniques, such as Gaussian mixtures models [141]. In dynamic PET imaging, the time-activities of the pixels in early frames may be recorded as negative values because of high noise. These negative activities can be considered as missing measurements for the TACs. Hence, curve clustering with PRMMs is quite appropriate for clustering the TACs of dynamic PET images.

The results of the application of partial TACs from first minute were compared to that used entire TACs. One obvious effect of using partial TACs for curve clustering over entire TACs was a reduction in the computational expense, due to a smaller dataset being considered. The results of the computer simulation studies indicated that using partial TACs allowed us to obtain ROIs that were comparable to those obtained by using entire TACs. In addition, the use of partial TACs allowed us to derive more precise delineation of ROI_{blc}.

The HCM with partial TACs (HCM_1) and KCM were applied to automatically delineate ROIs in mouse FDG-PET studies. The TTAC of the myocardium is similar to the TAC of the blood cavity because the myocardium has an ample blood supply for the delivery of oxygen and nutrients. Their similarity of the shape and magnitude could be further increased by the partial volume effects and spillovers between these two regions. These factors could be potential reasons for the failure of the KM in correctly delineating ROIs in most of the mouse studies. The proposed HCM modeled the TACs using PRMMs for curve clustering. This allowed the use of all the kinetic information available in the TACs. Under the HCM, the pixels whose corresponding TACs were curve-specific members of the blood TACs cluster could be counted as part of ROI_{blc}. The ROI_{blc} derived automatically by HCM included several structures that contained a large amount of blood, in addition to the left ventricle where the manual ROI_{blc} was placed. This is the reason for the low DSC observed in some cases. The ROIs of blood cavity could also have been placed in these blood-filled structures, which include regions such as the right ventricle and the nearby aorta, for extraction of the reasonable input function [147, 148].

A noninvasive methodology for obtaining an input function is still an attractive topic in the quantitative analysis of PET images. IDIFs are well established and have been improved with the addition spillover correction, allowing for the derivation of more accurate PTACs [52, 147, 149]. There has recently been an increase in the number of small animal studies using microPET-CT, mainly due to the advent of booming biological techniques. It is still necessary to develop IDIFs for these studies. However, most proposed methods still continue to rely upon the manual placement of ROIs within the heart [133, 137]. Our proposed HCM was explored for

the fully automatic estimation of the input function. In this study, the well-established IDIF method with spillover, dispersion, and delay corrections was employed for the estimation of an IDIF using automatically derived ROIs. The results demonstrated that this technique was successful in deriving an IDIF that was comparable to the gold standard obtained from invasive blood samples.

The manual initialization of the IDIF parameters is a drawback of this method as it is largely dependent on the experience of the person setting the values. The accuracy of the estimation could be improved by initializing the IDIF parameters from the mean and SD of invasive blood samples taken from a small sample population with Bayesian parameter constrains [133].

Finally, this proposed HCM only needs to rely on the temporal information available in dynamic PET images for ROI delineation. Therefore the HCM can be applied to other organs by defining an ROI in large vascular structures, such as the carotid artery in the brain, as well as the hepatic arteries and the portal vein in the liver. The HCM could also be practically and reliably used for ROI delineation in PET images using other tracers.

6.7 Summary

In this chapter, a novel hybrid clustering method (HCM) has been explored for the delineation of ROIs in dynamic PET images. These automatically derived ROIs were used for the estimation of image-derived input function for small animal FDG-PET studies. The proposed HCM consisted of three steps: K-means clustering for background removal; curve clustering with PRMMs for the detection of classes; and

hierarchical clustering for merging classes. The high accuracy of ROI definitions were demonstrated in both computer simulations and small-animal studies. In the small-animal FDG-PET studies, the ROIs derived by the HCM were used for the automatic estimation of an IDIF with one blood sample. The predicted IDIF, which was corrected for spillovers, dispersion, and delay, had a high correlation with the gold standard, as calculated by the AUC and Patlak K_i. We believe the proposed HCM has great potential for automatic ROI delineation in small-animal dynamic FDG-PET studies and may extend for the general dynamic PET studies using other tracers.

Chapter 7

Conclusions and Future Work

7.1 Conclusions

As a powerful molecular imaging technique, PET provides unique approach to quantitatively study diverse biological processes *in vivo* with specific tracers and quantification techniques. The rapid development of information technology gives rise to opportunities for the accurate and convenient quantifications of PET studies. Hence, this thesis is devoted to develop the accurate and objective quantification techniques which aim to improve the reliability of quantification and facilitate the analysis of PET studies, particularly emphasising on the FDG-PET studies. The investigations in this thesis were concluded as follows:

Firstly, the studies of quantitative indexes were performed to improve the quantification quality. In Chapter 3, SUV, a common semi-quantitative index, was estimated and modified based on an automatic image-based method for static FDG-PET imaging. The imaged-derived SUV gave out a way to accurately quantify the tracer uptake in tissue when the actual measurement of body weight or injected dose was missing or unreliable. The modified SUV reduced the inter-subject variability

and enhance the tumor-to-background separation, which has the potential to increase the accuracy of malignancy detection. In addition to the improved SUVs, the imaging protocol was also studies for improving the quantification quality of PET imaging. A simulation framework was developed in Chapter 4 in order to improve the performance of dual-time FDG-PET imaging in lung cancer diagnosis. The generalized optimal quantitative index with its corresponding flexible dual-time imaging protocol was derived from the simulation framework and achieved the highest accuracy in differentiating malignancy from benign lesions for lung cancer diagnosis.

Secondly, the non-invasive approaches were developed to eliminate or minimize the requirements of invasive blood samples. This can make the quantification process of dynamic PET imaging more convenient and harmless. In Chapter 5, a non-invasive Patlak graphic analysis method is extended and adopted to quantify the tracer uptake in target tissue by relative influx rates under the support of selected reference in whole-body PET imaging. The computer simulations and experimental FDG-PET studies both demonstrated that high linearity of relative influx rates was achieved between non-invasive Patlak graphic analysis method and common Patlak graphic analysis method for most pairs of target and reference with appropriate underlying kinetic model. In Chapter 6, the image-derived input function method was studied to directly obtain PTAC from PET images with the corrections of spillover, delay and dispersion. In the experimental mouse FDG-PET studies, the predicted image-derived input function had a high correlation with the gold standard, the PTAC derived from invasive blood sampling.

Finally, the automatic analysis processes were explored to increase the convenience of PET studies, especially for the investigation based on large-scale database. In Chapter 3, an automatic image-based method was developed to derive improved SUVs: imaged-derived SUV and modified SUV. This automatic approach may profit the quantification in an inter-institution sharing database. Moreover, in Chapter 6, a novel hybrid clustering method was explored to automatically delineate the ROIs based on the fully usage of the dynamic information of time-activity curves from dynamic PET images. This method showed its advantage in automatic ROI delineation both in computer simulations and experimental mouse FDG-PET studies. This method had a great potential in ROI delineation for automatic estimation of image-derived input function in dynamic FDG-PET studies.

In a word, the major work of this thesis is to develop the accurate and convenient quantification techniques for the high quality quantitative PET imaging. The contributions in this thesis can be summarised as follows:

1. An automatic image-based method was explored to extract more information from microPET and microCT images in the quantification of static FDG-PET image. The image-derived SUV (iSUV) has the capability to replace SUV when the actual measurements were mission or unreliable. The modified SUV (mSUV) can reduce the inter-subject variability of SUV and enhance the tumor-to-background separation by subtracting the tracer extracted in bladder. Using this image-based method, the estimated iSUV is valuable for multidisciplinary and inter-institution large-scale database in education and scientific research. Meanwhile, the predicted mSUV has the potential to improve the performance in accurate malignancy detection.

2. A simulation framework was set up to find out the better solution for dual-time FDG-PET imaging in the lung cancer diagnosis. The generalized optimal quantitative index and its corresponding flexible imaging protocol were suggested to achieve the optimum performance of dual-time FDG-PET imaging.

3. A new non-invasive Patlak graphic analysis method was extended and applied in whole-body dynamic FDG-PET studies, where the relative influx rate is used to quantify the tracer uptake in certain tissue with the selected reference tissue. This non-invasive Patlak graphic analysis method brings not only the non-invasive benefit to quantification but also the simplicity in implementation with linear regression, so that it can provide a practical solution of non-invasive quantitative analysis for whole-body dynamic PET imaging.

4. A novel hybrid clustering method (HCM) based on curve clustering was proposed to automatically delineate the ROIs in dynamic PET images. This novel method was adopted in dynamic mouse FDG-PET studies to avoid the manual placement of ROIs in the estimation of image-derived input function. Moreover, this automatic ROI delineation has the potential to benefit the quantitative analysis for the dynamic PET studies using other tracers.

5. An automatic estimation of image-derived input function was developed based on the proposed HCM to avoid invasive blood sampling. The estimated image-derived input function was processed by the corrections of spillover, delay and dispersion for obtaining the accurate input function. This automatic approach is successfully applied in a set of experimental FDG-PET studies.

7.2 Future Work

This thesis has explored the effective methods to improve quantification techniques of PET studies especially for the FDG-PET imaging. Some of the proposed quantification techniques may also benefit the studies using other PET tracers or other applications. The more quantification techniques could be further developed based on the theory and results proposed in this thesis.

Firstly, for the automatic image-based method, the more valuable anatomical or structural parameters can be derived from the microPET/CT images. For example, body surface area can be obtained directly from the microCT image (e.g., by a marching cubes algorithm [126]) in the future work. Because using of body surface area has been reported in some studies to be preferable in SUV calculation [31], e.g. for obese subjects with increased fraction of body fat, the estimated body surface area can be used as the normalization factor instead of body weight in the calculation of SUV.

Secondly, because developing a suitable PET assay is a multi-discipline cooperation, an integrated system for quantitatively analyzing PET images needs to be developed to fill the gap in linking the knowledge among the varied disciplines including biology, physiology, pharmacology, physic, and mathematic *et al*. This integrated system can be able to assistant the operators in the simulation or the quantitative analysis for PET studies. The traditional quantification techniques as well as these novel approaches proposed in this thesis can be integrated as useful quantification modules for image-based or noninvasive analysis. In addition, the integrated system demands a notable module for Monte Carlo simulation, which can generate realistic PET data in different signals acquisition steps to assist the

developments of quantification techniques. Several software packages as well as the phantoms have been developed for the Monte Carlo simulation [150], such as PET-SORTEO [151] and GATE [152], which could be helpful for the set up the computer simulation module of the integrated system in the future.

Thirdly, while the computer aided detection/diagnosis (CAD) is widely studied for varied image modalities such as CT and MRI, the topic of automatic lesion detection becomes the attractive area. For PET imaging, the automatic lesion detection is much useful and urgently demanded for the CAD approaches in cancer diagnosis, staging even the therapy monitoring. However, there are many difficulties in using the routine image processing techniques to achieve the goals of CAD due to the low spatial resolutions and high noise levels in the PET images. In this case, the temporal information of dynamic PET image provides quite valuable features for lesion detection. Generally, the parametric image derived by tracer kinetic modeling can be used to detected disorder regions. However, the impacts of noise of single voxel kinetic can lead parametric imaging to a poor quality in small lesions detection, such as the metastasis lesion in oncology. In addition to the curve clustering approach described in this thesis, the matched subspace detector has the potential to automatically detect the lesions particularly the small lesions for dynamic PET images [153, 154]. There is still much room for refinement of the automatic lesion detection for PET imaging not only using the temporal information in the dynamic images but also using the spatial information in the aligned anatomical images.

Finally, because the molecular imaging has been matured in quantifying the different physiological parameters with specific image modalities, these parameters can be integrated into the mathematic models to practically reflect the concerned

biological process. The mathematic model integrated with quantitative parameters obtained from PET and MRI has shown the predictive value in modeling and simulating the tumor growth and the treatment response [155]. This previous research only starts an initial stage of mathematic modeling with the quantitative parameters derived from molecular imaging. A number of assumptions and simplifications could limit the biological relevancy of model, so that many improvements will be done for adjusting the mathematic model.

The outcomes of these continuing researches would have significant scientific and social impacts.

Appendix A

Imaging Technique	Portion of EM radiation spectrum used in image generation	[a] Spatial resolution	Depth	[b] Temporal resolution	[c] Sensitivity	[d] Type of molecular probe	Amount of molecular probe used	Quantitative degree
Positron emission tomography (PET)	high-energy gamma rays	1- 2 *mm*	no limit	10 *sec* to minutes	10^{-11} -10^{-12} *mole/L*	Radiolabeled direct or indirect	nanograms	+++
Single photon emission computed tomography (SPECT)	low-energy gamma rays	1-2 *mm*	no limit	minutes	10^{-10} - 10^{-11} *mole/L*	Radiolabeled direct or indirect	nanograms	++
Optical bioluminescence imaging	visible light	[f] 3-5 *mm*	1-2 *cm*	seconds to minutes	not well - characterized possibly 10^{-15} - 10^{-17} *mole/L*	[i] activatable indirect	micrograms to milligrams	+ to ++
Optical fluorescence imaging	visible light or near-infrared	[g] 2-3 *mm*	[h] <1 *cm*	seconds to minutes	not well - characterized possibly 10^{-9} - 10^{-12} *mole/L*	activatable direct or indirect	micrograms to milligrams	+ to ++
Magnetic resonance imaging (MRI)	radiowaves	25-100 μm	no limit	minutes to hours	10^{-3} - 10^{-5} *mole/L*	activatable direct or indirect	micrograms to milligrams	++
CT	X-rays	50-200 μm	no limit	minutes	not well characterized	may be possible	not applicable	not applicable
Ultrasound	high-frequency sound	50-500 μm	millimeters to centimeters	seconds to minutes	not well characterized	limited activatable, direct	micrograms to milligrams	+

[a] Spatial resolution is a measure of the accuracy or detail of graphic display in the image expressed in millimeters. It is the minimum distance between two independently measured objects that can be distinguished separately. It is a measure of how fine the image is.

[b] Temporal resolution is the frequency at which the final interpretable version of images can be recorded/captured from the subject once the image process is initiated. This relates to the time required to collect enough events to form an image, and to the responsiveness of the imaging system to rates of any change induced by the operator or in the biological system at hand.

Table continued

Ability to scale to human imaging	Perturbation of biological system	Principal use	Advantages	Disadvantages	[e] Cost
yes	no	metabolic reporter/gene expression, receptor/ligand, enzyme targeting	high sensitivity, isotopes can substitute naturally occurring atoms, quantitative translational research	PET cyclotron or generator needed, relatively low spatial resolution, radiation to subject	$$$$
yes	no	reporter/gene expression, receptor/ligand	many molecular probes available, can image multiple probes simultaneously may be adapted to clinical imaging	relatively low spatial resolution because of sensitivity, collimation, radiation	$$$
yes but limited	yes if necessary to give mass quantity of molecular probe	reporter/gene expression, cell trafficking	high sensitivity, quick, easy, low-cost, relative high-throughput	low spatial resolution, current 2D imaging only, relatively surface-weighted, limited translational research	$$
yes but limited	yes if necessary to give mass quantity of molecular probe	reporter/gene expression, cell trafficking	high sensitivity, detects fluorochrome in live and dead cells	[j] relatively low spatial resolution, surface-weighted	$ - $$
yes	yes if necessary to give mass quantity of molecular probe	morphological reporter/gene expression, receptor/ligand if many	highest spatial resolution, combines morphological and functional imaging	relatively low sensitivity, long scan and postprocessing time, mass quantity of probe may be needed	$$$$
yes	as MRI, and also if excessive radiation dose	morphological	bone and tumor imaging, anatomical imaging	limited "molecular" applications, limited soft tissue resolution, radiation	$$
yes	no	morphological	real-time, low cost	limited spatial resolution, mostly morphological	$$

[c] Sensitivity, the ability to detect a molecular probe when it is present, relative to the background, measured in moles per liter.
[d] Type of molecular probe. See text in [6].
[e] This includes cost of equipment and cost per study. For details of instrumentation vendors, visit Web site www.mi-central.org.
[f] Spatial resolution of bioluminescence and reflectance fluorescence is depth-dependent. For bioluminescence, the resolution is slightly worse or equal to the depth of the object, that is, an object 3-5 mm deep has an ~3-5 mm spatial resolution.
[g] Use of fluorescence tomography is likely to result in better spatial resolution.
[h] This depth applies to reflectance fluorescence. Fluorescence tomography can likely image objects at greater depths (2-6 cm).
[i] Bioluminescence may also offer direct means of imaging through the use of the use of the Renilla luciferase protein. Feasibility studies are underway.
[j] Except for fluorescence tomography, which has better spatial resolution and can image at greater depths.

Appendix B

Mathematical morphology, which stems from set theory, aims at analysing the shape and form of objects. In this thesis, the "morphological opening" and "morphological fill" operators were used to refine the results of image segmentation in **Chapter 3** and **Chapter 6**.

Morphological opening is defined based on the fundamental operations of erosion and dilation, which are normally applied to binary images. The erosion has two inputs: the original binary image and a set of coordinate points known as structuring element (SE). The erosion is defined as the locus of points that SE is included in the image set, as given in (A-1).

$$\varepsilon_S(X) = \{x | S_x \subseteq X\} \tag{A-1}$$

where $\varepsilon_S(X)$ denotes the erosion of an image set X by a SE S.

The dilation is defined as the locus of points where the SE hit the image set, as expressed by (A-2).

$$\delta_S(X) = \{x | S_x \cap X \neq \emptyset\} \tag{A-2}$$

where $\delta_S(X)$ denotes the dilation of an image set X by a SE, S.

Simply, opening is defined as erosion followed by a dilation using the same SE for both morphological operations. The expression of opening is shown in (A-3).

$$\gamma_S(X) = \bigcup_x \{S_x | S_x \subseteq X\} \tag{A-3}$$

where $\gamma_S(X)$ denotes the opening operation.

The “morphological opening” can filter out the small blobs in binary images. This effect is adopted for removing the small size artifacts and noise in the results of image segmentation. In addition, the “morphological fill" aims to fill the holes in the binary images. It performs using an algorithm based on morphological reconstruction which can be thought of conceptually as repeated dilations of an image.

The further information about the principles and applications of mathematic morphology in image analysis can be found in the reference [156].

Appendix C

The nPGA method proposed in **Chapter 5** originates from the PGA method, assuming that the whole-body is a SIMO system. For the PGA method, the FDG concentration could be expressed as a relationship with the PTAC as given in (A-4).

$$C_{\mathrm{t}}(t) = K_{\mathrm{i}} \int_0^t C_{\mathrm{p}}(\tau) d\tau + I\, C_{\mathrm{p}}(t), t > t^* \tag{A-4}$$

The TTACs of two distinct ROIs (one as acting as the reference ROI, the other being the target ROI) can be described by (A-5).

$$\begin{cases} C_{\mathrm{ref}}(t) = K_{\mathrm{ref}} \int_0^t C_{\mathrm{p}}(\tau) d\tau + I_{\mathrm{ref}}\, C_{\mathrm{p}}(t) \\ C_{\mathrm{tg}}(t) = K_{\mathrm{tg}} \int_0^t C_{\mathrm{p}}(\tau) d\tau + I_{\mathrm{tg}}\, C_{\mathrm{p}}(t) \end{cases}, t > t^* \tag{A-5}$$

According to (A-5), the PTAC can be presented by (A-6).

$$\begin{cases} \int_0^t C_{\mathrm{p}}(\tau) d\tau = \dfrac{I_{\mathrm{tg}} C_{\mathrm{ref}}(t) - I_{\mathrm{ref}} C_{\mathrm{tg}}(t)}{D} \\ C_{\mathrm{p}}(t) = \dfrac{-K_{\mathrm{tg}} C_{\mathrm{ref}}(t) + K_{\mathrm{ref}} C_{\mathrm{tg}}(t)}{D} \end{cases}, D = K_{\mathrm{ref}} I_{\mathrm{tg}} - K_{\mathrm{tg}} I_{\mathrm{ref}}, t > t^* \tag{A-6}$$

Equation (A-7) is obtained by integrating both sides of the second equation in (A-6).

$$\begin{aligned} \int_{t_0}^t C_{\mathrm{p}}(\tau) d\tau &= \int_{t_0}^t \frac{\left[-K_{\mathrm{tg}} C_{\mathrm{ref}}(\tau) + K_{\mathrm{ref}} C_{\mathrm{tg}}(\tau)\right]}{D} d\tau \\ &= \frac{-K_{\mathrm{tg}} \int_{t_0}^t C_{\mathrm{ref}}(\tau) d\tau + K_{\mathrm{ref}} \int_{t_0}^t C_{\mathrm{tg}}(\tau) d\tau}{D} \end{aligned} \tag{A-7}$$

Because $\int_0^t C_{\mathrm{p}}(\tau) d\tau = \int_0^{t_0} C_{\mathrm{p}}(\tau) d\tau + \int_{t_0}^t C_{\mathrm{p}}(\tau) d\tau, t > t_0 > t^*$ and $\int_0^{t_0} C_{\mathrm{p}}(\tau) d\tau = \left[I_{\mathrm{tg}} C_{\mathrm{ref}}(t_0) - I_{\mathrm{ref}} C_{\mathrm{tg}}(t_0)\right]/D$, (A-8) can be obtained from (A-6) and (A-7).

$$\frac{I_{\mathrm{tg}}C_{\mathrm{ref}}(t) - I_{\mathrm{ref}}C_{\mathrm{tg}}(t)}{D} = \frac{I_{\mathrm{tg}}C_{\mathrm{ref}}(t_0) - I_{\mathrm{ref}}C_{\mathrm{tg}}(t_0)}{D} + \frac{-K_{\mathrm{tg}}\int_{t_0}^{t} C_{\mathrm{ref}}(\tau)d\tau + K_{\mathrm{ref}}\int_{t_0}^{t} C_{\mathrm{tg}}(\tau)d\tau}{D} \tag{A-8}$$

To eliminate *D* in (A-8), a new equation expressing the relationship between two TTACs, is given by (A-9).

$$K_{\mathrm{ref}}\int_{t_0}^{t} C_{\mathrm{tg}}(\tau)d\tau = K_{\mathrm{tg}}\int_{t_0}^{t} C_{\mathrm{ref}}(\tau)d\tau + I_{\mathrm{tg}}[C_{\mathrm{ref}}(t) - C_{\mathrm{ref}}(t_0)] - I_{\mathrm{ref}}\left[C_{\mathrm{tg}}(t) - C_{\mathrm{tg}}(t_0)\right] \tag{A-9}$$

Finally, the nPGA method can be presented by the equation in (A-10). The relative influx rate can then be derived by liner least squares method.

$$\begin{aligned}\int_{t_0}^{t} C_{\mathrm{tg}}(\tau)d\tau &= \frac{K_{\mathrm{tg}}}{K_{\mathrm{ref}}}\int_{t_0}^{t} C_{\mathrm{ref}}(\tau)d\tau + \frac{I_{\mathrm{tg}}}{K_{\mathrm{ref}}}[C_{\mathrm{ref}}(t) - C_{\mathrm{ref}}(t_0)] \\ &\quad - \frac{I_{\mathrm{ref}}}{K_{\mathrm{ref}}}\left[C_{\mathrm{tg}}(t) - C_{\mathrm{tg}}(t_0)\right] \\ &= K_{\mathrm{tr}}\int_{t_0}^{t} C_{\mathrm{ref}}(\tau)d\tau + I_{\mathrm{tr}}[C_{\mathrm{ref}}(t) - C_{\mathrm{ref}}(t_0)] \\ &\quad - I_{\mathrm{rr}}\left[C_{\mathrm{tg}}(t) - C_{\mathrm{tg}}(t_0)\right], t > t_0 > t^*\end{aligned} \tag{A-10}$$

Bibliography

[1] M. E. Phelps, "Positron emission tomography provides molecular imaging of biological processes," *Proc Natl Acad Sci USA,* vol. 97, pp. 9226-9233, Aug 1 2000.

[2] R. Weissleder and U. Mahmood, "Molecular Imaging1," *Radiology,* vol. 219, pp. 316-333, May 2001.

[3] F. A. Jaffer and R. Weissleder, "Molecular Imaging in the Clinical Arena," *JAMA,* vol. 293, pp. 855-862, Feb16 2005.

[4] M. Rudin and R. Weissleder, "Molecular imaging in drug discovery and development," *Nat Rev Drug Discov,* vol. 2, pp. 123-131, Feb 2003.

[5] J. K. Willmann, *et al.*, "Molecular imaging in drug development," *Nat Rev Drug Discov,* vol. 7, pp. 591-607, 2008.

[6] T. F. Massoud and S. S. Gambhir, "Molecular imaging in living subjects: seeing fundamental biological processes in a new light," *Genes Dev,* vol. 17, pp. 545-580, Mar 1 2003.

[7] T. Beyer, *et al.*, "A Combined PET/CT Scanner for Clinical Oncology," *J Nucl Med,* vol. 41, pp. 1369-1379, Aug 1 2000.

[8] C. Catana, *et al.*, "Simultaneous in vivo positron emission tomography and magnetic resonance imaging," *Proceedings of the National Academy of Sciences,* vol. 105, pp. 3705-3710, Mar 11 2008.

[9] S. R. Cherry, *et al.*, "The Integration of Positron Emission Tomography With Magnetic Resonance Imaging," *Proceedings of the IEEE,* vol. 96, pp. 416-438, 2008.

[10] K. Herholz and W. D. Heiss, "Positron emission tomography in clinical neurology," *Mol Imaging Biol,* vol. 6, pp. 239-269, Jul-Aug 2004.

[11] R. Duara, *et al.*, "Positron emission tomography in Alzheimer's disease," *Neurology,* vol. 36, pp. 879-, Jul 1 1986.

[12] J. C. Mazziotta, *et al.*, "The use of positron emission tomography in the clinical assessment of dementia," *Seminars in Nuclear Medicine,* vol. 22, pp. 233-246, 1992.

[13] N. Tolboom, *et al.*, "Detection of Alzheimer Pathology In Vivo Using Both 11C-PIB and 18F-FDDNP PET," *J Nucl Med,* vol. 50, pp. 191-197, Feb 1, 2009 2009.

[14] H. R. Schelbert, "The usefulness of positron emission tomography," *Current Problems in Cardiology,* vol. 23, pp. 69-120, 1998.

[15] T. H. Schindler, *et al.*, "Cardiac PET Imaging for the Detection and Monitoring of Coronary Artery Disease and Microvascular Health," *J Am Coll Cardiol Img,* vol. 3, pp. 623-640, Jun 1 2010.

[16] R. Weissleder, "Molecular Imaging in Cancer," *Science,* vol. 312, pp. 1168-1171, May 26 2006.

[17] K. A. Wood, *et al.*, "Positron emission tomography in oncology: a review," *Clin Oncol (R Coll Radiol),* vol. 19, pp. 237-255, May 2007.

[18] S. S. Gambhir, "Molecular imaging of cancer with positron emission tomography," *Nat Rev Cancer,* vol. 2, pp. 683-693, 2002.

[19] R. Kumar and A. Chauhan, "Positron emission tomography: clinical applications in oncology. Part 2," *Expert Rev Anticancer Ther,* vol. 6, pp. 625-640, Apr 2006.

[20] R. Kumar, *et al.*, "Positron emission tomography: clinical applications in oncology. Part 1," *Expert Rev Anticancer Ther,* vol. 5, pp. 1079-1094, Dec 2005.

[21] L. Lu, *et al.*, "Rat Studies Comparing 11C-FMAU, 18F-FLT, and 76Br-BFU as Proliferation Markers," *J Nucl Med,* vol. 43, pp. 1688-1698, December 1, 2002 2002.

[22] S.-L. Song, *et al.*, "Changes in 18F-FDG Uptake Within Minutes After Chemotherapy in a Rabbit VX2 Tumor Model," *J Nucl Med,* vol. 49, pp. 303-309, Feb 1 2008.

[23] H. A. Wieder, *et al.*, "Time Course of Tumor Metabolic Activity During Chemoradiotherapy of Esophageal Squamous Cell Carcinoma and Response to Treatment," *Journal of Clinical Oncology,* vol. 22, pp. 900-908, Mar 1 2004.

[24] I. Penuelas, *et al.*, "Positron emission tomography and gene therapy: basic concepts and experimental approaches for in vivo gene expression imaging," *Mol Imaging Biol,* vol. 6, pp. 225-238, Jul-Aug 2004.

[25] Y. Waerzeggers, *et al.*, "Methods to monitor gene therapy with molecular imaging," *Methods,* vol. 48, pp. 146-160, Jun 2009.

[26] D. D. Feng, *et al.*, "Techniques for Parametric Imaing," in *Biomedical Information Technology*, D. D. Feng, Ed., ed: Elsevier, 2008, pp. 137-159.

[27] S. C. Huang, "Anatomy of SUV. Standardized uptake value," *Nucl Med Biol,* vol. 27, pp. 643-646, Oct 2000.

[28] L. M. Hamberg, *et al.*, "The Dose Uptake Ratio as an Index of Glucose Metabolism: Useful Parameter or Oversimplification?," *J Nucl Med,* vol. 35, pp. 1308-1312, Aug 1 1994.

[29] J. W. Keyes, Jr., "SUV: Standard Uptake or Silly Useless Value?," *J Nucl Med,* vol. 36, pp. 1836-1839, Oct 1 1995.

[30] B. J. Fueger, *et al.*, "Impact of Animal Handling on the Results of 18F-FDG PET Studies in Mice," *J Nucl Med,* vol. 47, pp. 999-1006, Jun 1 2006.

[31] C. K. Kim, *et al.*, "Standardized uptake values of FDG: body surface area correction is preferable to body weight correction," *J Nucl Med,* vol. 35, pp. 164-167, Jan 1994.

[32] J. A. Thie, *et al.*, "A weight index for the standardized uptake value in 2-deoxy-2-[F-18]fluoro-D-glucose-positron emission tomography," *Mol Imaging Biol,* vol. 9, pp. 91-98, Mar-Apr 2007.

[33] E. J. Hoffman, *et al.*, "Quantitation in positron emission computed tomography: 1. Effect of object size," *J Comput Assist Tomogr,* vol. 3, pp. 299-308, Jun 1979.

[34] C.-H. Chen, *et al.*, "Simultaneous Recovery of Size and Radioactivity Concentration of Small Spheroids with PET Data," *J Nucl Med*, vol. 40, pp. 118-130, Jan 1 1999.

[35] J. A. Thie, *et al.*, "Optimizing imaging time for improved performance in oncology PET studies," *Mol Imaging Biol*, vol. 4, pp. 238-244, May 2002.

[36] S. Beaulieu, *et al.*, "SUV Varies with Time After Injection in 18F-FDG PET of Breast Cancer: Characterization and Method to Adjust for Time Differences," *J Nucl Med*, vol. 44, pp. 1044-1050, Jul 1 2003.

[37] B. B. Chin, *et al.*, "Increasing uptake time in FDG-PET: standardized uptake values in normal tissues at 1 versus 3 h," *Mol Imaging Biol*, vol. 11, pp. 118-122, Mar-Apr 2009.

[38] S. Basu, *et al.*, "Novel quantitative techniques for assessing regional and global function and structure based on modern imaging modalities: implications for normal variation, aging and diseased states," *Semin Nucl Med*, vol. 37, pp. 223-39, May 2007.

[39] H. Zhuang, *et al.*, "Dual Time Point 18F-FDG PET Imaging for Differentiating Malignant from Inflammatory Processes," *J Nucl Med*, vol. 42, pp. 1412-1417, Sep 1 2001.

[40] A. Matthies, *et al.*, "Dual Time Point 18F-FDG PET for the Evaluation of Pulmonary Nodules," *J Nucl Med*, vol. 43, pp. 871-875, Jul 1 2002.

[41] R. Kumar, *et al.*, "Potential of dual-time-point imaging to improve breast cancer diagnosis with (18)F-FDG PET," *J Nucl Med*, vol. 46, pp. 1819-1824, Nov 2005.

[42] Y. Nishiyama, *et al.*, "Dual-time-point 18F-FDG PET for the evaluation of gallbladder carcinoma," *J Nucl Med*, vol. 47, pp. 633-638, Apr 2006.

[43] D. Uesaka, *et al.*, "Evaluation of dual-time-point 18F-FDG PET for staging in patients with lung cancer," *J Nucl Med*, vol. 49, pp. 1606-1612, Oct 2008.

[44] R. Jia, *et al.*, "Optimal dual time point for FDG-PET in the differentiation of benign from malignant lung lesions: a simulation study," presented at the Conf Proc IEEE Eng Med Biol Soc, Lyon, France, 2007.

[45] J. A. Thie, "Optimizing dual-time and serial positron emission tomography and single photon emission computed tomography scans for diagnoses and therapy monitoring," *Mol Imaging Biol,* vol. 9, pp. 348-356, Nov-Dec 2007.

[46] D. Feng, *et al.*, "A technique for extracting physiological parameters and the required input function simultaneously from PET image measurements: theory and simulation study," *IEEE Trans Inf Technol Biomed,* vol. 1, pp. 243-254, Dec 1997.

[47] K. P. Wong, *et al.*, "Simultaneous estimation of physiological parameters and the input function--in vivo PET data," *IEEE Trans Inf Technol Biomed,* vol. 5, pp. 67-76, Mar 2001.

[48] H.-M. Wu, *et al.*, "Factor Analysis for Extraction of Blood Time-Activity Curves in Dynamic FDG-PET Studies," *J Nucl Med,* vol. 36, pp. 1714-1722, Sep 1 1995.

[49] F. Hermansen, *et al.*, "Generation of Myocardial Factor Images Directly from the Dynamic Oxygen-15-Water Scan Without Use of an Oxygen-1 5-Carbon Monoxide Blood-Pool Scan," *J Nucl Med,* vol. 39, pp. 1696-1702, Oct 1 1998.

[50] D. Eidelberg, *et al.*, "Positron emission tomographic findings in Filipino X-linked dystonia-parkinsonism," *Ann Neurol,* vol. 34, pp. 185-191, Aug 1993.

[51] S. Eberl, *et al.*, "Evaluation of two population-based input functions for quantitative neurological FDG PET studies," *Eur J Nucl Med,* vol. 24, pp. 299-304, Mar 1997.

[52] K. P. Lin, *et al.*, "Correction of spillover radioactivities for estimation of the blood time-activity curve from the imaged LV chamber in cardiac dynamic FDG PET studies," *Phys Med Biol,* vol. 40, pp. 629-642, Apr 1995.

[53] D. Feng, *et al.*, "A new double modeling approach for dynamic cardiac PET studies using noise and spillover contaminated LV measurements," *IEEE Trans Biomed Eng,* vol. 43, pp. 319-327, 1996.

[54] V. J. Cunningham, *et al.*, "Compartmental analysis of diprenorphine binding to opiate receptors in the rat in vivo and its comparison with equilibrium data in vitro," *J Cereb Blood Flow Metab*, vol. 11, pp. 1-9, Jan 1991.

[55] S. P. Hume, *et al.*, "Quantitation of Carbon-11-labeled raclopride in rat striatum using positron emission tomography," *Synapse*, vol. 12, pp. 47-54, 1992.

[56] C. Svarer, *et al.*, "MR-based automatic delineation of volumes of interest in human brain PET images using probability maps," *Neuroimage*, vol. 24, pp. 969-979, 2005.

[57] F. Yasuno, *et al.*, "Template-Based Method for Multiple Volumes of Interest of Human Brain PET Images," *Neuroimage*, vol. 16, pp. 577-586, 2002.

[58] K.-P. Wong, *et al.*, "Segmentation of dynamic PET images using cluster analysis," *IEEE Trans Nucl Sci*, vol. 49, pp. 200-207, 2002.

[59] J. Kim, *et al.*, "Segmentation of VOI from multidimensional dynamic PET images by integrating spatial and temporal features," *IEEE Trans Inf Technol Biomed*, vol. 10, pp. 637-646, Oct 2006.

[60] Y. Kimura, *et al.*, "Fast formation of statistically reliable FDG parametric images based on clustering and principal components," *Phys Med Biol*, vol. 47, pp. 455-468, Feb 7 2002.

[61] R. Maroy, *et al.*, "Segmentation of Rodent Whole-Body Dynamic PET Images: An Unsupervised Method Based on Voxel Dynamics," *IEEE Trans Med Imaging*, vol. 27, pp. 342-354, 2008.

[62] M. Liptrot, *et al.*, "Cluster analysis in kinetic modelling of the brain: a noninvasive alternative to arterial sampling," *Neuroimage*, vol. 21, pp. 483-493, 2004.

[63] P. Zanotti-Fregonara, *et al.*, "Comparison of 3 Methods of Automated Internal Carotid Segmentation in Human Brain PET Studies: Application to the Estimation of Arterial Input Function," *J Nucl Med*, vol. 50, pp. 461-467, Mar 1 2009.

[64] S. Domenichelli, *et al.*, "Quantitative cardiac dynamic imaging of small animal PET images using cluster analysis," presented at the Computers in Cardiology, Bologna, Italy, 2008.

[65] M. E. Kamasak and B. Bayraktar, "Clustering Dynamic PET Images on the Projection Domain," *IEEE Trans Nucl Sci,* vol. 54, pp. 496-503, 2007.

[66] M. E. Kamasak, "Clustering dynamic PET images on the Gaussian distributed sinogram domain," *Comput Methods Programs Biomed,* vol. 93, pp. 217-227, 2009.

[67] S. R. Cherry and M. Dahlbom, "PET: Physics, Instrumentation and Scanners," in *PET: Molecular Imaging and Its Biological Applications*, M. E. Phelps, Ed., ed: Springer-Verlag, 2004, pp. 1-125.

[68] D. L. Bailey, "Data Acquisition and Performance Characterization in PET," in *Positron Emission Tomography: Basic Sciences*, D. L. Bailey, *et al.*, Eds., ed London: Springer-Verlag, 2005, pp. 41-62.

[69] C. Cobelli and M. P. Saccomani, "Accessible pool and system parameters: assumptions and models," *J Parenter Enteral Nutr,* vol. 15, pp. 45S-50S, May-Jun 1991.

[70] S. S. Gambhir, "Quantitative assay development for PET," in *PET: Molecular Imaging and Its Biological Applications*, M. E. Phelps, Ed., ed: Springer-Verlag, 2004, pp. 125-216.

[71] E. L. Forker and B. A. Luxon, "Lumpers vs. distributers," *Hepatology,* vol. 5, pp. 1236-1237, Nov-Dec 1985.

[72] M. E. Phelps, "PET: The Merging of Biology and Imaging into Molecular Imaging," *J Nucl Med,* vol. 41, pp. 661-681, Apr 1 2000.

[73] M. E. Phelps and J. C. Mazziotta, "Positron emission tomography: human brain function and biochemistry," *Science,* vol. 228, pp. 799-809, May 17 1985.

[74] M. E. Phelps, *et al.*, "Study of cerebral function with positron computed tomography," *J Cereb Blood Flow Metab,* vol. 2, pp. 113-62, 1982.

[75] E. M. Rohren, *et al.*, "Clinical applications of PET in oncology," *Radiology,* vol. 231, pp. 305-32, May 2004.

[76] L. Sokoloff, *et al.*, "The [14C]deoxyglucose method for the measurement of local cerebral glucose utilization: theory, procedure, and normal values in the conscious and anesthetized albino rat," *J Neurochem,* vol. 28, pp. 897-916, May 1977.

[77] M. E. Phelps, *et al.*, "Tomographic measurement of local cerebral glucose metabolic rate in humans with (F-18)2-fluoro-2-deoxy-D-glucose: validation of method," *Ann Neurol,* vol. 6, pp. 371-388, Nov 1979.

[78] S. C. Huang, *et al.*, "Noninvasive determination of local cerebral metabolic rate of glucose in man," *Am J Physiol,* vol. 238, pp. E69-82, Jan 1980.

[79] R. A. Hawkins, *et al.*, "Effects of temporal sampling, glucose metabolic rates, and disruptions of the blood-brain barrier on the FDG model with and without a vascular compartment: studies in human brain tumors with PET," *J Cereb Blood Flow Metab,* vol. 6, pp. 170-183, Apr 1986.

[80] Y. Zhou, *et al.*, "Improved Parametric Image Generation Using Spatial-Temporal Analysis of Dynamic PET Studies," *Neuroimage,* vol. 15, pp. 697-707, 2002.

[81] S. C. Huang, *et al.*, "An internet-based "kinetic imaging system" (KIS) for MicroPET," *Mol Imaging Biol,* vol. 7, pp. 330-341, Sep-Oct 2005.

[82] R. F. Muzic, Jr. and S. Cornelius, "COMKAT: Compartment Model Kinetic Analysis Tool," *J Nucl Med,* vol. 42, pp. 636-645, Apr 1 2001.

[83] P. H. R. Barrett, *et al.*, "SAAM II: Simulation, analysis, and modeling software for tracer and pharmacokinetic studies," *Metabolism,* vol. 47, pp. 484-492, 1998.

[84] D. Feng, *et al.*, "An evaluation of the algorithms for determining local cerebral metabolic rates of glucose using positron emission tomography dynamic data," *IEEE Trans Med Imaging,* vol. 14, pp. 697-710, 1995.

[85] D. Feng, *et al.*, "An unbiased parametric imaging algorithm for nonuniformly sampled biomedical system parameter estimation," *IEEE Trans Med Imaging,* vol. 15, pp. 512-518, 1996.

[86] D. Feng, *et al.*, "GLLS for optimally sampled continuous dynamic system modeling: theory and algorithm," *Comput Methods Programs Biomed,* vol. 59, pp. 31-43, 1999.

[87] J. Logan, "A review of graphical methods for tracer studies and strategies to reduce bias," *Nucl Med Biol,* vol. 30, pp. 833-844, Nov 2003.

[88] C. S. Patlak and R. G. Blasberg, "Graphical evaluation of blood-to-brain transfer constants from multiple-time uptake data. Generalizations," *J Cereb Blood Flow Metab,* vol. 5, pp. 584-590, Dec 1985.

[89] K. Wienhard, *et al.*, "Estimation of local cerebral glucose utilization by positron emission tomography of [18F]2-fluoro-2-deoxy-D-glucose: a critical appraisal of optimization procedures," *J Cereb Blood Flow Metab,* vol. 5, pp. 115-125, Mar 1985.

[90] H.-M. Wu, *et al.*, "In Vivo Quantitation of Glucose Metabolism in Mice Using Small-Animal PET and a Microfluidic Device," *J Nucl Med,* vol. 48, pp. 837-845, May 2007.

[91] J. Logan, *et al.*, "Graphical analysis of reversible radioligand binding from time-activity measurements applied to [N-11C-methyl]-(-)-cocaine PET studies in human subjects," *J Cereb Blood Flow Metab,* vol. 10, pp. 740-747, Sep 1990.

[92] J. Logan, *et al.*, "Effects of blood flow on [11C]raclopride binding in the brain: model simulations and kinetic analysis of PET data," *J Cereb Blood Flow Metab,* vol. 14, pp. 995-1010, Nov 1994.

[93] J. Logan, *et al.*, "Distribution Volume Ratios Without Blood Sampling from Graphical Analysis of PET Data," *J Cereb Blood Flow Metab,* vol. 16, pp. 834-840, 1996.

[94] G. J. Hunter, *et al.*, "Simplified Measurement of Deoxyglucose Utilization Rate," *J Nucl Med,* vol. 37, pp. 950-955, Jun 1 1996.

[95] K. Ishizu, *et al.*, "Effects of Hyperglycemia on FDG Uptake in Human Brain and Glioma," *J Nucl Med*, vol. 35, pp. 1104-1109, Jul 1 1994.

[96] K. Ishizu and Y. Yonekura, "Clarification of a Fractional Uptake Concept--Reply," *J Nucl Med*, vol. 36, p. 712, Apr 1 1995.

[97] J. A. Thie, "Clarification of a Fractional Uptake Concept," *J Nucl Med*, vol. 36, pp. 711-712, Apr 1 1995.

[98] S. S. Gambhir, *et al.*, "Simple Noninvasive Quantification Method for Measuring Myocardial Glucose Utilization in Humans Employing Positron Emission Tomography and Fluorine-18 Deoxyglucose," *J Nucl Med*, vol. 30, pp. 359-366, Mar 1 1989.

[99] R. Hinz, *et al.*, "Validation of a tracer kinetic model for the quantification of 5-HT2A receptors in human brain with [lsqb]11C[rsqb]MDL 100,907," *J Cereb Blood Flow Metab*, vol. 27, pp. 161-172, 2006.

[100] J.-S. Lee, *et al.*, "A novel blood-cell-two-compartment model for transferring a whole blood time activity curve to plasma in rodents," *Comput Methods Programs Biomed*, vol. 92, pp. 299-304, 2008.

[101] J. Krivokapich, *et al.*, "Estimation of rabbit myocardial metabolic rate for glucose using fluorodeoxyglucose," *Am J Physiol Heart Circ Physiol*, vol. 243, pp. H884-895, Dec 1 1982.

[102] K. Chen, *et al.*, "Noninvasive Quantification of the Cerebral Metabolic Rate for Glucose Using Positron Emission Tomography, 18F-Fluoro-2-Deoxyglucose, the Patlak Method, and an Image-Derived Input Function," *J Cereb Blood Flow Metab*, vol. 18, pp. 716-723, 1998.

[103] L. M. Wahl, *et al.*, "Regions of Interest in the Venous Sinuses as Input Functions for Quantitative PET," *J Nucl Med*, vol. 40, pp. 1666-1675, Oct 1 1999.

[104] S. Chen and D. Feng, "Noninvasive quantification of the differential portal and arterial contribution to the liver blood supply from PET measurements using the ¹¹C-acetate kinetic model," *IEEE Trans Biomed Eng*, vol. 51, pp. 1579-1585, 2004.

[105] N. Kudomi, *et al.*, "Non-invasive estimation of hepatic glucose uptake from [(18)F]FDG PET images using tissue-derived input functions," *Eur J Nucl Med Mol Imaging,* pp. 2014-2026, Jun 13 2009.

[106] K. Chen, *et al.*, "Characterization of the image-derived carotid artery input function using independent component analysis for the quantitation of [18F] fluorodeoxyglucose positron emission tomography images," *Phys Med Biol,* vol. 52, pp. 7055-7071, Dec 7 2007.

[107] L. A. Green, *et al.*, "Noninvasive Methods for Quantitating Blood Time-Activity Curves from Mouse PET Images Obtained with Fluorine-18-Fluorodeoxyglucose," *J Nucl Med,* vol. 39, pp. 729-734, Apr 1 1998.

[108] A. S. Yu, *et al.*, "Quantification of Cerebral Glucose Metabolic Rate in Mice Using 18F-FDG and Small-Animal PET," *J Nucl Med,* vol. 50, pp. 966-973, Jun 1 2009.

[109] A. A. Lammertsma and S. P. Hume, "Simplified Reference Tissue Model for PET Receptor Studies," *Neuroimage,* vol. 4, pp. 153-158, 1996.

[110] R. Minamimoto, *et al.*, "FDG-PET of patients with suspected renal failure: standardized uptake values in normal tissues," *Ann Nucl Med,* vol. 21, pp. 217-222, Jun 2007.

[111] E. Laffon, *et al.*, "The effect of renal failure on 18F-FDG uptake: a theoretic assessment," *J Nucl Med Technol,* vol. 36, pp. 200-202, Dec 2008.

[112] M. Allen-Auerbach and W. A. Weber, "Measuring response with FDG-PET: methodological aspects," *Oncologist,* vol. 14, pp. 369-377, Apr 2009.

[113] S. C. Huang, *et al.*, "A Public Domain Dynamic Mouse FDG MicroPET Image Data Set for Evaluation and Validation of Input Function Derivation Methods," presented at the Nuclear Science Symposium Conference Record, IEEE, San Diego, 2006.

[114] M. R. Benz, *et al.*, "Treatment Monitoring by 18F-FDG PET/CT in Patients with Sarcomas: Interobserver Variability of Quantitative Parameters in Treatment-Induced Changes in Histopathologically Responding and Nonresponding Tumors," *J Nucl Med,* pp. 1038-1046, Jun 13 2008.

[115] A. Dirisamer, *et al.*, "Dual-time-point FDG-PET/CT for the detection of hepatic metastases," *Mol Imaging Biol,* vol. 10, pp. 335-340, Nov-Dec 2008.

[116] D. A. Mankoff, *et al.*, "Quantitative Analysis in Nuclear Oncologic Imaging," in *Quantitative Analysis in Nuclear Medicine Imaging*, H. Zaidi, Ed., ed New York: Springer Science+Business Media, Inc., 2006, pp. 494-536.

[117] R. Irwin, *et al.*, "Normal Bone Density Obtained in the Absence of Insulin Receptor Expression in Bone," *Endocrinology,* vol. 147, pp. 5760-5767, Dec 1 2006.

[118] C. B. Saw, *et al.*, "Determination of CT-to-density conversion relationship for image-based treatment planning systems," *Medical Dosimetry,* vol. 30, pp. 145-148, 2005.

[119] C. Suckow, *et al.*, "Multimodality rodent imaging chambers for use under barrier conditions with gas anesthesia," *Mol Imaging Biol,* vol. 11, pp. 100-106, Mar-Apr 2009.

[120] D. B. Stout, *et al.*, "Small animal imaging center design: the facility at the UCLA Crump Institute for Molecular Imaging," *Mol Imaging Biol,* vol. 7, pp. 393-402, Nov-Dec 2005.

[121] A.-X. Chatziioannou, *et al.*, "Method and apparatus for animal positioning in imaging systems," 2006.

[122] P. L. Chow, *et al.*, "A method of image registration for small animal, multi-modality imaging," *Phys Med Biol,* vol. 51, pp. 379-390, Jan 21 2006.

[123] P. L. Chow, *et al.*, "Attenuation correction for small animal PET tomographs," *Phys Med Biol,* vol. 50, pp. 1837-1850, Apr 21 2005.

[124] A. M. Loening and S. S. Gambhir, "AMIDE: a free software tool for multimodality medical image analysis," *Mol Imaging,* vol. 2, pp. 131-137, Jul 2003.

[125] T. J. Spinks, *et al.*, "The effect of activity outside the direct field of view in a 3D-only whole-body positron tomograph," *Phys Med Biol,* vol. 43, pp. 895-904, Apr 1998.

[126] E. L. William and E. C. Harvey, "Marching cubes: A high resolution 3D surface construction algorithm," *Comput Graph,* vol. 21, pp. 163-169, 1987.

[127] Y. Hashimoto, *et al.*, "Accuracy of PET for Diagnosis of Solid Pulmonary Lesions with 18F-FDG Uptake Below the Standardized Uptake Value of 2.5," *J Nucl Med,* vol. 47, pp. 426-431, Mar 1 2006.

[128] C. S. Smith, *et al.*, "False-Positive Findings on 18F-FDG PET/CT: Differentiation of Hibernoma and Malignant Fatty Tumor on the Basis of Fluctuating Standardized Uptake Values," *Am. J. Roentgenol.,* vol. 190, pp. 1091-1096, Apr 1 2008.

[129] C.-J. Chen, *et al.*, "Dual-Phase 18F-FDG PET in the Diagnosis of Pulmonary Nodules with an Initial Standard Uptake Value Less Than 2.5," *Am J Roentgenol,* vol. 191, pp. 475-479, Aug 1 2008.

[130] D. Feng, *et al.*, "Models for computer simulation studies of input functions for tracer kinetic modeling with positron emission tomography," *Int J Biomed Comput,* vol. 32, pp. 95-110, Mar 1993.

[131] J. Logan, *et al.*, "A strategy for removing the bias in the graphical analysis method," *J Cereb Blood Flow Metab,* vol. 21, pp. 307-20, Mar 2001.

[132] Y.-G. Wu, "Noninvasive quantification of local cerebral metabolic rate of glucose for clinical application using positron emission tomography and F-fluoro-2-deoxy-D-glucose," *J Cereb Blood Flow Metab,* vol. 28, pp. 242-250, 2007.

[133] G. Z. Ferl, *et al.*, "Estimation of the 18F-FDG Input Function in Mice by Use of Dynamic Small-Animal PET and Minimal Blood Sample Data," *J Nucl Med,* vol. 48, pp. 2037-2045, Dec 1 2007.

[134] O. L. Munk, *et al.*, "Liver Kinetics of Glucose Analogs Measured in Pigs by PET: Importance of Dual-Input Blood Sampling," *J Nucl Med,* vol. 42, pp. 795-801, May 1 2001.

[135] A. Bertoldo, *et al.*, "Kinetic modeling of [18F]FDG in skeletal muscle by PET: a four-compartment five-rate-constant model," *Am J Physiol Endocrinol Metab,* vol. 281, pp. E524-536, Sep 1 2001.

[136] D. L. Chen, *et al.*, "Comparison of Methods to Quantitate 18F-FDG Uptake with PET During Experimental Acute Lung Injury," *J Nucl Med,* vol. 45, pp. 1583-1590, Sep 1 2004.

[137] Y.-H. D. Fang and R. F. Muzic, Jr., "Spillover and Partial-Volume Correction for Image-Derived Input Functions for Small-Animal 18F-FDG PET Studies," *J Nucl Med,* vol. 49, pp. 606-614, Apr 1 2008.

[138] H. Wu, *et al.*, "Quantitative evaluation of skeletal tumours with dynamic FDG PET: SUV in comparison to Patlak analysis," *Eur J Nucl Med,* vol. 28, pp. 704-10, Jun 2001.

[139] N. M. Freedman, *et al.*, "Comparison of SUV and Patlak slope for monitoring of cancer therapy using serial PET scans," *Eur J Nucl Med,* vol. 30, pp. 46-53, Jun 2003.

[140] H. Iida, *et al.*, "Use of the Left Ventricular Time-Activity Curve as a Noninvasive Input Function in Dynamic Oxygen-15-Water Positron Emission Tomography," *J Nucl Med,* vol. 33, pp. 1669-1677, Sep 1 1992.

[141] S. J. Gaffney, "Probabilistic curve-aligned clustering and prediction with regression mixture models," Doctor of Philosophy Doctor of Philosophy, Information and Computer Science, University of California, Irvine, Irvine, 2004.

[142] J. van den Hoff, *et al.*, "Accurate Local Blood Flow Measurements with Dynamic PET: Fast Determination of Input Function Delay and Dispersion by Multilinear Minimization," *J Nucl Med,* vol. 34, pp. 1770-1777, Oct 1 1993.

[143] B. Dogdas, *et al.*, "Digimouse: a 3D whole body mouse atlas from CT and cryosection data," *Phys Med Biol,* vol. 52, pp. 577-587, Feb 7 2007.

[144] D. W. Shattuck, *et al.*, "Online resource for validation of brain segmentation methods," *Neuroimage,* vol. 45, pp. 431-439, Apr 1 2009.

[145] S. Takikawa, *et al.*, "Noninvasive quantitative fluorodeoxyglucose PET studies with an estimated input function derived from a population-based arterial blood curve," *Radiology,* vol. 188, pp. 131-136, Jul 1993.

[146] D. Vriens, *et al.*, "A Curve-Fitting Approach to Estimate the Arterial Plasma Input Function for the Assessment of Glucose Metabolic Rate and Response to Treatment," *J Nucl Med*, pp. 1933-1939, Nov 12 2009.

[147] T. Ohtake, *et al.*, "Noninvasive Method To Obtain Input Function for Measuring Tissue Glucose Utilization of Thoracic and Abdominal Organs," *J Nucl Med*, vol. 32, pp. 1433-1438, Jul 1 1991.

[148] W. Watabe, *et al.*, "Noninvasive estimation of the aorta input function for measurement of tumor blood flow with [/sup 15/O] water," *IEEE Trans Med Imaging*, vol. 20, pp. 164-174, 2001.

[149] X. Li, *et al.*, "Estimation of myocardial glucose utilisation with PET using the left ventricular time-activity curve as a non-invasive input function," *Med Biol Eng Comput*, vol. 36, pp. 112-117, Jan 1998.

[150] I. Buvat and I. Castiglioni, "Monte Carlo simulations in SPET and PET," *Q J Nucl Med*, vol. 46, pp. 48-61, Mar 2002.

[151] A. Reilhac, *et al.*, "PET-SORTEO: a Monte Carlo-based Simulator with high count rate capabilities," *IEEE Trans Nucl Sci*, vol. 51, pp. 46-52, 2004.

[152] S. Jan, *et al.*, "GATE: a simulation toolkit for PET and SPECT," *Phys Med Biol*, vol. 49, pp. 4543-61, Oct 7 2004.

[153] Z. Li, *et al.*, "Lesion Detection in Dynamic FDG-PET Using Matched Subspace Detection," *IEEE Trans Med Imaging*, vol. 28, pp. 230-240, 2009.

[154] G. Tian, *et al.*, "Automated tumor detection and treatment response assessment with FDG-PET dynamic studies," *J Nucl Med*, vol. 51, p. 25, May 1 2010.

[155] N. Atuegwu, C. , *et al.*, "The integration of quantitative multi-modality imaging data into mathematical models of tumors," *Phys Med Biol*, vol. 55, pp. 2429-2449, 2010.

[156] S. Pierre, *Morphological Image Analysis: Principles and Applications*: Springer-Verlag New York, Inc., 2003.